

University of St Andrews



Full metadata for this thesis is available in
St Andrews Research Repository
at:

<http://research-repository.st-andrews.ac.uk/>

This thesis is protected by original copyright

The Measurement and Interpretation of Stellar Magnetic Fields

by

N.B.P. Phillips

A thesis submitted to the University of St. Andrews in application
for the degree of Master of Science.

St. Andrews

November 1987

i



Tu A794

DECLARATION

Except where reference is made to others, the research described in this thesis and the composition of the thesis are my own work. No part of this work has been submitted for another degree at this or any other University. I was admitted to the Faculty of Science of the University of St. Andrews as a full-time research student under General Ordinance Nō. 12 on 1st October 1986. The higher study of which this is a record was carried out in the University of St. Andrews between the aforementioned date and November 1987.

February 1988

N.B.P. Phillips

CERTIFICATE

I certify that Mr. N.B.P. Phillips has fulfilled the conditions of the Resolutions and Regulations appropriate to the Degree of M.Sc. of the University of St. Andrews and that he is qualified to submit this thesis in application for that degree.

March 1988

D.W.N. Stibbs

In submitting this thesis to the University of St. Andrews, I understand that I am giving permission for it to be made available for use in accordance with the Regulations of the University Library for the time being in force, subject to any copyright vested in the work not being affected thereby. I also understand that the title and abstract will be published, and that a copy of the work may be made and supplied to any *bonafide* library or research worker.

ACKNOWLEDGEMENTS

I am indebted to my supervisors, Professor D.W.N. Stibbs and Dr. A.J. Adamson, for their invaluable help, encouragement, lively discussions, and general support throughout the term of this research.

I would also like to thank the staff and research students of the University of St. Andrews Observatory for their friendly advice and comments. I am especially grateful to Dr. T.R. Carson, Dr. G.W. Hill, Dr W.K. Bonsack, Mr. C.A. Pollard, Mr. G. Willingdale, Mr. D. Pollaco, and Mr. P.R. Rainger.

I would also like to acknowledge my great thanks to my parents for financial support throughout this research, and without whom this work would not have been possible. Lastly, but by no means least I would like to thank my friends in St. Andrews for their support, and my fiance, Paula, for the unimaginable amount of tolerance, support and understanding throughout my time in St. Andrews.

"I CAN SEE THE WORLD
IN A DIFFERENT LIGHT"

-Limelight - Alan Parsons Project

A statistical evaluation of the orientation of the magnetic axis inclination in known magnetic stars is conducted, finding no evidence for the time-dependent obliquity-angle variation proposed by Mestel (1981).

INDEX

	Introduction	1
	Chapter I	
I.0	The zeeman effect	
.1	The classical approach	4
.2	The quantum zeeman effect	
.2.1	The quantum atom	7
.2.2	LS coupling	8
.2.3	The effects of an external magnetic field	10
.2.4	Strong field	13
.2.5	Polarization & Intensities of zeeman components	14
.3	Absorption line formation	18
.4	Observational method	23
.5	Z-Values	26
.6	Disadvantages of the technique	28
.7.1	Methods of analysis	29
.7.2	Some basic fourier theorems	32
.8.1	ZCROSS: The cross-correlation program	33
.8.2	Cross-Correlation	36
.8.3	The noise-generation algorithm	42
.9.1	Methods of measurement	44
.9.2	Individual line determinations	
.9.2.1	The classical measurement system	45
.9.2.2	Template measurements	49
.9.3	Comparison of individual line methods	52
.9.4	Simultaneous line-measurement methods	
.9.4.1	Linearization by $-\frac{1}{\lambda}$	52

.9.4.2	Line grouping by $Z\lambda^2$	53
.9.4.3	Weiss et al. determination method	54
.10.1	Smoothing	56
.10.2	Results of smoothing	59
.11.1	Conclusions	62

Chapter II

II.1.0	Analysis applied to HD49976	
.1.1	The A0p star HD49976	63
.2.1	Reduction	65
.3.1	Measurement strategy	67
.3.2	Weiss sectional cross-correlation	67
.3.3	Measurement and calibration	68
.4.0	Individual line analysis	
.4.1	Definition of the noise level	72
.4.2	Window definition	73
.4.3	Additional template considerations	74
.4.4	Measurement of magnetic field and radial velocities	76
.5.1	Data analysis	77
.5.1.1	Line blending errors	77
.5.1.2	Cross-correlation errors	80
.5.2	Magnetic field determinations	80
.5.3	Radial velocity variations	83
.6.1	Additional data: Equivalent width measurements	85
.6.2	Calcium 3933A ⁰ : The \mathcal{K} -line behaviour	87
.7.1	Conclusions	91

Chapter III

III	Modelling and theories of magnetic variation	
-----	--	--

.1.0	The oblique rotator	92
.1.1	The decentred dipole	97
.1.2	The oblique rotator: quadrupole symmetry	99
.1.3	The symmetric rotator	101
.2	Harmonic analysis	
.2.1	Deutsch's harmonic analysis	102
.2.2	Mihalas' analysis	110
.2.3	Application of Mihalas' harmonic analysis	114
.2.3.1	A model atmosphere	114
.2.3.2	Calculation of the co-efficients	117
.2.3.3	Restriction of Mihalas' analysis	121
.3	Statistical evaluation of magnetic axis inclination	
.3.1	Theoretical considerations	122
.3.2	Statistical tests	125
.3.2.1	The Kolmogorov-Smirnov test	125
.3.2.2	The von Mises ω^2 test	126
.3.3.1	Hypothesis testing	128
.3.3.2	Observations on young stars	131
.3.3.3	Discussion	132
	APPENDIX-A: Absorption line list	133
	References:	138

INTRODUCTION

With the discovery in 1913 by George Hale that the Sun possessed a general magnetic field, it was proposed that a magnetic field may be an intrinsic property of all stars. However, it was not until 1958 and Babcock's Catalog of Magnetic Stars that magnetic fields were observed in stars other than the Sun. Babcock's catalog identified one particular class of stars as showing particularly strong magnetic fields, namely the Ap stars. These initial findings revealed many properties such as magnetic intensification of spectral lines, the cross-over effect, abundance anomalies and, most importantly, the variability of the magnetic field strength in many magnetic stars.

Stibbs (1950) considered these peculiarities to be caused by the non-coincidence of magnetic and rotational axes, the so-called oblique rotator. As the star rotates, it is thus possible for first one pole of a dipole like field followed by the other to be aspected, causing a variation in the measured effective magnetic field, H_z . This simple explanation, in contrast to the complex theories of fast oscillations in magnetic field strength within the stellar atmosphere, has since become the accepted basis of the field oscillations, though many modifications have been proposed (see Section III.1)

Further consideration of the geometry of the oblique rotator by Deutsch (1970), resulted in the production of low-resolution maps of the stellar surface, revealing that the observed abundance-anomalies could be explained within the framework of an enhanced-abundance spotted surface. According to Michaud (1970), a sufficiently strong magnetic field may stabilize the stellar atmosphere, allowing diffusion to predominate over turbulent forces. Thus it is possible that instead of a homogeneous mixture of elements within the atmosphere, stratification of elements and channelling of ionized elements along lines of magnetic force will result in a spotted surface.

Havnes & Conti (1971) proposed that the abundance enhancements to be the result of preferential magnetic accretion of interstellar material in the absence of a stellar wind, biased towards the heavier elements. The captured heavy elements are then channelled towards the magnetic poles, where, in analogy with the Van Allen radiation belts, a proportion are not reflected by magnetic mirroring and reach the surface. A composite of Michaud's stability and this accretion could then produce the observed variations.

From these arguments, the presence of a magnetic field is observed to produce appreciable changes in stellar structure. Indeed Shallis & Blackwell (1979) and Hubbard & Dearborn (1982) propose that the magnetic field in Ap stars may be great enough to expand the star by as much as 20% for a $2M_{\odot}$ star, and considerably more for a $3M_{\odot}$ star.

An additional contemporary problem in stellar astronomy is whether the stellar magnetic field is a 'relic' of an older field, perhaps generated by black holes in the early universe (Leahy & Vilenkin (1981)), or continuously generated by dynamo effects within the stars. This argument encompasses not only magnetic stars, but also to the weaker magnetic fields of all stars, and to the very weak fields observed within the planetary solar system.

The magnetic stars, being the most observable large sample of large-scale magnetic effects, are thus crucial to our understanding of the genesis, and various phenomena of magnetic fields.

To date, measurement of stellar magnetic fields have been conducted by methods that may be divided into two categories: Firstly those measuring the magnetic field of individual elements within the stellar atmosphere, an example of which is Pyper's (1969) analysis of $\alpha^2 CVn$. Secondly, measurements of the global magnetic field as conducted by Weiss (1977), or the H_{β} polarimetry of Angel and Landstreet (1970).

Though enabling mapping of the stellar surface and thus attaining more usable information, the first method suffers from the considerable time required for analysis, and its reliance upon human judgement (section I.3).

The research here conducted provides a quick, accurate and dispassionate replacement to this method which, it is felt, will considerably enhance the volume and quality of magnetic field data, upon which discrimination of future and existing theories are made. It is hoped that this will enable answers to be provided to many of the contemporary quandaries such as the difference between A-stars and Ap-stars, the origin of the field, whether time-dependent migration of the magnetic pole inclination occurs (section III.3.2) and many other associated conundrums.

I.0 The Zeeman effect

I.1 The classical approach

A means to observe the magnetic fields of stars was provided by the discovery of Pieter Zeeman in 1896 that spectral lines were split into components under the influence of a magnetic field. With the discovery of the electron a year later, Zeeman and Lorentz proposed that the electron was a direct participant in the emission of spectral lines.

Lorentz considered the electron (charge $-q$, mass m_e) to be bound to a central position by a force $F = -kr$, causing the displacement to vary harmonically with frequency,

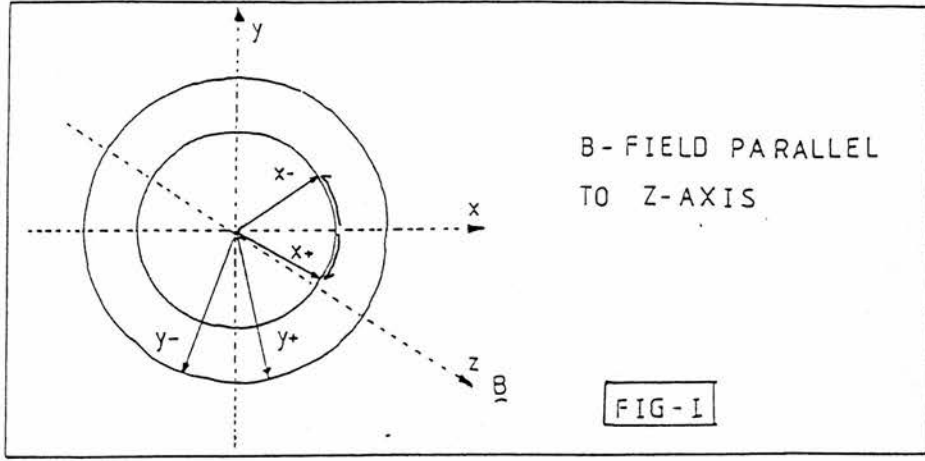
$$\nu_0 = \frac{1}{2\pi} \sqrt{\frac{k}{m}} \quad (1.1)$$

and that this frequency of oscillation was the genesis of the light emitted by the atom. In cartesian co-ordinates each component of r will vary with this frequency, but with different amplitudes and phases.

When the electron is subjected to an external magnetic field, the frequency of the electron will be changed due to the perturbing electromagnetic force, $F = q(v \times B)$ exerted upon the electron.

Consider a magnetic field oriented along the z -axis, as shown in (fig. I). The z -component of motion will be unaffected by the perturbing force, but the components perpendicular to the force will experience an additional force of magnitude qvB .

In general, any simple harmonic vibration can be regarded as the superposition of two circular motions of the same frequency but in contra-rotation. Thus the x and y motions may be broken down into $x \pm$ and $y \pm$. The two senses of rotation will experience a different force corresponding to $\pm qvB$.



Thus we may write the orbital motion as,

$$\frac{mv^2}{r} = kr \pm qvB. \quad (1.2)$$

Substituting in $v = 2\pi r\nu$ and $k = 4\pi^2 m\nu_0^2$ from Eq.(1.1) and solving for ν ,

$$\nu = \pm \frac{qB}{4\pi m} + \sqrt{\nu_0^2 + \left(\frac{qB}{4\pi m}\right)^2} \quad (1.3)$$

In all cases of interest,

$$\nu_0^2 \gg \left(\frac{qB}{4\pi m}\right)^2$$

resulting in,

$$\nu = \nu_0 + \frac{qB}{4\pi m}. \quad (1.4)$$

It can also be noted by consideration of the orientation that the ν_+ vibrations correspond to the two + (clockwise) rotations and the ν_- by the two - (anti-clockwise) rotations. Thus, light emitted due to this rotation will be circularly polarized when observed parallel to the field, and plane polarized when perpendicular to the field. Likewise, the z-component ν_0 will be linearly polarized when viewed perpendicular to the field, and will vanish when viewed parallel to the field.

I.2 The quantum zeeman effect

I.2.1 The quantum atom

In consideration of the quantum zeeman effect, and the effects of a large magnetic field, it is useful to review a small part of the quantum mechanical description of the atom; specifically, the concept of electron spin, and the resultant effect of LS or Russell-Saunders coupling.

From Schrodinger's solution of the one-electron atom, there arises the necessity of describing the energy levels of the electron in terms of 3 quantum numbers: n, l, m_l . These refer to the energy, angular momentum, and z-component of the angular momentum of the electron. However, in a full relativistic treatment, conducted by Dirac, the electron was attributed with a spin, $s = \pm \frac{1}{2}$. This created the necessity to introduce a fourth quantum number m_s , the z-component of the spin. The allowed values of these quantum numbers are illustrated in fig (IV).

n	1		2			3								
l	0	0	1			0	1			2				
m_l	0	0	+1	0	-1	0	+1	0	-1	+2	+1	0	-1	-2
m_s	↑↓	↑↓	↑↓	↑↓	↑↓	↑↓	↑↓	↑↓	↑↓	↑↓	↑↓	↑↓	↑↓	↑↓
Nomenclature	1s	2s	2p			3s	3p			3d				

These four quantum numbers determine the exact energy of any energy level in the one-electron atom, and transitions are governed by the selection rule $\Delta l = 0, \pm 1$.

In the case of more than one electron in the outer shell of an atom, the individual electron angular momenta and spin are summed to produce alternative quantum numbers L and S , where $L = l_1 + l_2 + \dots$ and $S = s_1 + s_2 + \dots$

I.2.2 LS Coupling

The fact that the electron has a spin results in a spin angular momentum,

$$\sigma = \sqrt{s(s+1)}\hbar \quad (1.5)$$

By virtue of its spin, the electron has a magnetic moment of magnitude,

$$\mu_s = -2 \left(\frac{e}{2m} \right) \sigma_s = -\frac{e}{m} \sqrt{s(s+1)}\hbar \quad (1.6)$$

If the electron has any orbital angular momentum ($l \neq 0$), then in the electron's rest frame, the nucleus has a non-zero velocity and will produce a magnetic field at the location of the electron equal to,

$$B = \frac{1}{c^2} v \times E = \frac{l}{mec^2 r} \frac{dV}{dr} \quad \text{where} \quad V = -\frac{Ze^2}{4\pi\epsilon_0 r} \quad (1.7)$$

The energy of the orientation of the electron's magnetic moment μ_e in such a field is,

$$W = -\mu \cdot B = \frac{1}{2} \cdot \frac{\sigma \cdot l}{m^2 c^2 r} \cdot \frac{dV}{dr} \quad (1.8)$$

However, when Thomas' precession is taken into account, the actual energy becomes half this amount. Evaluating $\frac{dV}{dr}$ and including the $\frac{1}{2}$ factor, we arrive at,

$$W = \frac{1}{2} \cdot \frac{Z^4 e^2 (\sigma \cdot l)}{4\pi\epsilon_0 m^2 c^2 a_0^3 n^3 l(l + \frac{1}{2})(l + 1)} \quad (1.9)$$

Not only are the energy levels of the electron changed due to this interaction energy, but, more importantly, the torque $\mu \times B$ changes the direction of l and

s. This can be seen from Eq (I.9) by the scalar product of $(\sigma.l)$. Now l and s are no longer independent and only the sum $j = l + s$ remains constant. Graphically, the vector j remains constant, while l and s precess around their sum. To evaluate the scalar product, we make use of the fact that $j = l + s$ as below.

$$\begin{aligned}
 j &= (l + s) \\
 j.j &= l.l + 2s.l + s.s \\
 s.l &= \frac{1}{2}(j.j - l.l - s.s) \\
 \sigma.l &= \frac{1}{2}(j.j - l.l - \sigma.\sigma)
 \end{aligned}
 \tag{1.10}$$

It is now no longer possible to describe the energy levels by the quantum numbers n, l, m_l, m_s , as l is no longer a good quantum number. As such, an alternative set are chosen comprising of n, l, j, m_j , where m_j is the z component of j and takes values between $+j$ and $-j$ inclusive. The corresponding selection rules for these quantum numbers now becomes $\Delta J = 0, \pm 1$ within the existing rule $\Delta m_j = 0, \pm 1$.

I.2.3 The effects of an external magnetic field

We may express the net magnetic moment as the sum of the orbital magnetic moment and the spin magnetic moments of the individual electrons.

$$\begin{aligned}
 \mu &= - \sum_{i=1}^n \left[\frac{1}{2} \left(\frac{e}{m} \right) l_i + \left(\frac{e}{m} \right) \sigma_i \right] \\
 \mu &= - \frac{1}{2} \left(\frac{e}{m} \right) \sum_i l_i - \left(\frac{e}{m} \right) \sum_i \sigma_i \\
 \mu &= - \frac{1}{2} \left(\frac{e}{m} \right) (L + 2S) \\
 \mu &= - \frac{1}{2} \left(\frac{e}{m} \right) (J + S)
 \end{aligned} \tag{1.11}$$

As can be seen from eq. (1.11), μ is not necessarily parallel to J , and in the absence of any external magnetic field, L , S and μ will precess around J .

On application of an external magnetic field, J will no longer remain constant, but will precess around the field by virtue of the magnetic moment μ . This precession is much slower than that of the L , S around J in the case of a weak field, enabling the time-average component of μ along the field to be approximately equal to its component along J , multiplied by the component of J along the field.

Then,

$$\begin{aligned}
 W &= \frac{1}{2} \left(\frac{e}{m} \right) \frac{[(J + S) \cdot J](J \cdot B)}{|J|^2} \\
 &= \frac{1}{2} \left(\frac{eB}{m} \right) \frac{(|J|^2 + J \cdot S)}{|J|^2} J_z
 \end{aligned} \tag{1.12}$$

Where $J \cdot S$ may be evaluated similar to eq. (1.10),

$$J \cdot S = \frac{1}{2} (|J|^2 + |S|^2 - |L|^2)$$

resulting in,

$$\begin{aligned}
 W &= \frac{1}{2} \left(\frac{eB}{m} \right) \left\{ \frac{J(J+1) + \frac{1}{2}[J(J+1) + S(S+1) - L(L+1)]}{2J(J+1)} \right\} m_j \hbar \\
 &= \frac{1}{2} \left(\frac{e\hbar B}{m} \right) \left\{ 1 + \frac{J(J+1) + S(S+1) - L(L+1)}{2J(J+1)} \right\} m_j \\
 W &= \frac{1}{2} \left(\frac{e\hbar B}{m} \right) g m_j
 \end{aligned} \tag{1.13}$$

where g_j is equal to,

$$g_j = 1 + \frac{J(J+1) + S(S+1) - L(L+1)}{2J(J+1)} \tag{1.14}$$

In the presence of an external magnetic field, an energy level is split into $2J+1$ levels corresponding to the values of m_j . It is this Landé g-factor that results in the appearance of 'normal' or 'anomalous' zeeman patterns, and not, as one might presume, due to the $2J+1$ levels.

To clarify this, consider two energy levels, E_1 and E_2 , and their respective splitting energy,

$$\Delta E_1 = \frac{1}{2} \left(\frac{e\hbar B}{m} \right) g_1 M_{j_1} \quad \Delta E_2 = \frac{1}{2} \left(\frac{e\hbar B}{m} \right) g_2 M_{j_2} \tag{1.15}$$

The shift in frequency of emitted radiation in a transition 1 to 2 is given by,

$$\begin{aligned}
 \Delta\omega_{12} &= \frac{\Delta E_1 - \Delta E_2}{\hbar} \\
 &= \frac{1}{2} \left(\frac{e\hbar B}{m} \right) (g_1 M_{j_1} - g_2 M_{j_2})
 \end{aligned} \tag{1.16}$$

Thus, if $g_1 = g_2$,

$$\Delta\omega_{12} = \frac{1}{2} \left(\frac{e\hbar B}{m} \right) (M_{j_1} - M_{j_2})$$

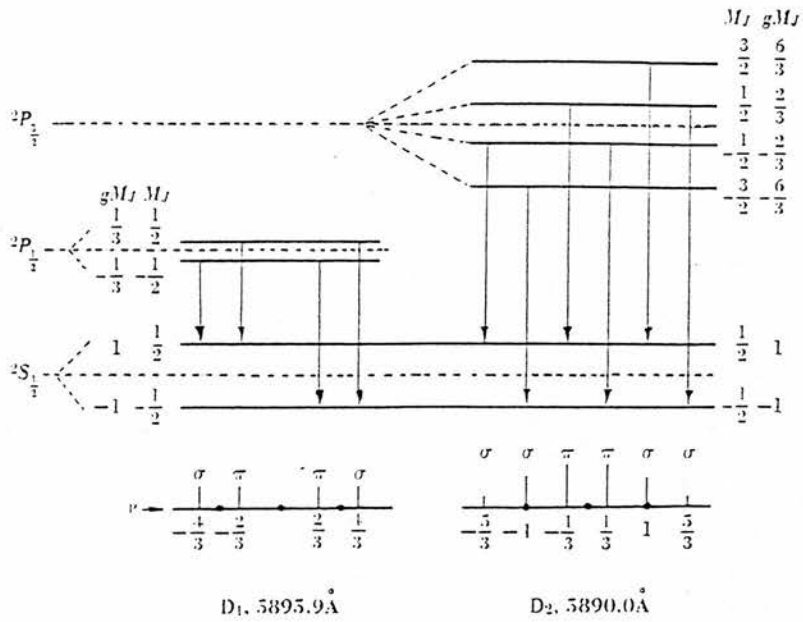


Fig. V Weak-field Zeeman splitting for the sodium *D* lines. The position of the normal triplet is shown by three dots. The same scale is used for all Zeeman separations. The relative heights of the lower lines suggest the theoretical relative intensities.

resulting in the three values that m_j may assume from the selection rules, whereas if $g_1 \neq g_2$ then the level splitting will be different in 1 and 2, and multiple components will be visible as in fig (V).

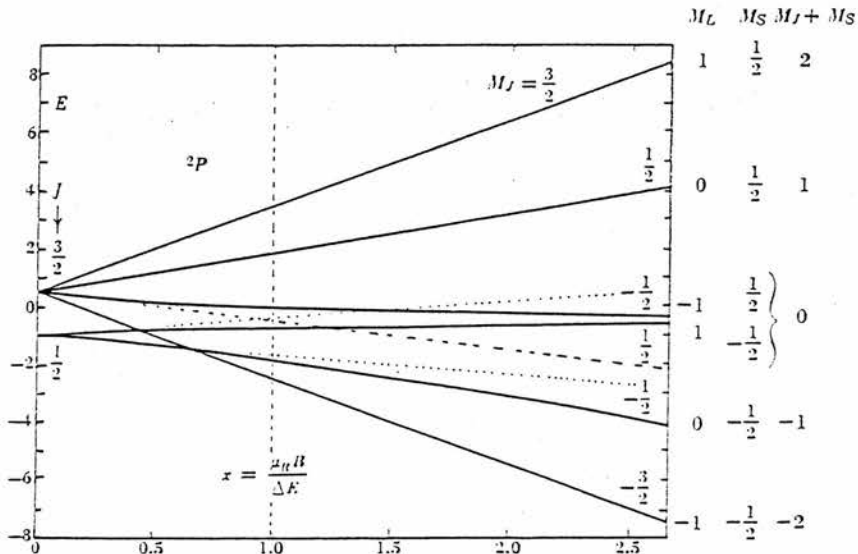


Fig. VI

I.2.4 Strong field

In the presence of an external field causing the zeeman splitting energy to be comparable to the LS fine structure, the approximations above are no longer valid. At this point, the precession of J around the magnetic field and LS around J become comparable, and J ceases to be constant over a revolution. The B-field has no tendency to destroy the coupling of l into L and s into S , but does destroy the coupling of L and S into J . This is known as the Paschen-Back effect.

The B-field required for the appearance of the Paschen-Back effect is dependent upon the ΔE_{ls} of the level concerned and the ΔE_z , zeeman splitting, and can be roughly evaluated by equating these two terms. From I.12 and I.14,

$$3.62 \times 10^{-4} \frac{Z^4 [J(J+1) - L(L+1) - S(S+1)]}{n^3 L(L + \frac{1}{2})(L+1)} = \frac{1}{2} \left(\frac{e\hbar B}{m} \right) g m_j \quad (1.17)$$
$$B = 6248 \frac{Z^4 [J(J+1) - L(L+1) - S(S+1)]}{n^3 L(L + \frac{1}{2})(L+1) g J} eV$$

Both the validity of this equality, and the resultant complication of the zeeman components, are illustrated in fig (VI).

I.2.5 Polarization & intensities of the zeeman components.

Quantum mechanics and time-dependent perturbation theory require that for the emission of radiation the matrix element,

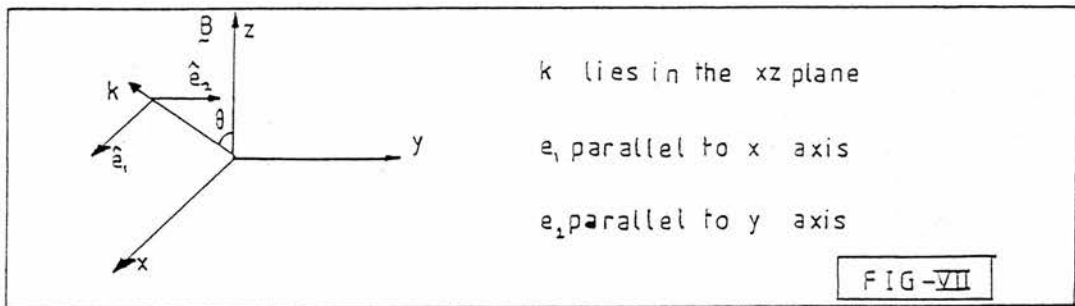
$$| \langle .u_2^* | er | u_1 \rangle | \neq 0$$

and the matrix element squared is proportional to the transition probability. To investigate the zeeman component intensities and polarizations we will be concerned with the transitions from an initial state $|J, m_j \rangle$ to a final state, $\langle J', m'_j |$, and the evaluation of the matrix elements,

$$R_{ij} = | \langle J', m'_j | \hat{e} \cdot r | J, m_j \rangle |^2$$

where \hat{e} is the unit vector perpendicular to k , the direction of propagation of the light.

To evaluate these matrices, consider the following geometrical features,



As there is spherical symmetry around the z -axis, let k lie in the xz plane, and decompose \hat{e} into,

$$\hat{e} = a_1 \hat{e}_1 + a_2 \hat{e}_2 \quad (1.18)$$

The components of \hat{e} can be written in cartesian co-ordinates as,

$$\hat{e} = a_1 \cos \theta \hat{x} + a_2 \hat{y} + a_1 \sin \theta \hat{z} \quad \text{where } r = x\hat{x} + y\hat{y} + z\hat{z} \quad (1.19)$$

Finally, r can be written in spherical tensor co-ordinates as,

$$\begin{aligned} r_0 &= z \\ r_{-1} &= \frac{1}{\sqrt{2}}(x - iy) \\ r_{+1} &= \frac{1}{\sqrt{2}}(x + iy) \end{aligned} \quad (1.20)$$

In spherical tensor notation, the unit vectors of \hat{e} become,

$$\hat{e}_0 = \hat{z} \quad \hat{e}_{-1} = \frac{1}{\sqrt{2}}(\hat{x} - i\hat{y}) \quad \hat{e}_{+1} = \frac{1}{\sqrt{2}}(\hat{x} + i\hat{y}) \quad (1.21)$$

and so,

$$r = r_0 \hat{z} + r_{-1} \frac{1}{\sqrt{2}}(\hat{x} - i\hat{y}) - r_{+1} \frac{1}{\sqrt{2}}(\hat{x} + i\hat{y}) \quad (1.22)$$

The matrix elements may be evaluated, and the non-vanishing components are shown below.

For $J' = J$:

$$\begin{aligned} |\langle \gamma' J M_j | z | \gamma J M_j \rangle|^2 &= M_j^2 A \\ |\langle \gamma' J M_j + 1 | r_{+1} | \gamma J M_j \rangle|^2 &= \frac{1}{2}(J - M_j)(J + M_j + 1)A \\ |\langle \gamma' J M_j - 1 | r_{-1} | \gamma J M_j \rangle|^2 &= \frac{1}{2}(J + M_j)(J - M_j + 1)A \\ \sum_{M_j} |\langle \gamma' J M_j | r | \gamma J M_j \rangle|^2 &= J(J + 1)A \end{aligned}$$

For $J' = J + 1$:

$$\begin{aligned} |\langle \gamma' J + 1 M_j | z | \gamma J M_j \rangle|^2 &= \{(J + 1)^2 - M_j^2\}B \\ |\langle \gamma' J + 1 M_j + 1 | r_{+1} | \gamma J M_j \rangle|^2 &= \frac{1}{2}(J + M_j + 1)(J + M_j + 2)B \\ |\langle \gamma' J + 1 M_j - 1 | r_{-1} | \gamma J M_j \rangle|^2 &= \frac{1}{2}(J - M_j + 1)(J - M_j + 2)B \\ \sum_{M_j} |\langle \gamma' J + 1 M_j | r | \gamma J M_j \rangle|^2 &= 2(J + 1)^2 B \end{aligned}$$

For $J' = J - 1$:

$$\begin{aligned} |\langle \gamma' J - 1 M_j | z | \gamma J M_j \rangle|^2 &= \{J^2 - M_j^2\}C \\ |\langle \gamma' J - 1 M_j + 1 | r_{+1} | \gamma J M_j \rangle|^2 &= \frac{1}{2}(J - M_j)(J - M_j - 1)C \\ |\langle \gamma' J - 1 M_j - 1 | r_{-1} | \gamma J M_j \rangle|^2 &= \frac{1}{2}(J + M_j)(J + M_j - 1)C \\ \sum_{M_j} |\langle \gamma' J - 1 M_j | r | \gamma J M_j \rangle|^2 &= J(2J - 1)C \end{aligned}$$

It is immediately obvious from where the selection rules are evaluated. In table (I) there are only 3 possible non-vanishing values of J' and $m - j'$ resulting in the selection rules,

$$\Delta J = 0, \pm 1 \quad \Delta m_j = 0, \pm 1$$

Additionally, the selection rule $\Delta m_j = 0, \pm 1$ is seen to correspond to the components $r_0, r_{\pm 1}$.

To evaluate $\langle J' m'_j | \hat{e} r | J m_j \rangle$ we now combine eq (1.19), the geometrical part, with the matrix elements to attain,

$$\begin{aligned}
 | \langle J', m'_j | \hat{e} r | J, m_j \rangle |^2 &= |a_1|^2 \sin^2 \theta | \langle J', m_j | z | J, m_j \rangle |^2 \\
 &+ \frac{1}{2} \{ |a_1|^2 \cos^2 \theta + |a_2|^2 - i(a_1 a_2^* - a_1^* a_2) \cos \theta \} | \langle J', (m_j - 1) | r_{-1} | J, m_j \rangle |^2 \\
 &+ \frac{1}{2} \{ |a_1|^2 \cos^2 \theta + |a_2|^2 + i(a_1 a_2^* - a_1^* a_2) \cos \theta \} | \langle J', (m_j + 1) | r_{+1} | J, m_j \rangle |^2
 \end{aligned} \tag{1.24}$$

This formula is the quantum mechanical analogue to the Seares relations (Eq. 1.27). Eq. (1.24) conveys both information on the intensities and polarization states of the zeeman components.

The constants a_1, a_2 define the observed polarization. A state $a_1 = 1, a_2 = 0$ corresponds to the electric vector e , parallel to the z -axis, and observing the longitudinal polarized light from the split components. Likewise $a_1 = 0, a_2 = 1$ corresponds to e perpendicular to the z -axis, transverse light in the xy plane. By writing a_1, a_2 in a column matrix, the similarities to the Jones vectors for describing polarization become apparent.

$$\left. \begin{array}{l} a_2 = 0 \\ a_1 = 1 \end{array} \right\} = \begin{bmatrix} 0 \\ 1 \end{bmatrix} \quad \text{Horizontal P-state}$$

The total intensity of light from a given J, m_j line is thus equal to the result of the Dirac matrix modified by the state of observation polarization. To illustrate this, consider the case of a normal zeeman triplet observed in circularly polarized light:

The appropriate Jones vectors and equivalent values of a_1, a_2 are,

$$\text{R-state} = \frac{1}{\sqrt{2}} \begin{bmatrix} 1 \\ -i \end{bmatrix} \quad \text{L-state} = \frac{1}{\sqrt{2}} \begin{bmatrix} 1 \\ i \end{bmatrix} \tag{1.25}$$

Substituting a_1, a_2 into Eq. (1.20) the Right hand / Left hand states give,

$$\begin{aligned}
 |J', m'_j | \hat{e}_r | J, m_j \rangle|^2 &= \frac{1}{2} \sin^2 \theta | \langle J, m_j | \hat{e}_z | J, m_j \rangle|^2 \\
 &+ \frac{1}{4} (\cos \theta + 1)^2 | \langle J, (m_j - 1) | \hat{e}_{r-1} | J, m_j \rangle|^2 \quad (1.26) \\
 &+ \frac{1}{4} (\cos \theta - 1)^2 | \langle J, (m_j + 1) | \hat{e}_{r+1} | J, m_j \rangle|^2
 \end{aligned}$$

In the case of a normal zeeman triplet, the matrix elements are equivalent, and the relative intensities of the three components are,

$$\begin{aligned}
 I_{r_0} &= \frac{1}{2} \sin^2 \theta \\
 I_{r_{-1}} &= \frac{1}{4} (1 \pm \cos \theta)^2 \\
 I_{r_{+1}} &= \frac{1}{4} (1 \mp \cos \theta)^2
 \end{aligned} \quad (1.27)$$

These relationships were first calculated by Seares (1913) for the displacement of spectral lines noted by Hale (1913) varying with latitude. Seares calculated the components due to linearly and elliptically polarized light incident upon a quarter-wave plate, from a normal zeeman triplet, arriving at the intensities of Eq (1.27) via addition of the respective amplitudes.

With a knowledge of the effects of a magnetic field upon an atom, it solely remains to devise a method for the observation of the components.

I.3 Absorption line formation

The discussion so far of the relative intensities and polarizations evaluated by both the classical and quantum descriptions of the atom has been confined to the simplified case of emission. Since all detection of magnetic fields is performed with measurements upon the stellar absorption line profiles it now remains to consider whether the above effects of a magnetic field may be applied to the case of absorption.

A detailed evaluation of the effects of a magnetic field upon absorption profiles has been conducted by Unno (1956). Since the coefficients of absorption for each zeeman component are functions of the angle between the local vertical and observation angle, and the polarizations are related, if the zeeman components are blended, the radiative transfer cannot be treated by usual polarization optics. Instead, the Stokes parameters (Eq. 1.29), as used by Chandrasekhar (1950) in Rayleigh scattering, must be applied.

$$I = I(I, Q, U, V) \quad (1.28)$$

where,

$$\begin{aligned} I &= I_1 + I_2 & Q &= I_1 - I_2 \\ I_1 &= \zeta_1^2 & I_2 &= \zeta_2^2 \\ U &= 2\zeta_1\zeta_2 \cos(\epsilon_1 - \epsilon_2) & V &= 2\zeta_1\zeta_2 \sin(\epsilon_1 - \epsilon_2) \end{aligned} \quad (1.29)$$

and ζ_1, ζ_2 are the amplitudes, and ϵ_1, ϵ_2 the phase angles of radiation along the co-ordinate axes x, y and the line of sight defined by the z -axis.

By considering the absorption caused by the π component (p-electrons) and the two σ components (l -, r -electrons), Unno formulates the change in intensity in terms of the Stokes parameters and $\kappa_p, \kappa_l, \kappa_r$ the absorption coefficients per unit length to be:

From p-electron absorption of the electric vibration parallel to the field as

$$\begin{aligned}
 \Delta I_1 &= -\kappa_p \Delta z \sin^2 \psi I_1 \\
 \Delta I_2 &= 0 \\
 \Delta U &= -\kappa_p \Delta z \sin^2 \psi U \\
 \Delta V &= -\kappa_p \Delta z \sin^2 \psi V
 \end{aligned}
 \tag{1.30}$$

The r , l electrons absorb elliptically polarized light, resulting in a change in the system due to the l -electron absorption of,

$$\begin{aligned}
 \Delta I_1 &= -\frac{\kappa_l}{4} \Delta z (2I_1 \cos^2 \psi - V \cos \psi) \\
 \Delta I_2 &= -\frac{\kappa_l}{4} \Delta z (2I_2 - V \cos \psi) \\
 \Delta U &= -\frac{\kappa_l}{4} \Delta z U (1 + \cos^2 \psi) \\
 \Delta V &= -\frac{\kappa_l}{4} \Delta z [-2I_1 \cos \psi - 2I_2 \cos \psi + (1 + \cos^2 \psi)V]
 \end{aligned}
 \tag{1.31}$$

and similarly for the r -electron absorption,

$$\begin{aligned}
 \Delta I_1 &= -\frac{\kappa_r}{4} \Delta z [2I_1 \cos^2 \psi + V \cos \psi] \\
 \Delta I_2 &= -\frac{\kappa_r}{4} \Delta z [2I_2 + V \cos \psi] \\
 \Delta U &= -\frac{\kappa_r}{4} \Delta z U (1 + \cos^2 \psi) \\
 \Delta V &= -\frac{\kappa_r}{4} \Delta z [2I_1 \cos \psi + 2I_2 \cos \psi + (1 + \cos^2 \psi)V]
 \end{aligned}
 \tag{1.32}$$

The continuous absorption, where κ_p , κ_l , $\kappa_r = \kappa$ may likewise be written as,

$$\Delta I_1 = -\kappa \Delta z I_1 \quad \Delta I_2 = -\kappa \Delta z I_2 \quad \Delta U = -\kappa \Delta z U \quad \Delta V = -\kappa \Delta z V \tag{1.33}$$

Pure, coherent emission is then considered and found to be,

$$\begin{aligned}
 \Delta I_1 &= \kappa \Delta z \left[1 + \eta_p \sin^2 \psi + \frac{\eta_l + \eta_r}{2} \cos^2 \psi \right] \frac{B}{2} \\
 \Delta I_2 &= \kappa \Delta z \left[1 + \frac{\eta_l + \eta_r}{2} \right] \frac{B}{2} \\
 \Delta U &= 0 \\
 \Delta V &= \kappa \Delta z \left[-\frac{\eta_l + \eta_r}{2} \right] \cos \psi B
 \end{aligned} \tag{1.34}$$

Since U has no interaction with the other parameters in the emission case, Unno then sets U identically equal to zero.

Incorporating both emission and absorption to create the transfer equations, Unno attains, after simplification,

$$\begin{aligned}
 \cos \theta \frac{dI}{d\tau} &= (1 + \eta_I)I + \eta_Q + \eta_V - (1 + \eta_I)B \\
 \cos \theta \frac{dQ}{d\tau} &= \eta_Q I + (1 + \eta_I)Q - \eta_Q B \\
 \cos \theta \frac{dV}{d\tau} &= \eta_V I + (1 + \eta_I)V - \eta_V B
 \end{aligned} \tag{1.35}$$

where,

$$\begin{aligned}
 I &= I_1 + I_2 & Q &= I_1 - I_2 \\
 \eta_I &= \frac{\eta_r}{2} \sin^2 \psi + \frac{\eta_l + \eta_r}{4} (1 + \cos^2 \psi) & \eta_V &= -\frac{\eta_r + \eta_l}{2} \cos \psi \\
 \eta_Q &= \left(\frac{\eta_p}{2} - \frac{\eta_l + \eta_r}{4} \right) \sin^2 \psi & d\tau &= -\kappa \Delta z \sec \theta
 \end{aligned} \tag{1.36}$$

The solution of the transfer equations may be completed by using the familiar black-body approximation for the source function in the continuum,

$$B = B_0(1 + \beta_0 \tau) \tag{1.37}$$

and the intensities are then evaluated as,

$$\begin{aligned}
 I(0, \theta) &= B_0 \left[1 + \beta_0 \cos \theta \left(\frac{1 + \eta_I}{(1 + \eta_I)^2 - \eta_Q^2 - \eta_V^2} \right) \right] \\
 Q(0, \theta) &= -B_0 \beta_0 \cos \theta \left(\frac{\eta_Q}{(1 + \eta_I)^2 - \eta_Q^2 - \eta_V^2} \right) \\
 V(0, \theta) &= -B_0 \beta_0 \cos \theta \left(\frac{\eta_V}{(1 + \eta_I)^2 - \eta_Q^2 - \eta_V^2} \right)
 \end{aligned} \tag{1.38}$$

The continuous background may be evaluated by letting,

$$\eta_p = \eta_l = \eta_r = 0$$

leaving the only non-zero term to be,

$$I(0, \theta) = B_0(1 + \beta_0 \cos \theta)$$

The intensities and polarizations are measured in units of the continuous background which may then be found to be,

$$r_I(\theta) = \frac{I_0(0, \theta) - I(0, \theta)}{I_0(0, \theta)} = \frac{\beta \cos \theta}{1 + \beta_0 \cos \theta} \left[1 - \frac{1 + \eta_I}{(1 + \eta_I)^2 - \eta_Q^2 - \eta_V^2} \right]$$

and likewise,

$$\begin{aligned}
 r_Q(\theta) &= \frac{\beta_0 \cos \theta}{1 + \beta \cos \theta} \left[\frac{\eta_Q}{(1 + \eta_I)^2 - \eta_Q^2 - \eta_V^2} \right] \\
 r_V(\theta) &= \frac{\beta_0 \cos \theta}{1 + \beta_0 \cos \theta} \left[\frac{\eta_V}{(1 + \eta_I)^2 - \eta_Q^2 - \eta_V^2} \right]
 \end{aligned} \tag{1.39}$$

This then defines the total absorption intensities for any angle ψ , and θ . Assuming a doppler contour for each component,

$$\eta_p = \eta(v) \quad \eta_l = \eta(v) - v_H \frac{d\eta}{dv} \quad \eta_r = \eta(v) + v_H \frac{d\eta}{dv}, \tag{1.40}$$

in the case of non-resolution of the components due to a weak field, terms higher than v_H may be neglected.

Substitution into (Eq. 1.36) results in only η_V being non-zero, as,

$$\eta_V = r_H \cos \psi \frac{d\eta}{dv}$$

Observation of the longitudinal zeeman effect is then found to result in intensities given by $r_I \pm r_V$ for the two spectra, giving, from (Eq. 1.39),

$$r_I \pm r_V = \frac{\beta_0 \cos \theta}{1 + \beta_0 \cos \theta} \cdot \frac{\eta(v \pm v_H \cos \psi)}{1 + \eta(v + v_H \cos \psi)} \quad (1.41)$$

In the case when $1 \gg \eta(v + v_H \cos \psi)$, this is then found to correspond to the emission formulae, with the familiar $\cos \psi$ found by Seares.

$$r_I \pm r_V = \frac{\beta_0 \cos \theta}{1 + \beta_0 \cos \theta} \{ \eta(v) \mp \eta(v_H \cos \psi) \}$$

However, when $1 \not\gg \eta(v + v_H \cos \psi)$ the absorption formula is found to differ from that of emission. For the use of the Seares relationships it is thus essential that $1 \geq \eta(v + v_H \cos \psi)$.

Unno also notes that the magnetic intensification, caused by the magnetically broadened profile, is greatest at $\psi = 55^\circ$. Since magnetic-field measurements evaluated are weighted by the equivalent width value (sect. III.2.1), this may be the cause of the anharmonic field variations found within the measurement of individual elemental magnetic fields, and absent in the technique of H_β polarimetry (Sect. I.7.1). Since field measurements attained by H_β polarimetry are not dependent upon the Seares relations, this effect would not be apparent. Anharmonic variations are notably found to be within $\frac{\pi}{2}$ of the magnetic field extrema, consistent with such an hypothesis.

I.4 Observational method

In theory, the determination of a magnetic field from the zeeman components should be a matter of ease. However, the small shift between components of the zeeman pattern is only visible at high fields, due to effects of natural and doppler broadening as well as the spectroscopic dispersion used. The profile seen in unpolarized light is greatly blended, and separation of the components for determination of ΔE_z is impossible.

Zeeman (1913) described a differential analyzer for analysis of magnetic splitting and, from this, Babcock (1946) built a replica of the analyzer for determination of stellar magnetic fields.

The differential analyzer isolates the L-state polarization from the R-state, by interposing a quarter-wave plate in front of a calcite crystal.

The R and L-state light can be thought of as two plane-polarized waves orientated along x , and y , but $\frac{\pi}{4}$ out of phase.

$$\begin{aligned} E_x(z, t) &= x E_0 \cos(kz - \omega t) \\ E_y(z, t) &= y E_0 \cos\left(kz - \omega t - \frac{\pi}{4}\right) = y E_0 \sin(kz - \omega t) \end{aligned} \tag{1.43}$$

The $\frac{\lambda}{4}$ wave plate is produced out of mica, an optically anisotropic crystal, which has two refractive indices dependent upon the relative orientation of the electric vector e , and the optic axis. The mica plate is orientated such that the two refractive indices lie along x , and y producing a differing speed of propagation between the waves E_y, E_x . This results in a difference in the relative optical path given by,

$$\Lambda = d(n_E - n_O) \tag{1.44}$$

The phase difference introduced becomes,

$$\Delta\Phi = \frac{2\pi d}{\lambda_0} (|n_O - n_E|) \tag{1.45}$$

The depth of the mica plate is calculated to give a $\frac{\pi}{2}$ phase shift for a given wavelength, creating two P-state waves at $\pm 45^\circ$, from the circularly polarized light.

As can be seen from Eq (1.45), the exact phase shift is dependent upon the wavelength of incident light. For wavelengths other than λ_0 , the phase shift produced will be,

$$\Delta\Phi = \frac{\pi\lambda_0}{2\lambda} \quad (1.46)$$

This variation may be minimised if λ is restrained to within a few hundred angstroms of λ_0 , as is the case here.

The calcite crystal is also anisotropic, but in this case the optic axis lies at an angle to the incident face. This produces two waves, corresponding to the $P \pm 45^\circ$ -states, mutually displaced.

A high-resolution coude spectrograph is placed behind the differential analyzer, producing two adjacent spectra corresponding to the R and L-state polarized incident light. This arrangement is shown in figure (VIII).

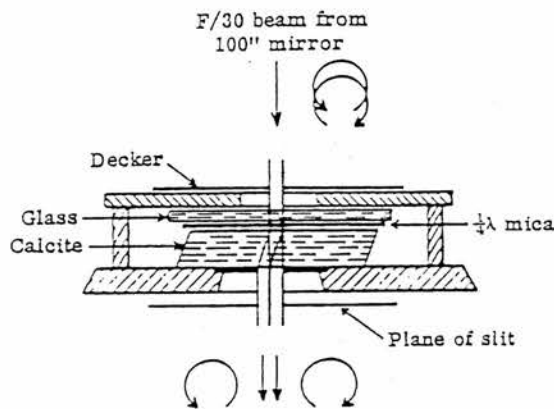


Fig. 4. Differential analyzer for right-hand and left-hand circularly polarized light (Babcock, 1958).

In the creation of the two spectra, it is important to compensate for any unwanted polarization. One such cause is that of polarization by reflection from the coude flats and other grazing incidence apparatus within the telescope. The degree of polarization varies with declination and, unless compensated for,

would reduce the relative zeeman displacements. Babcock (1958) used two crossed $\frac{\pi}{8}$ plates varying in azimuth, but any equivalent, such as a Babinet-Soleil compensator would be appropriate in restoring the original polarization states.

As mentioned earlier, the Babcock analyzer separates the R- and L-state π components enabling the mutual displacements to be measured. As can be seen from Eq. (1.27), the total separation occurs only when the angle between observation and field is zero. At all other angles, the central π component will appear in both spectra, adding to the profile blending. It is still possible to deconvolve the field by consideration of the centre of gravity of the profile.

The displacement of the centre of gravity produced by a field H may be written as,

$$\delta\lambda = \frac{aH(I_V - I_R)}{(I_V + I_M + I_R)} \quad (1.47)$$

where $a = \frac{e\lambda^2}{4\pi mc}$ from Eq.(1.4). Substituting for the relative intensities from Eq. (1.27),

$$I_V = \frac{1}{4}(1 \pm \cos \theta)^2$$

$$I_M = \frac{1}{2} \sin^2 \theta$$

$$I_R = \frac{1}{4}(1 \mp \cos \theta)^2$$

we see that the displacement of the blended lines in the two spectra is

$$\delta\lambda = \pm aH \cos \theta \quad (1.48)$$

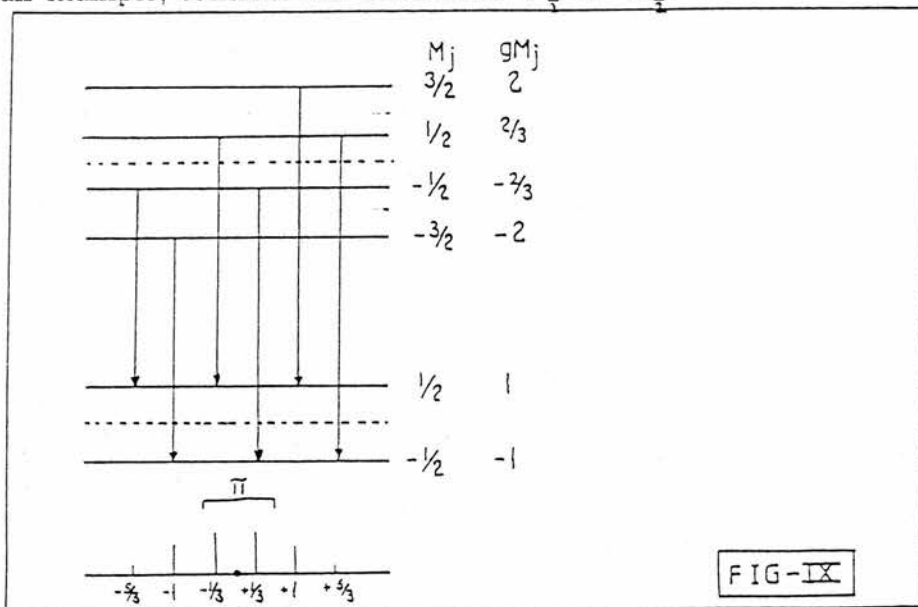
Using $H \cos \theta = H_z$, the total displacement corresponds to twice the splitting caused by a magnetic field H_z , the field component parallel to the line of sight.

I.5 Z-values

In the case where there arise multiple σ, π components, blending of the multiple π components results in an erroneous $\delta\lambda$. This is due to the shifted centre of gravity of the individual σ, π profiles. To overcome this, each line is assigned a Z-value, where Z is defined as a multiplicative factor relating the magnetic field to the mutual $d\lambda$ displacement that would arise from a $g_j = 1$ (see Eq. (1.14)) zeeman triplet.

Z may be evaluated from experimental observation of the longitudinal zeeman effect, or calculated from the intensities and displacements of the σ, π components, as given in section I.2.3 and I.2.5.

As an example, consider the transition ${}^2P_{3/2}$ to ${}^2S_{1/2}$.



From Eq. (1.14) the g values corresponding to the initial and final levels are $g = 2$, and $g = \frac{4}{3}$ respectively. The transition is one of $\Delta J = -1$ and from table (I), the intensities may be evaluated as,

$$m_J \left(\frac{1}{2} \quad \text{to} \quad -\frac{1}{2} \right) = \frac{1}{2} \cdot 2 \cdot 1 = 1$$

$$m_J \left(-\frac{1}{2} \quad \text{to} \quad -\frac{3}{2} \right) = \frac{1}{2} \cdot 3 \cdot 2 = 3$$

The centre of gravity of the σ, π profile is thus,

$$d\lambda = 1.167aH \cos \theta \quad (1.49)$$

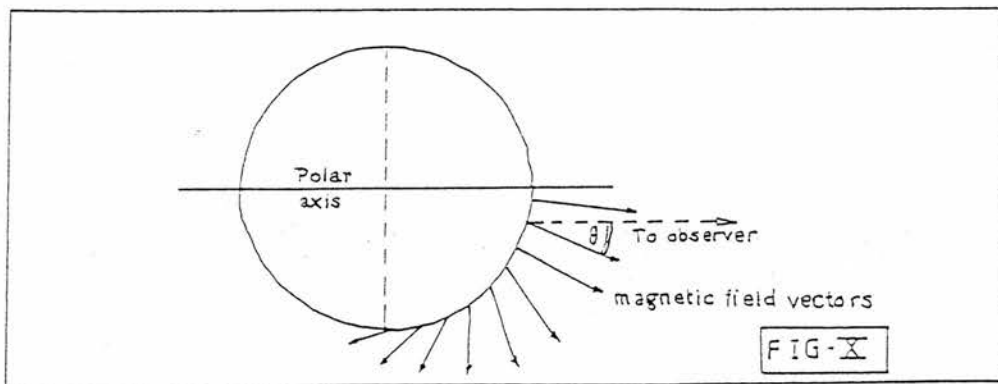
and the shift observed from the centre of gravity will be the same as that from a normal zeeman triplet under a field of $1.167 H_z$.

In this manner, the multiple components of the anomalous zeeman effect may be considered as a normal zeeman triplet multiplied by Z ,

$$d\lambda = 4.67 \times 10^{-13} \lambda^2 ZH \cos \theta \quad (1.50)$$

I.6 Disadvantages of the technique.

The principal disadvantage of this technique is that the zeeman displacements measured are the result of the integration of the magnetic field components over the hemisphere of the star towards the observer. No information is gathered about the real magnitude of the magnetic field distribution over the visible disc. Opposite field elements will cancel, and the field from a small magnetic region will be diluted by the light from the remaining non-magnetic region. To gain information on the field configuration it is thus necessary to acquire equivalent width measurements as in Hockey's (1969) and Adam's (1965) analysis of HD125248, or additionally radial velocity variations as in Deutsch's (1970) analysis (See Chapter III.2.1). For instance, if the star is treated as a uniformly magnetised globe (Babcock (1947)), the net shift observed, pole-on to the observer, will amount to only $0.311 H_{polar}$, due to the orientation of the field lines (fig (X)) and the restriction in only calculating H_z .



To overcome this, Robinson (1980) developed a technique to evaluate the absolute magnetic field by comparison of the blended profile, with a standard, magnetically inert, profile. His work will not be further detailed here save for the reference.

I.7.1 Methods of analysis.

To date, much of the determination of $\Delta\lambda$ has been conducted by visual measurement. Babcock used a measuring machine to calibrate the spectra to the arc measurements for line identification. The actual measurement of relative displacements between O and E spectra was conducted with recourse to Russell's rule for the determination of the centre of gravity of a blended, asymmetric profile: The centre of gravity of an asymmetric blended pattern may be taken to lie one quarter of the way from the strong component to the extreme weak component.

Much accuracy has since been gained by use of the Grant & Abbé comparators. The comparator described by Wolff and Bonsack (1972) functioned by overlaying the O and E spectra upon an oscilloscope display. By fine adjustments in steps of 0.5μ , the E spectra may be moved to maximum mutual line correspondence and the required shift recorded. For typical plate dispersions used, $3.4A^0mm^{-1}$, this resulted in an accuracy to $1.7 \times 10^{-3}A^0$. Despite this accuracy, the technique was laboriously slow, and still relied upon human judgement in evaluating the exact point of coincidence between the line profiles. To counter any personal-judgement bias to either the left or right, the plates were turned over and end for end, and a second set of measurements taken.

Considering the time needed for measurements, many weeks usually, and the reliance of the technique upon human judgement, the measurements could be greatly enhanced by an automated, fast, and accurate mutual-shift technique.

Weiss, Jenkers & Wood (1977) provided an alternative method for evaluating the optimum shift between the O and E spectra. By calculation of the sum of squared differences between spectrum densities, in the two spectra for

a range of trial mutual shifted amounts, a 'difference curve' may be plotted. This shows a minimum at the optimum shift, that may easily be evaluated by parabolic fitting. The procedure may be stated mathematically as,

$$d_j = \sum_{i=n_1}^{n_2} (x_i - y_{i+j})^2$$

where x_i = digitized density of reference spectrum

and y_{i+j} = digitized density of spectrum to be

shifted by a trial amount j

However, this technique is far from ideal, despite the increase in speed over the previous measurement system: Measurements must be taken over a range of $50 - 100A^0$ to achieve a high signal-to-noise ratio. No information pertaining to individual elements is gathered, and in ignoring the dispersive Z-values, though an accurate shift in microns is achieved, it may not be transformed into an effective magnetic field. This results in an accurate determination of the variations of a magnetic star, though no absolute values may be acquired.

Angel and Landstreet (1970), in attempting to measure the magnetic field variations of White Dwarfs and hence their rotation rate, proposed a measurement procedure based upon the detection of varying circular polarization in the wings of H_β lines. In such stars, where magnetic fields of order 10^4 gauss (Woltjer 1969) are expected, the conventional zeeman effect may not be used since 75% of the known white dwarfs are type DA and only broad Balmer lines may be measured. The effect of the magnetic field will not cause the centre of gravity of the profiles to move appreciably, though the splitting will blunt or round the core.

By observing the slight circular polarization in the Balmer wings, characteristic of the zeeman σ components, as a percentage of the total line intensity, a magnetic field may be obtained, knowing that a field of 10^5 gauss results in

0.65% polarization in the light admitted by a $30A^0$ filter. The magnetic field may then be evaluated from,

$$H_e(\text{gauss}) = 1.3 \times 10^5 P \quad \text{where } P = \text{percent}$$

Though developed for the study of dwarfs, the technique may be transferred to the study of Ap stars by using the wings of the H_β and a filter of $5A^0$, as was done by Angel and Landstreet for 53 Cam. This technique of H_β polarimetry has now been used by a number of authors leading (Borra (1974) and Borra & Landstreet (1977,1979) to put forward theoretical arguments stating that the photographic zeeman measurements suffer from systematic errors that distort the true shape. The observed photoelectric curves are found to be more harmonic than variations attained by the classical zeeman measurements. Borra and Landstreet state that this inconsistency can be explained by the fact that the classical measurement procedure is used on Iron group lines. As these are observed to vary and, the measured longitudinal field is weighted by equivalent width it is clear that the calculated H_z may bear little resemblance to the real field distribution. Additionally, the complex shape of the zeeman pattern and the aforementioned human intervention may cause systematic errors.

The photoelectric method, they argue, suffers from neither of these error sources, since measurement is totally automated, and concerned with hydrogen, whose distribution is expected to be uniform. However, as with all techniques independent of individual elemental measurements, though accurate in the attainment of the magnetic field, confers no information on abundance distributions.

These shortfalls motivated interest in measurement of the mutual-shift by means of cross-correlation. By automated measurements, human errors may be eliminated and the speed of measurement will be increased.

Cross-correlation has, for many years, been extensively utilised in radial

velocity, and galaxy velocity-dispersion work. It is thus strange that its ability to measure relative displacements to high accuracy has not been exploited in this very similar problem.

In evaluating the feasibility of this application, the theory behind cross-correlation must be considered.

I.7.2 Some basic Fourier theorems.

In the following sections a basic knowledge of the principles of Fourier theorems is assumed. Essential knowledge is briefly detailed below:

The fourier integral theorem states that if a function $f(x)$ satisfies the Dirichlet conditions on every finite interval, and if the integral,

$$\int_{-\infty}^{\infty} |f(x)| dx \quad (1.51)$$

is finite, then the fourier transform may be written as,

$$F(u) = \int_{-\infty}^{\infty} f(x) \exp\{-2\pi i u x\} dx \quad (1.52)$$

The corresponding inverse transform may be written as,

$$f(x) = \int_{-\infty}^{\infty} F(u) \exp\{2\pi i u x\} du \quad (1.53)$$

In many real cases, the function $f(x)$ is discontinuous, and composed of an array of discrete data points. In these cases, the transform is defined by,

$$F(u) = \frac{1}{N} \sum_{x=0}^{N-1} f(x) \exp\left\{\frac{-2\pi i u x}{N}\right\}$$

$$f(x) = \sum_{u=0}^{N-1} F(u) \exp\left\{\frac{2\pi i u x}{N}\right\}$$

for $x=0,1,\dots,N-1$ and $u=0,1,\dots,N-1$.

The fourier shift theorem states that if a function $f(x)$ has a transform $F(u)$, then the transform of $f(x - x_0)$ is found to be,

$$\mathcal{F}[f(x - x_0)] = F(u) \exp\{-2\pi i u x_0\} \quad (1.54)$$

With these two theorems, it is possible to envisage the effect of cross-correlation as will be detailed below.

1.8.1 ZCROSS: The cross-correlation program

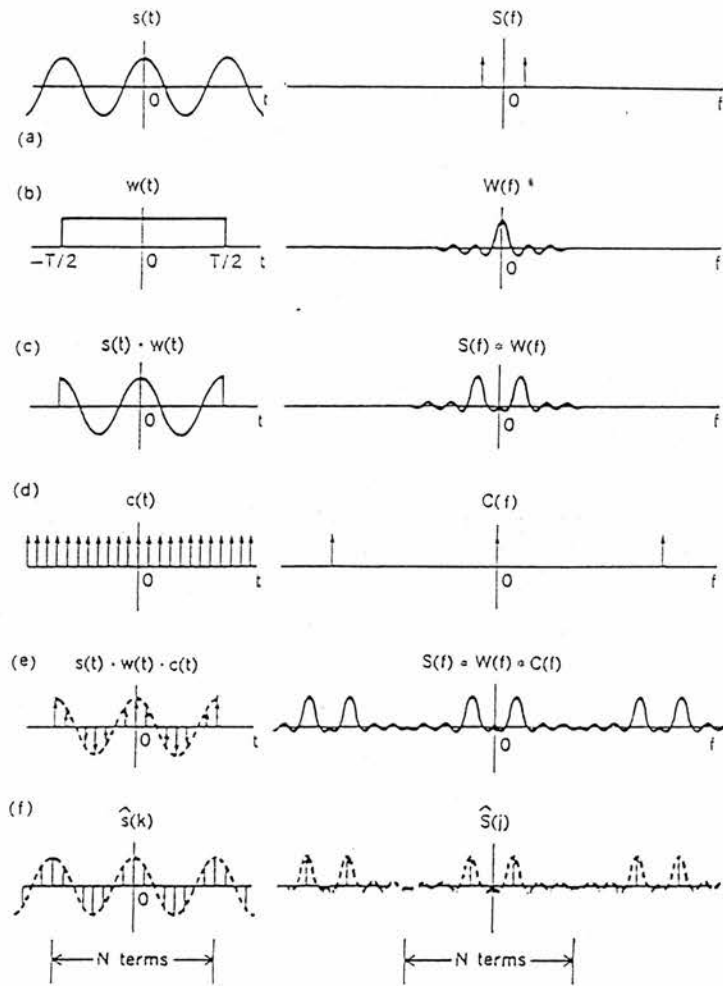
The cross-correlation program used in this research is an adapted version of VCROSS (Hill 1982). This program, ZCROSS, retains all of its predecessor's ability, with the additional feature that allows the processing of many lines individually from a line list.

The fast fourier transform (FFT) algorithm FOURS (Brenner 1970), an extension of Cooley and Tukey's (1965) algorithm is used to compute the fourier transform. This algorithm greatly reduces the computational time necessary by representation of the N data points in binary format. A direct fourier transformation of N data point would normally require N^2 complex operations, but by noting that in this format many integrals are duplicated or unity, the numbers of computations are reduced considerably as shown in fig (XI).

The inherent problems of any fourier transform using sampled data over a finite interval are reduced by tapering the end points with a cosine bell function. Additionally, the data are averaged and zeros are added to the end points to bring the entire data length to 120% of the initial window.

The necessity of this processing (Bergland 1969, Brault & White 1971, Brault & Piersol 1971, Simkin 1974) may be appreciated by considering the effects of sampling and the finite length of the data train.

FIGURE XII The Fourier coefficients of the discrete Fourier transform viewed as a corrupted estimate of the continuous Fourier transform.



After Bergland, the effects of a finite data train may be calculated by considering the signal as the multiplication of a rectangular 'box-car' function and the data. This multiplication results in the convolution of the fourier signal by a sinc function as seen in fig (XII). As the sinc function is not localized to one point in fourier space, nearby frequencies will be contaminated by its extended wings. This 'leakage' may be eliminated by choosing a window such that its

fourier transform is as localized as possible. One such function is Tukey's 'Interim window' or extended cosine bell, as in fig (XIII). The width of the sinc function may be further reduced by the addition of zeros to the data ends, since the width is inversely proportional to the data-train length.

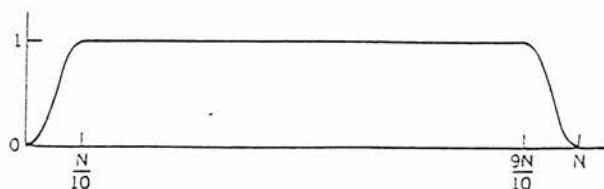
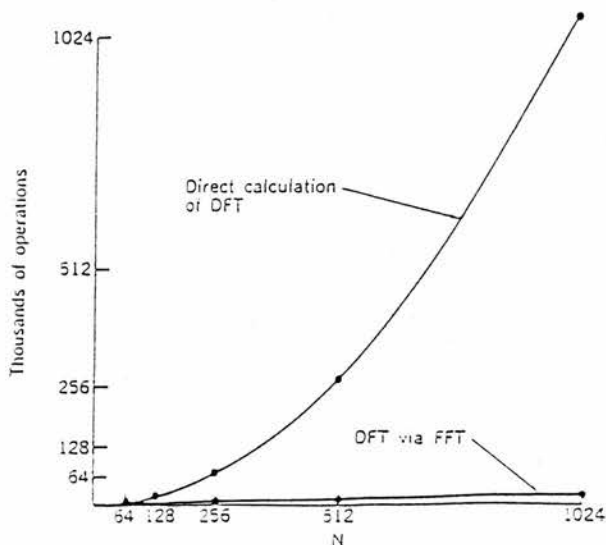


FIGURE XIII An extended cosine-bell data window.

The effect of discrete sampling can be regarded as the convolution of a row of delta functions and the data; the transform of which is depicted in fig (XIIId), causing an infinite number of replicas of the transform.

Lastly, the scaling of the data around the mean $\frac{D}{\langle D \rangle}$ is performed to remove the zero-frequency term. Neglect of this would give rise to a low-frequency spike and contamination similar to the sinc-function leakage. Likewise, it is important, when dealing with real data, that all continuum fluctuations are removed before transformation. Such trends will give rise to unwanted low frequency spikes and additional leakage.

FIGURE XI The number of operations required for computing the discrete Fourier transform using the FFT algorithm compared with the number of operations required for direct calculation of the discrete Fourier transform.



I.8.2 Cross-Correlation

The cross-correlation of two functions $f_c(x)$ and $f_p(x)$ is attained by computing their respective fourier transforms, $F_c(u)$ and $F_p(u)$. The comparison transform, $F_c(u)$, is subsequently multiplied by the complex transform of the program transform, $F_p^*(u)$, and the resultant inversely transformed to attain the 'Cross-correlation function' or CCF.

The following mathematics, will consider an upright gaussian, even though in the cases of physical interest the gaussian is inverted. The mathematics in both cases are identical save for the appearance of a continuum in the inverted case. Thus, to avoid this added term, the upright case will be dealt with, though the term depth will be retained so as to relate more to the physical picture.

To illustrate the effect of cross-correlation, consider a gaussian with depth D_0 , half-width σ , centred at λ_0 . The function $f(\lambda)$ is thus,

$$f(\lambda) = D_0 \exp \left\{ -\left(\frac{\lambda - \lambda_0}{\sqrt{2}\sigma} \right)^2 \right\}$$

Letting $\lambda - \lambda_0 = x$,

$$f(x) = D_0 \exp \left\{ \frac{-x^2}{2\sigma^2} \right\} \quad (1.55)$$

The fourier transform of $f(x)$ is (by eq.(1.52))

$$\begin{aligned} F(u) &= \int_{-\infty}^{\infty} D_0 \exp \left\{ \frac{-x^2}{2\sigma^2} \right\} \exp \{-2\pi i u x\} dx \\ &= D_0 \int_{-\infty}^{\infty} \exp \left\{ -\left(\frac{x^2}{2\sigma^2} + 2\pi i u x \right) \right\} dx \end{aligned} \quad (1.56)$$

To evaluate this, let

$$y = \left\{ \frac{x}{2\sigma^2} - i\pi u \sqrt{2}\sigma \right\} \quad dy = \frac{dx}{\sqrt{2}\sigma}$$

and thus,

$$F(u) = D_0 e^{2\pi^2 u^2 \sigma^2} \int_{-\infty}^{\infty} \sqrt{2}\sigma e^{-y^2} dy \quad (1.58)$$

$$F_t(u) = D_0 \sigma \sqrt{2\pi} \exp \{-(2\pi^2 u^2 \sigma^2)\}$$

It is thus seen that the fourier transform of a gaussian is another gaussian in fourier space. Applying the shift theorem, a gaussian centred at $x - x_0$, would have a transform equal to,

$$F_s(u) = D_0 \sigma \sqrt{2\pi} \exp \{-(2\pi^2 u^2 \sigma^2 + 2\pi i u x_0)\} \quad (1.59)$$

By taking the complex conjugate of this, multiplying by eq(1.52), the transform of the undisplaced gaussian, and taking the inverse transform,

$$F_s^*(u) F_t(u) = D_0^2 \sigma^2 2\pi \exp(-4\pi^2 u^2 \sigma^2 - 2\pi i u x_0)$$

$$f_t(x) = \mathcal{F}(F_s^*(u) F_t(u)) = \frac{1}{2\pi} \int_{-\infty}^{\infty} D_0^2 \sigma^2 2\pi \exp \{-(4\pi^2 u^2 \sigma^2 - 2\pi i u x_0)\} du$$

Letting,

$$y = \left(2\pi u \sigma - \frac{i}{2\sigma} x_0 \right)$$

$$f_t(x) = \frac{D_0^2 \sigma^2}{2\pi \sigma} \int_{-\infty}^{\infty} \exp \left\{ y^2 - \frac{1}{4\sigma^2} x_0^2 \right\} dy$$

$$= \frac{D_0^2 \sigma^2}{2\pi \sigma} \exp \left\{ -\frac{x_0^2}{4\sigma^2} \right\} \int_{-\infty}^{\infty} \exp(-y^2) dy$$

$$f_t(x) = \frac{D_0^2 \sigma^2}{2\pi \sigma} \sqrt{\pi} \exp \left\{ -\frac{x_0^2}{4\sigma^2} \right\}$$

the cross-correlation function is seen to be,

$$\text{CCF} = f_t(x) = \frac{D_0^2 \sigma}{2\sqrt{\pi}} \exp \left\{ -\frac{x_0^2}{4\sigma^2} \right\} \quad (1.60)$$

This corresponds to a gaussian centered at $(x - x_0)$, the shift between the two original gaussians.

For the case of inaccurate matching of the parameters D_0 and σ , eq(1.60) may be expanded to incorporate D_{0_1}, σ_1 (parameters for one gaussian) and D_{0_2}, σ_2 for the the second, as below.

$$f_t(x) = \frac{D_{0_1} d_{0_2} \sigma_1 \sigma_2}{2\sqrt{\pi(\sigma_1^2 + \sigma_2^2)}} \exp \left\{ -\frac{x_0^2}{4\sigma^2} \right\} \quad (1.61)$$

Despite the non-identical parameters, eq (1.61) still represents a gaussian centered at $(x - x_0)$ but the width of this cross-correlation function will be reliant upon the greater of the two widths.

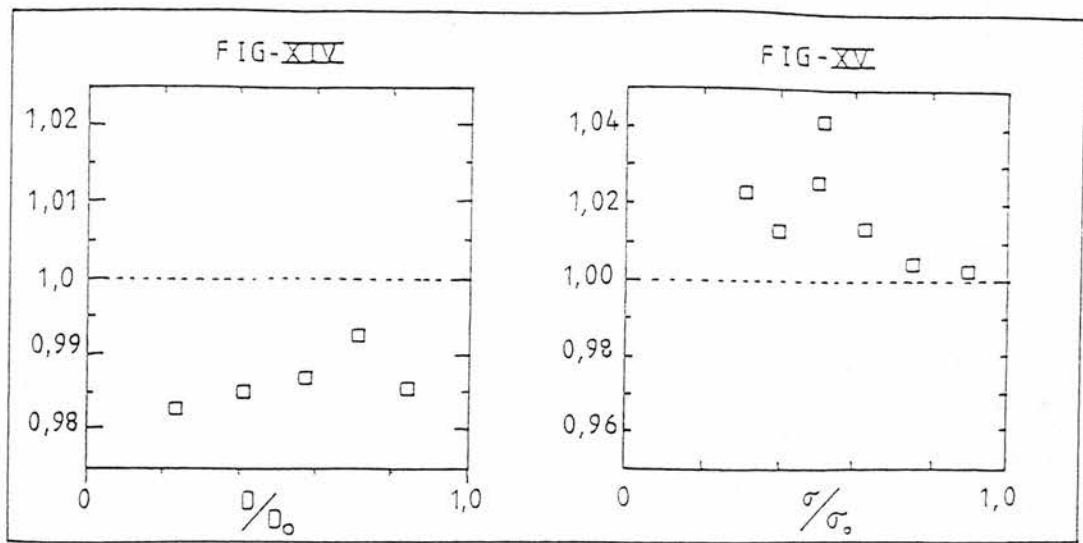
The central depth of the gaussian is also affected by dispersion of the initial gaussian parameters.

Consider the case of an ideal gaussian, depth D , width σ . Let $D_{0_1} = D + \delta D$, $D_{0_2} = D - \delta D$ and $\sigma_1 = \sigma + \delta\sigma$, $\sigma_2 = \sigma - \delta\sigma$. Forcing these results into eq(1.61),

$$f_t(x) = \frac{(D^2 - \delta D^2)(\sigma^2 - \delta\sigma^2)}{2\sqrt{\pi(2(\sigma^2 + \delta\sigma^2))}} \exp \left\{ -\frac{x_0^2}{4\sigma^2} \right\} \quad (1.62)$$

Comparing this with the result for D, σ for both gaussians, it is evident that the central depth of the resultant profile has been lowered. Although in the case of a single line cross-correlated with another single line this lowering will be inconsequential, when noise is present in the lines, this will cause a lowering of the signal-to-noise ratio to the detriment of accuracy.

To test the resilience of the cross-correlation peak position with dispersive parameters, a gaussian of $D = 0.7$ and $\sigma = 100\text{mA}$ was cross-correlated with varying depth and width. Figures (XIV,XV) depict the results of this single line cross-correlation, and show that, for an isolated gaussian, the placement and



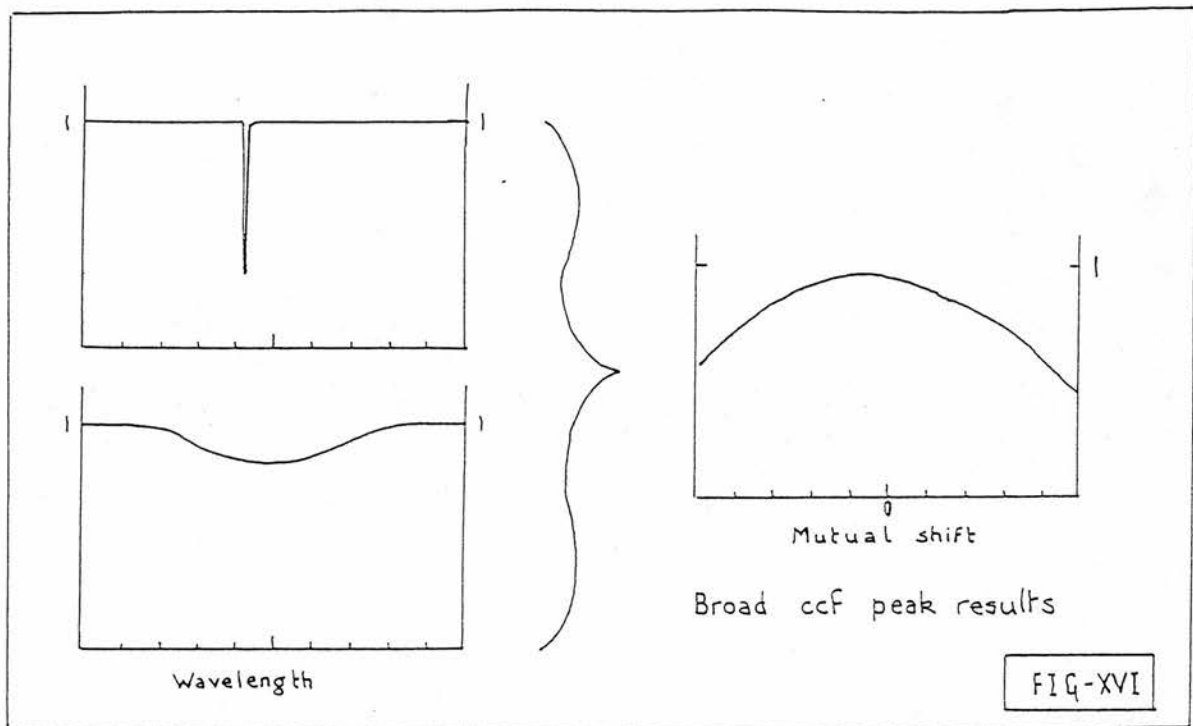
accuracy of the cross-correlation profile is very resilient to even great disparity between parameters.

The simple co-existence of the required line with unwanted 'noise', such as continuum fluctuations, adjacent spectral lines, and plate grain, will produce peaks in the cross-correlation function.

To illustrate this, consider a large σ , small depth, gaussian cross-correlated with a sharp spectral line. Eq(1.62) predicts a peak in the cross-correlation function whose position corresponds to the mutual shift in wavelength. Figs (XVIabc) depict the functions and the resultant cross-correlation function, showing the extent to which this occurs in practice.

Fig (XVIb) may be thought of as a continuum variation whose unwanted presence will cause blending in the cross-correlation peak and an inaccurate shift determination. Fig (XVII) shows this 'continuum variation' superimposed upon a replica of the sharp line considered. The resultant peak (fig (XVII)) shows that the peak caused by the continuum variation, though visibly unnoticeable, has shifted the determined position of the peak, from the expected value of -2.40 to -2.52.

Although the inaccuracy introduced by this blending is reduced by the normalization of the cross-correlation function (Simkin 1974), as mentioned earlier, it may be eradicated by careful delineation of the continuum level in



the rectification stage of data processing.

This is in contrast to the problems of line blending and random noise, although the effect of the latter may be limited by a smoothing algorithm.

Fig - XVI a

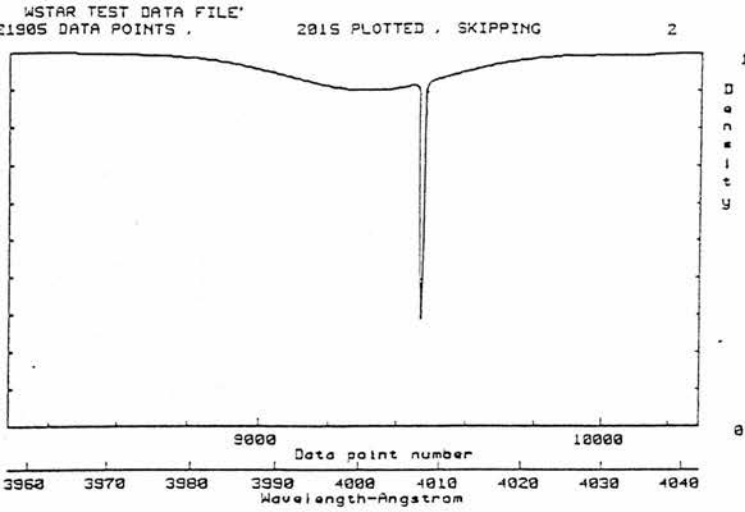
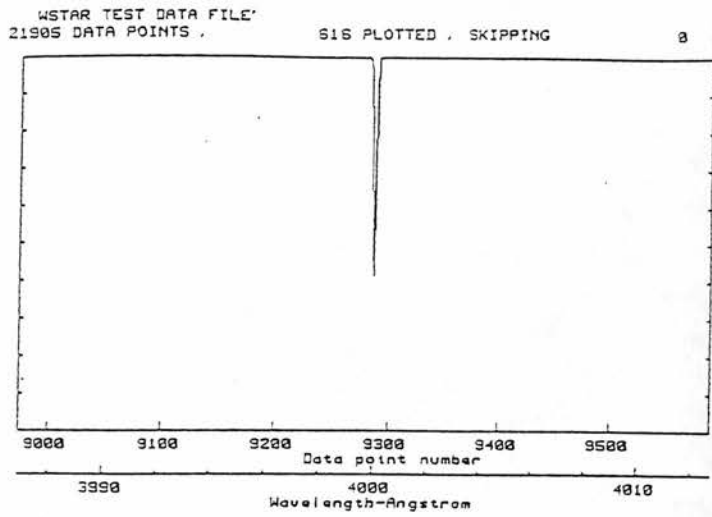


Fig - XVI b



Plot: (X)S%WHM; Skip: DFC; Measure: TT, function G, std profile P, E=End
Fit function to window: 1=Gauss, 2=Lorentz; End with A for all data, OI*

Program * R741AS KE741A HD49976 -4.78 4202
Comp * R741AM KE741A HD49976 -4.78 4202 RU 0.00 k/s

D(lam): -0.0352 +/- 0.0000 d(RV) -2.52 +/- 0.00 RV -2.52

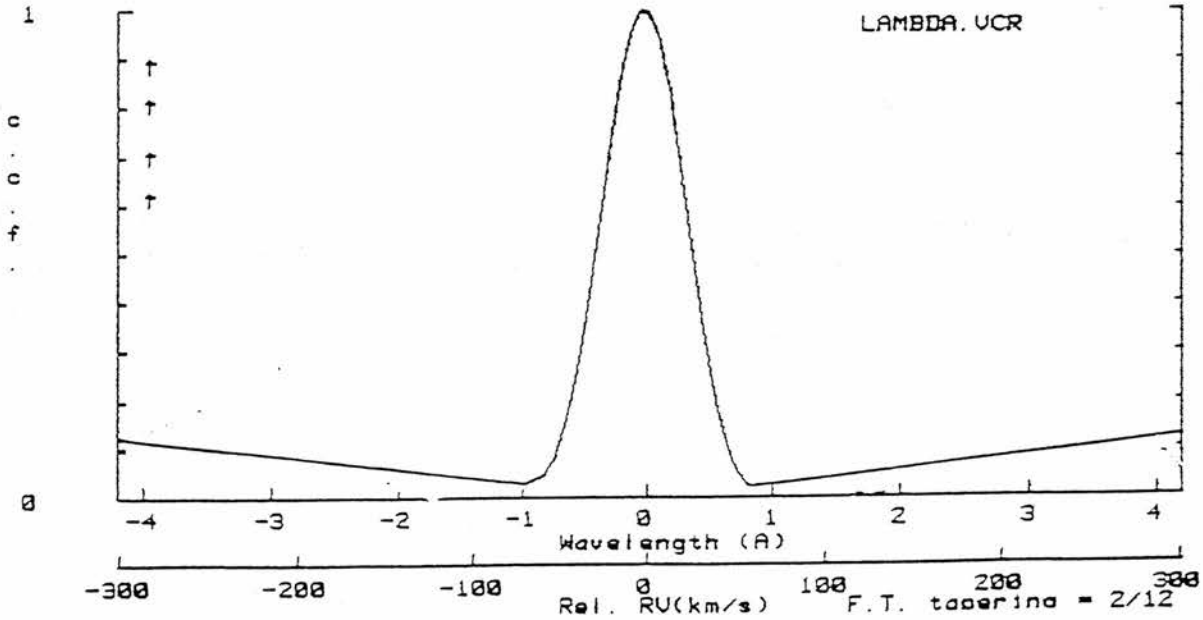


Fig - XVI c

I.8.3 The Noise-generation algorithm

In order to study the effects of line blending and random noise, an algorithm for noise generation was created. In this way, noise of varying amplitude could be superimposed upon synthetic lines, and the blending evaluated by consideration of the error introduced to a pre-determined mutual shift between lines under consideration.

To simulate accurately the conditions that prevail in real spectra, a selection of plates (Sect. II) were studied to reveal the 'noise' distribution. Wavelength sections devoid of major lines according to Striganov (1968) and a line list provided by Bonsack, were studied revealing small variations. These fluctuations, of average depth 0.07 and half-width $0.1 A^0$, were identified with inherent plate grain in the spectrograms. The distribution of separation between grains was found to approximate a bell-shape distribution around a separation of $0.2 A^0$. The distribution function is thus taken as,

$$\text{noise position}_{(n+1)} = \text{position}_n + 0.3 + R \quad (1.63)$$

Where R is a random number between -0.1 and +0.1, based upon the position given from a bell-shape distribution.

The starting wavelength for the addition of noise is first identified, and a new wavelength position produced by the addition of the mean noise separation. To simulate the bell-distribution, a random number is subsequently generated which produces an additional shift in accordance with the distribution function, given in Eq.(1.63).

This final position is then taken as the central position of the noise fluctuation and a gaussian profile generated. The profile parameters were then generated with recourse to Eq. (1.64)

$$D_{noise} = \text{Noise level} \times R_{-1to+1} \quad \sigma = \frac{150 \times \text{noise level} \times R}{D_n \times \sqrt{2\pi}} \quad (1.64)$$

To simulate both the effects of small-scale fluctuations such as plate grain, while at high noise levels, causing noise in the form of sharp-line blending, the parameter 'Noise level' is varied in proportion to the quantity of noise required.

Though small-scale noise is rarely gaussian in shape, the exact profile is comparable with the gaussian approximation, and the difference should cause little inaccuracy.

The process is then repeated producing high-frequency noise across the spectral range required, approximating the noise present in the studied spectrograms. Although this method does not undertake to simulate very strong noise-lines, or lines with extended wings, it is presumed that in this case the blended moderate-strength line under consideration could be seen visually as blended and would be removed from consideration. It is the effect of small- to medium-scale noise that is most important, as visual observations of a line may not reveal the presence of this noise. Consequently, erroneous mutual- shifts may be measured.

I.9.1 Methods of measurement

With the ability to cross-correlate not only individual lines, but many lines simultaneously and, additionally, to generate a smooth comparison template, the possibilities for a new measurement system arise. Consequently, five distinct methods are suggested, requiring error evaluation to determine the optimum approach to shift measurements. These five methods are given briefly below:

i.) The classical measurement system -

Measurements are obtained from the mutual displacement between O & E spectra, line by line.

ii.) Template measurement system -

Shift to be obtained by cross-correlating both O & E spectra with a noise-free template, the difference determining the magnetic field.

iii) Spectral linearization by $-\frac{1}{\lambda}$ -

In analogy with the $\ln(\lambda)$ linearization in radial velocity, the formula for the magnetic field suggests linearization $-\frac{1}{\lambda}$.

iv.) Line grouping by Z -

To remove all dispersion of parameters in Eq (1.50). Cross-correlate many lines with similar $Z\lambda^2$.

v.) Weiss measurement system -

The measurement scheme proposed by

The five methods may be grouped into two broad categories: Those that measure line shifts individually, (i) & (ii), and those that cross-correlate many lines simultaneously, namely (iii),(iv) & (v).

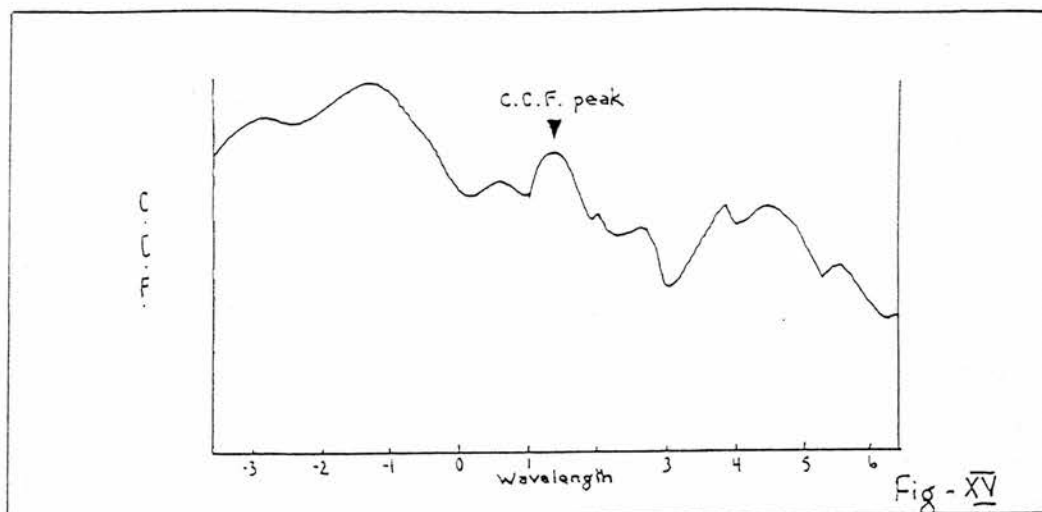
I.9.2. Individual line determinations

I.9.2.1 The classical measurement system.

This method, though a seemingly direct replication of the classical determination, requires additional considerations arising from the use of cross-correlation procedures. The accuracy of the cross-correlation procedure, and specifically the fourier transform calculation, reliant upon the similarity between the two spectra, should be improved with respect to the template system (see I.8.2.2). Line profiles in both spectra are similar, as are continuum levels. Furthermore, lines may be measured within the wings of the hydrogen lines, whereas a template measurement system would prove innaccurate due to the non-replication of the sloping continuum at this point (Section (I.8.1)).

The principal disadvantage arises from the cleanliness of both spectra. Incident and adjacent features to the studied line will cause peaks in the cross-correlation function, resulting in inaccurate shift determinations. More importantly, correlation of noise-with-noise, may at high noise-levels mask the position of the real cross-correlation function peak. Such masking is evident in Fig (XV), clearly showing the difficulty in interpretation of the CCF.

By definition of the cross-correlation window such that adjacent 'noise' features are excluded, this problem is apparently overcome. However, in narrowing the window, spectral leakage caused by the window fourier transform is increased, resulting in additional contamination of the cross-correlation profile. The limit to which the window may be narrowed is also well defined, being the



line width resulting from co-adding the O and E spectra. Further narrowing will eliminate data points in the wings of either or both spectra, resulting in a faulty fourier transform, and errors in accordance with this.

Using the line and noise-generation algorithm to obtain measurements of probable errors, cross-correlations were conducted for increasing noise level. Since the magnitude of any peak in the cross-correlation spectrum is primarily dependent upon the central depth, D , the definition of 'Noise level' was taken to be the ratio of the noise central depth to that of the studied line.

To illustrate the necessity of tight window fitting to the studied line, a broad window of 10 angstroms width was taken. The results of this error evaluation procedure are given in Table (II).

—Table (II)—

Noise level	Mean H value	Standard error
0.000	2000.000	7.0
0.010	1991.000	36.0
0.030	2012.000	71.0
0.071	2054.000	106.0

0.140	2180.000	334.0
0.210	2773.000	863.0
0.280	3343.000	1272.0

Expected value of H = 2,000 gauss

The errors quoted are the standard errors of the sample mean, in Gauss.

Above a noise level of 30%, many cross-correlation profiles are blended to an extent where the expected peak is invisible in a large proportion of the test correlations. In the few cases where a peak may be discerned from the background, it leads to inaccuracy in excess of 100A noise level of 30% thus defines the limit to which this technique may be used with any accuracy.

In contrast to this, a window of 2.0 angstroms width, defined to the wings of the line, provides a better signal-to-noise relation as in Table (III).

—Table (III)—

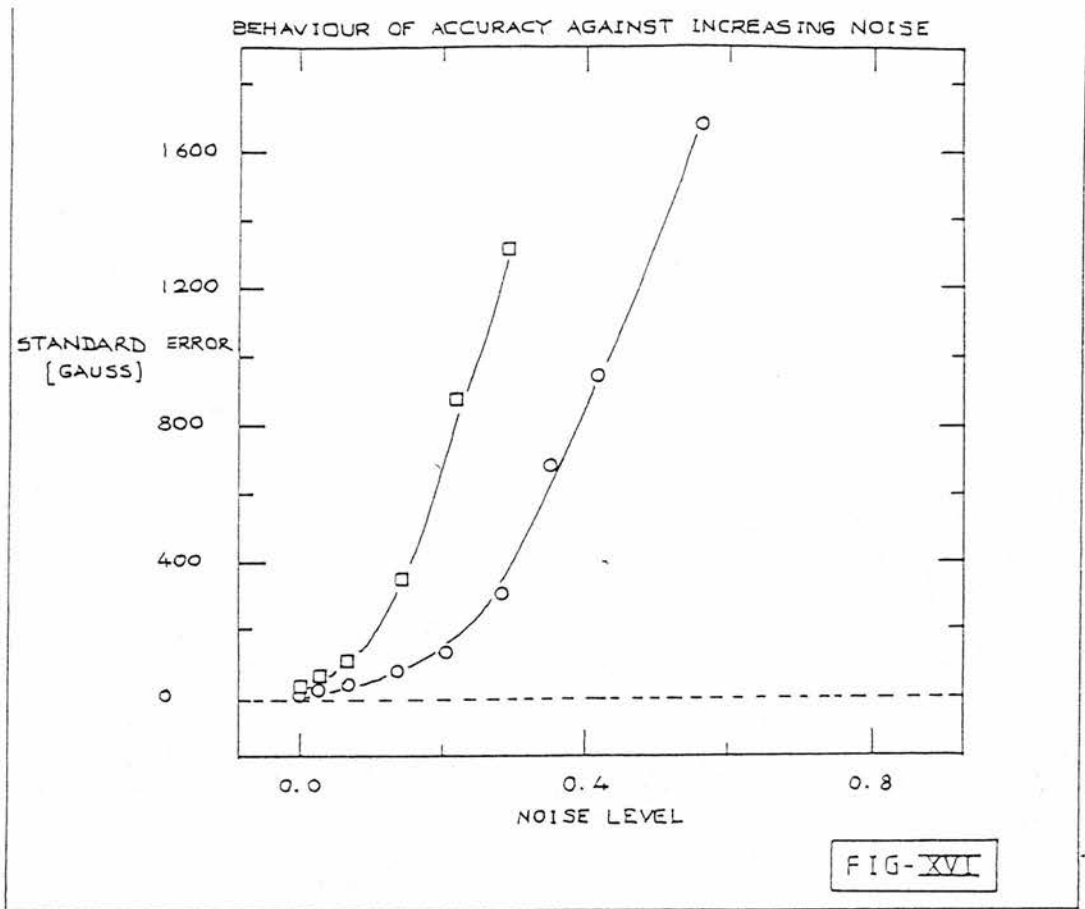
Noise level	Mean H value	Standard error
0.000	2000.000	1.0
0.010	1995.000	5.2
0.030	1948.000	12.0
0.071	1823.000	41.4
0.140	1989.000	75.2
0.210	2181.000	130.8
0.280	1609.000	303.1
0.350	3177.000	1040.0
0.420	2314.000	942.0
0.560	4008.000	1681.0

Expected value of $H = 2,000$ gauss

It is seen that the limit to measurement now occurs at a higher noise level, on fitting the window to the limit of the line wings. A noise level of 60% is expected to form the limit of the technique, in contrast to the 30% arrived at previously.

Fig (XVI) shows both data sets and illustrates that the onset of inaccuracy is delayed. Until a level of 20% noise is reached the errors incurred are found to remain low, and relatively insensitive to small noise-level variations. Thus in the magnetic field determinations, lines must be chosen so as to give a noise level lower than 20% for maximum accuracy, as after this level, errors rise considerably. Based upon the measurements of real plate noise, this corresponds to a lower limit of 0.35 central depth, which would eliminate the majority of spectral lines. The mean central depth for lines of interest is approximately 0.20, which would produce a noise level of 0.35 and corresponding errors of ± 700 gauss.

Since this error is the result of a large sample, it may be regarded as the best possible result obtainable. For a small sample of lines, the errors could be expected to rise, and the mean H_z vary accordingly. However, the sample size should not be augmented by considering shallow/weak lines, since the determinations from these lines will act to the detriment of the overall accuracy.



I.9.2.2 Template measurements

The logic of applying a template comparison to measure the relative shifts of lines in both O and E spectra is not immediately obvious since the only apparent difference is to introduce an additional error. As the measurement of precise peak position is completed by parabolic curve fitting, a measurement of first O, then E against a template, and subsequent subtraction to determine O-E, involves two fittings. Incident noise will bias this fitting if the line is non-symmetrical, and hence additional errors arise.

Secondly, as mentioned previously, the template, unless intricately constructed, will introduce errors arising from the mismatching of line parameters, giving rise to a lower cross-correlation peak.

The advantage of this approach is to eliminate all unwanted 'noise' from one spectrum, resulting in a clean line against which to cross-correlate the O and E spectra. The cross-correlation of line-with-line is performed as before, as is the cross-correlation of line-with-noise. However, no noise-with-noise cross-

correlation occurs, and the clarity of the expected peak in the cross-correlation spectrum is enhanced.

The cross-correlation process will produce a number of peaks dependent upon the number of permutations of line combinations. Three lines in one spectra cross-correlated with three in the second will produce a cross-correlation spectrum containing 9 peaks of varying size. If two of the lines are considered as 'noise', the cause of the profile masking, defining the limit of the previous method, is evident. By the application of a template, at most there can be only three peaks in both O and E cross-correlation spectra, adding considerable accuracy. It is thus expected that the noise level to which the template technique may be used, should be greater than previously attained.

Testing of the procedure subsequently proved that such is the case. The results of this (Table (IV).), show that the noise level upper limit has been greatly improved. At low noise levels it is also evident that the use of a template detracts from the accuracy, due to the additional computational requirements of the method.

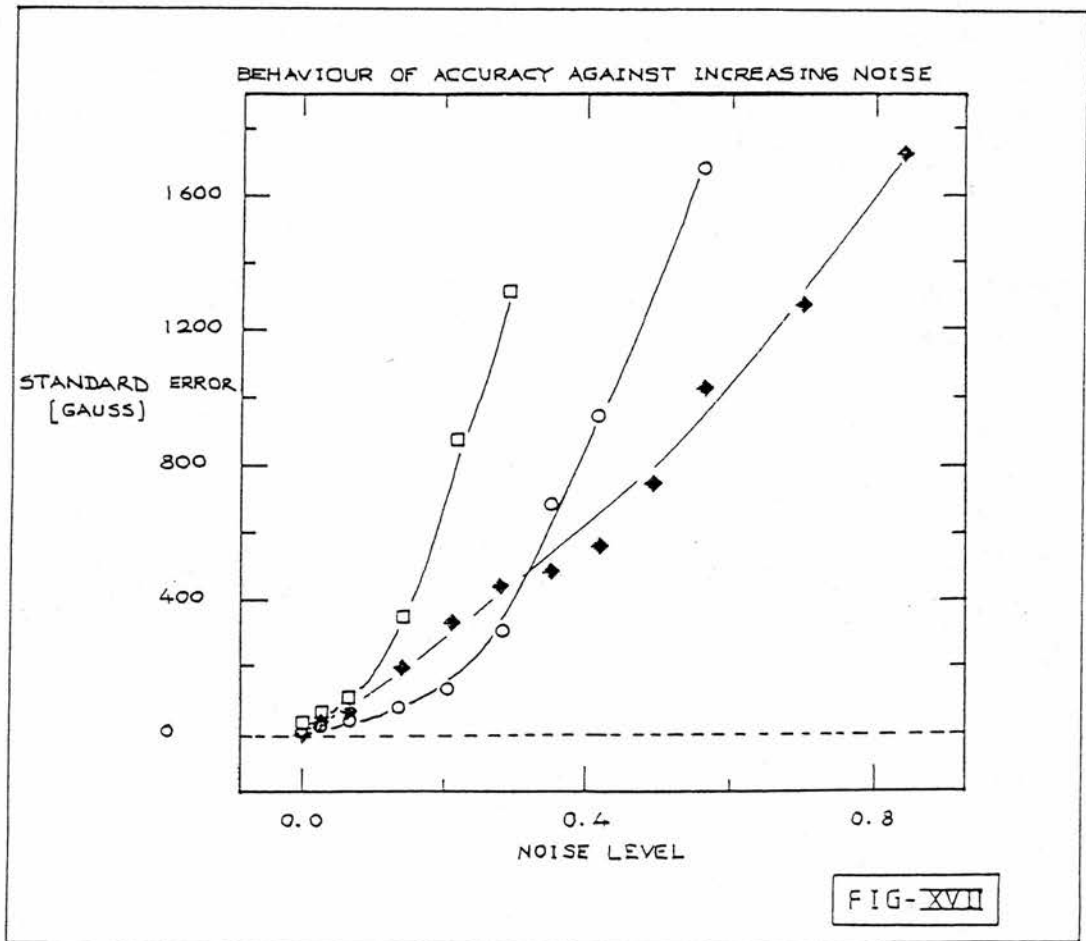
---Table (IV)---

Noise level	Mean H value	Standard error
0.000	2000.000	0.67
0.030	2058.000	17.10
0.071	2132.000	70.00
0.140	1998.000	208.00
0.210	2592.000	339.00
0.280	1591.000	443.00
0.350	1573.000	452.00

0.420	1633.000	564.00
0.490	2005.000	743.00
0.560	3348.000	1030.00
0.700	756.000	1280.00
0.840	3044.000	1731.00

Expected value of $H = 2,000$ gauss

For purposes of comparison, the errors incurred from the two processes, Template and Classical are shown in fig (XVII).



I.9.3 Comparison of individual line methods

From fig (XVII) the optimum measurement system may be chosen by calculation of the expected noise level. At high noise level, the template must be applied, though at levels below the cross-over point the classical determination scheme is favoured. In the calculation of the 'noise level', it must be remembered that, 'noise' is defined as small-scale fluctuations, in this case intrinsic plate noise, and weak blending.

In the spectra of HD49976, the mean central line depth of 0.2 corresponds to a noise level of 40%. For maximum accuracy, a template is thus suggested, although this value lies close to the cross-over point, and both methods should be applicable.

I.9.4 Simultaneous line-measurement methods

I.9.4.1 Linearization by $-\frac{1}{\lambda}$

Though linearization by $\ln(\lambda)$ is essential in radial velocity work, linearization by $-\frac{1}{\lambda}$ should not enhance the studied measurement process significantly. Apart from the implementational problems in ZCROSS, from consideration of the magnetic shift (Eq. 1.50), it is seen that wavelength and magnetic field do not totally define the shift. The free parameter, Z , still results in a diffuse peak since its variation is independent of other variables.

This dispersion may be removed by cross-correlating groups of lines with similar values of Z . The distribution of Z for usable lines, supplied by Bonsack, fig (XVIII), shows that by cross-correlating groups of three lines simultaneously, the dispersion previously observed may be eliminated, since many clusters of similar Z appear. In so doing, the 'effective noise level' may be reduced, since by cross-correlating three lines simultaneously, the probability of noise correlation within the three lines is lowered.

Linearization by $-\frac{1}{\lambda}$, creates sampling difficulties. The linearization involves interpolation between data points to create an evenly spaced data set. Since the expected shift is of the order of $0.0198A^0$, any loss of data due to undersampling would increase the error in this determination.

For a spectrum sampled at intervals of $0.042A^0$, the $\ln(\lambda)$ linearization demanded in radial velocity work, would create a data sampling interval of $0.039A^0$ at $3610A^0$, decreasing to $0.0489A^0$ at $4530A^0$. Neither end is greatly under or oversampled, since the difference in sampling amounts to no greater than 14%. In contrast the linearization by $-\frac{1}{\lambda}$ results in a sampling interval of $0.035A^0$ at $3610A^0$ decreasing to $0.055A^0$ at $4610A^0$. This causes the red end of the spectra to lose approximately 30% of its data points. As this section is most rich in usable lines, this loss of data would severely countermand any advantages from decreased 'effective noise'.

I.9.4.2 Line grouping by $Z\lambda^2$

A logical extension of the previous method would be to cross-correlate groups of lines with the same $Z\lambda^2$. By removing all free parameters from Eq. (1.50), the amplified effect of three lines with comparable shifts should produce a visible and accurate peak in the CCF. An e.d.f. format for the distribution of $Z\lambda^2$ (fig(XIX)) illustrates that at a value of $Z\lambda^2 = 2.6 \times 10^7$ many lines have comparable values, and the technique may be applied without incurring large errors due to variation of $Z\lambda^2$ within a group. A bar indicating the errors incurred in utilising a spread in $Z\lambda^2$ of the appropriate value is shown along the axis. An error of ± 100 gauss would thus be incurred at values of 1×10^7 in order to incorporate three lines into a line group, decreasing to ± 50 gauss at around $2 - 3 \times 10^7$.

In order to gain optimum accuracy, it would be necessary to forego information on magnetic field variations for individual elements, since different

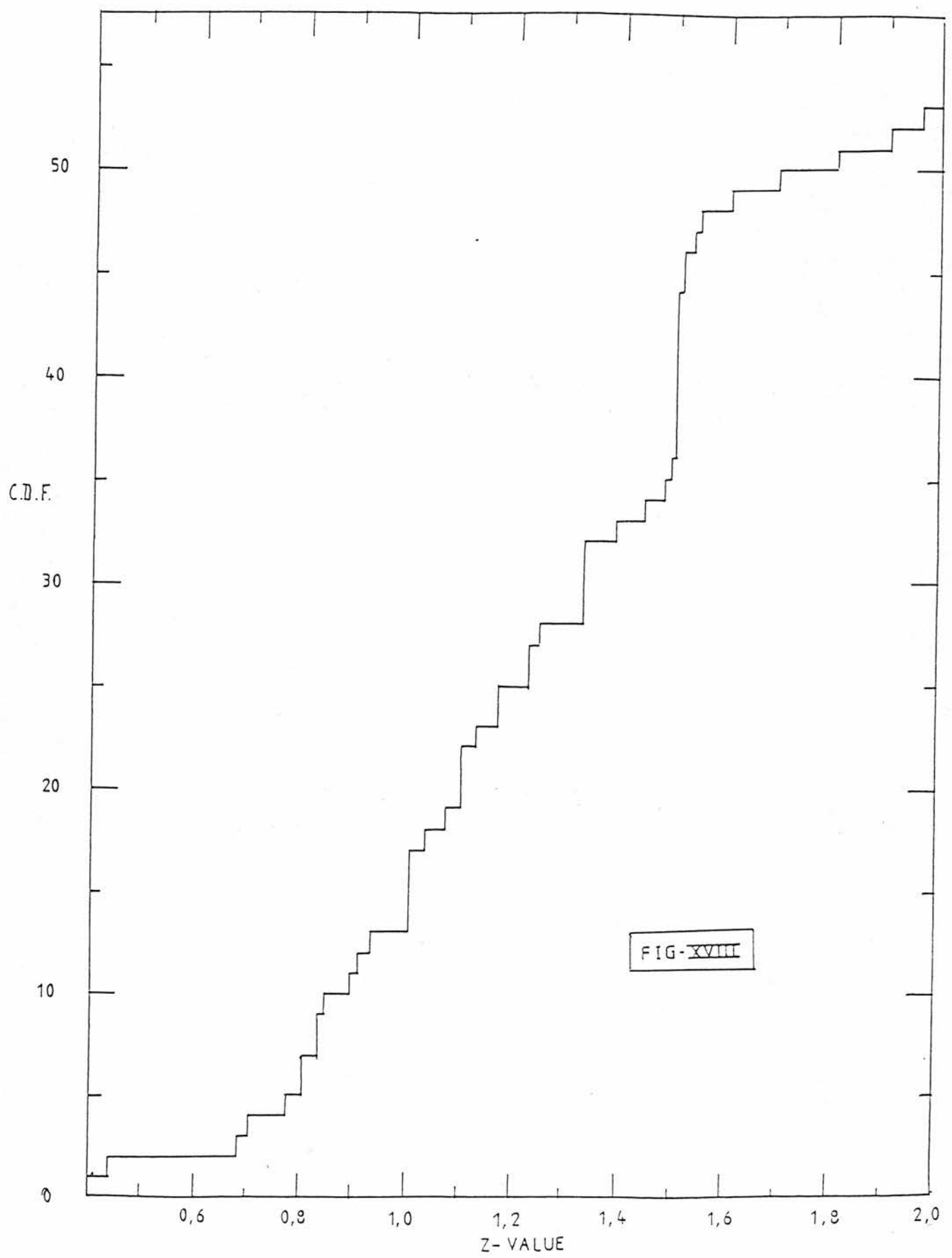


FIG-XVIII

elements may be required to be cross-correlated in the same group. If, additionally, the surface distribution of individual elements differs considerably, causing different integrated fields to be measured, dispersion of measured shifts would occur within these mixed groups, and the resultant cross-correlation peak broadened, to the detriment of accuracy. The possible advantages are thus annulled by the above considerations and loss of elemental information.

I.9.4.3 Weiss et al. determination method

Of the three methods devoid in elemental information, the technique proposed by Weiss et al. (1977) is most feasible. By cross-correlating a large $50 - 100A^0$ wide section, the effects of noise are greatly diminished. The resultant width resolution of the cross-correlation peak is totally dependent upon the dispersion of the free parameters: wavelength, Z-value and the magnetic field. Since elements are not segregated in the technique and the calibration of shift to magnetic field is unknown, at present the technique can only show the existence or non-existence of a magnetic field, and the variation over phase.

In order to calibrate the shift measurements to the magnetic field, a mean value of Z and wavelength must be attained, for substitution into Eq (1.50). Bonsack (1987) suggests that since a great amount of information is already lost, that the simple approximation of $Z_{(eff)} = 1$ would outweigh the difficulties of attempting a further detailed analysis. Further consideration must still be given to an appropriate value of effective mean wavelength.

It is apparent that if all lines created a peak of equal height in the cross-correlation spectrum, then the mean of the free parameters $Z\lambda^2$ would totally define the calibration factor necessary to attain the magnetic field. The blending of the multiple line cross-correlations would create a peak centred upon the shift required for a magnetic field H, the dispersion in $Z\lambda^2$ acting only to broaden the peak.

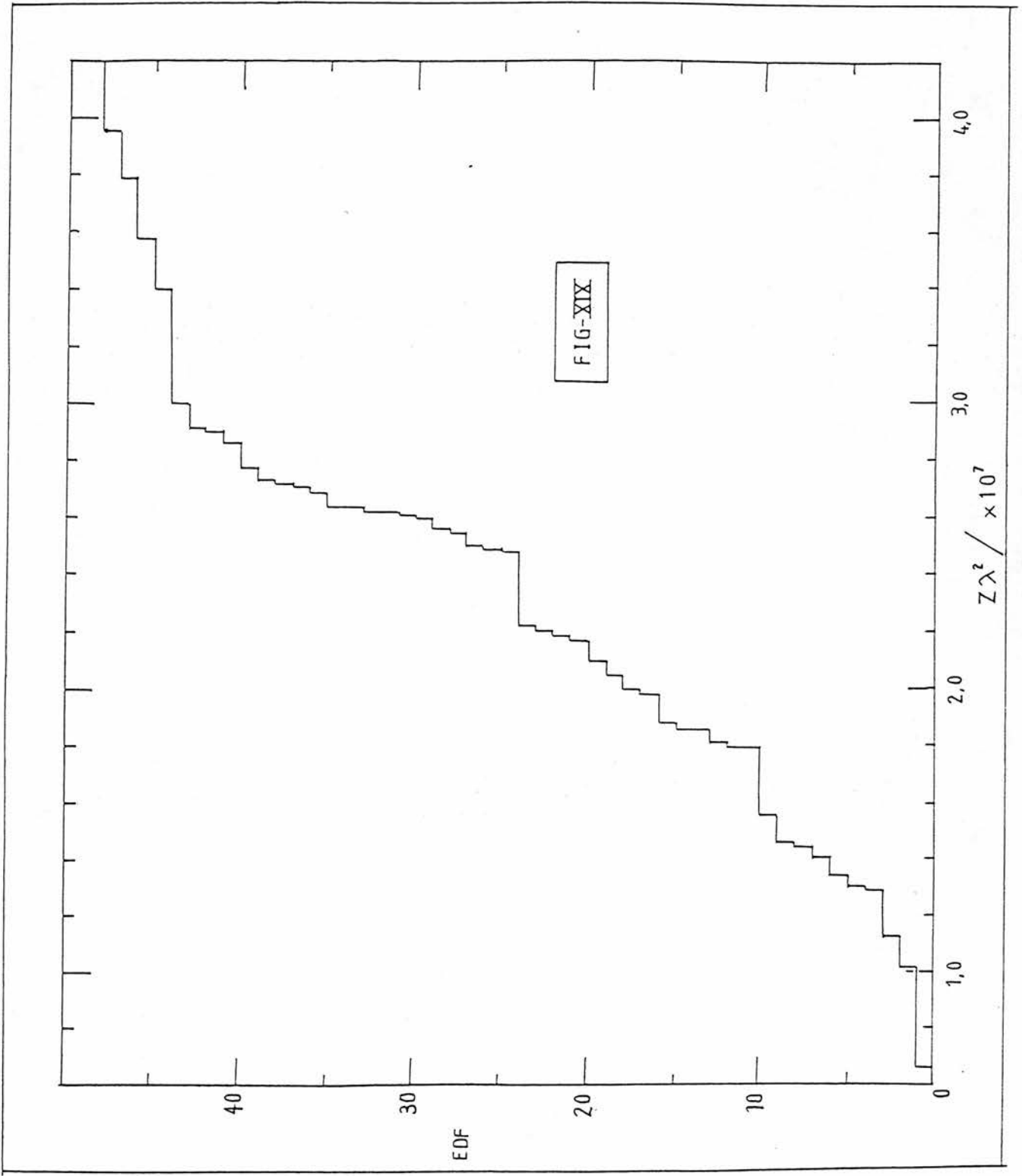


FIG-XIX

For lines of differing strength, the evaluation of a mean $Z\lambda^2$ requires a weighting mechanism. Such a system is suggested by Eq (1.60).

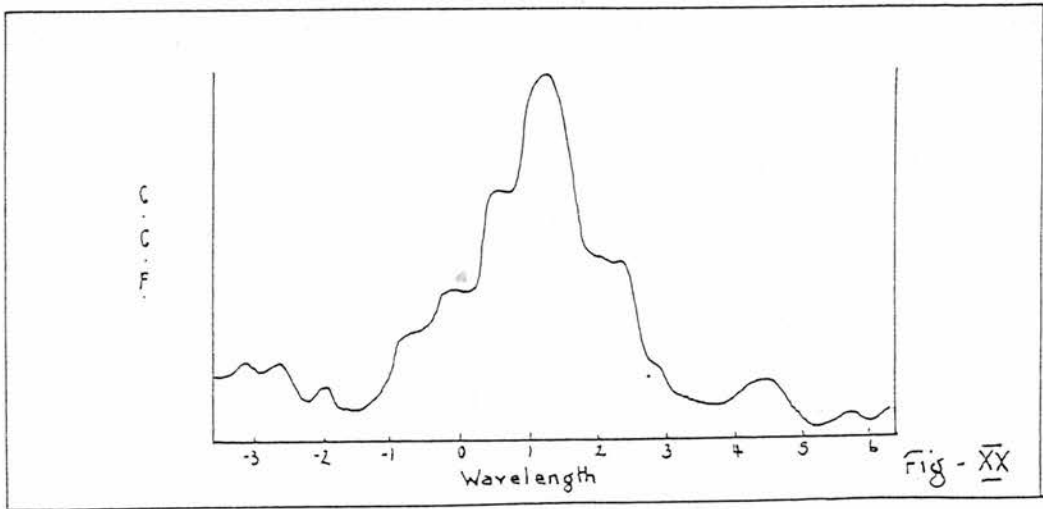
Consider all lines to have the same width σ . Then the intensity of the cross-correlation peak for an individual line will depend only upon the value of D_0^2 . Thus the mean value of $Z\lambda^2$ may be evaluated from the individual line wavelengths and Z -values, weighted by the respective central depth squared. To test the validity of this weighting, lines of set wavelength and Z , were varied in central depth, in groups of three in order to study the variations in displacement of the measured shift, as a function of the varying line strengths. No noise was introduced into the spectra, and cross-correlation was performed, O with E.

It is found that, despite the fixed parameters $Z\lambda^2$, the measured shift arising from the ensemble varies. To account for this within the framework of no weighting, the error in measurements would have to be 16%. Since the noise level is zero, from fig (XVII), this is clearly impossible. Weighting by D_0 still results in an uncharacteristic 5%, whereas weighting by D_0^2 results in an error of only 1.7%. Considering the intrinsic normalization of the cross-correlation program, this error would be within the expected error. Consequently, a weighted mean value of $Z\lambda^2$ for all lines within the wavelength window, weighted by D_0^2 , should provide the necessary calibration.

Though this method discards much useful information it has the advantage of a fast speed of operation. A star could thus be scanned for a magnetic field, and quickly calibrated to attain a first approximation to the global field intensity. Subsequent investigations of elemental magnetic fields, by the individual line methods, could then be undertaken, if a magnetic variation was observed. If no variation was observed, the method saves the time and difficulties that a full investigation would entail.

I.10.1 Smoothing

Though the errors incurred from line blending and plate fluctuations have been evaluated, in real spectra, a third source of inaccuracy is found to occur. For wide spectral lines, the gaussian profile is found to have many sharp lines superimposed upon it. On cross-correlation, this situation, illustrated in fig (XX), creates a primary cross-correlation peak convolved with multiple smaller peaks from the cross-correlation of the secondary lines. Parabolic fitting to such a cross-correlation peak now results in a highly inaccurate mutual shift measurement for the primary line. In order to measure the primary line, removal of the secondary peaks is essential.



Smoothing is thus used in this context to not only diminish small-scale noise, but, primarily, to enable measurement of strong lines.

Though many smoothing algorithms may be applied, such as the use of fourier transform optimum restoration (Brault & White 1971), the method chosen was gaussian-weighted smoothing. Though simpler, this method was judged to outweigh fourier smoothing, since in order to remove such comparatively large noise, the cutoff frequency would need to lie within the main fourier transform, and not at the higher cut-off frequency described by Brault & White. As such, the spectra may be considerably distorted on re-transformation into

λ -space.

In choosing a gaussian weighted algorithm, the primary line profile remains as invariant as possible. In addition, accurate removal of the secondary peaks will require a wide smoothing window, so that features small in comparison to the window width will be smoothed most effectively. This criterion may be met by matching the smoothing window-width with the mean spectral-line width, allowing the primary line profile to be least affected, while removing the secondary lines.

Letting $f(\lambda_i)$ be the intensity value at a given wavelength λ in the unsmoothed spectra, and $F(\lambda_i)$ the gaussian smoothed value, then the smoothing is completed by use of eq (1.65) below,

$$F(\lambda_i) = \frac{\sum_{i=-n^*}^{n^*} f(\lambda_i) \exp \left\{ -\frac{2i^2}{n^*} \right\}}{\sum_{i=-n^*}^{n^*} \exp \left\{ -\frac{2i^2}{n^*} \right\}} \quad (1.65)$$

where $-n^*$ to n^* define the n data points within the smoothing window. Within the window, each wavelength position is weighted by the corresponding value of a gaussian of unity depth, centred at λ_i , and half width equal to the smoothing window.

Since the mean width of lines blended in this way is $0.5A^0$ and the wavelength increment of the discrete data is $0.042A^0$, a gaussian smoothing window of 9-11 data points is suggested. Increasing the window width further than this limit will prove counterproductive since the primary gaussian profile will begin to deform due to dilution caused from adjacent spectral lines.

The effects of gaussian-11 point smoothing are illustrated in figure (XXI-abcd).

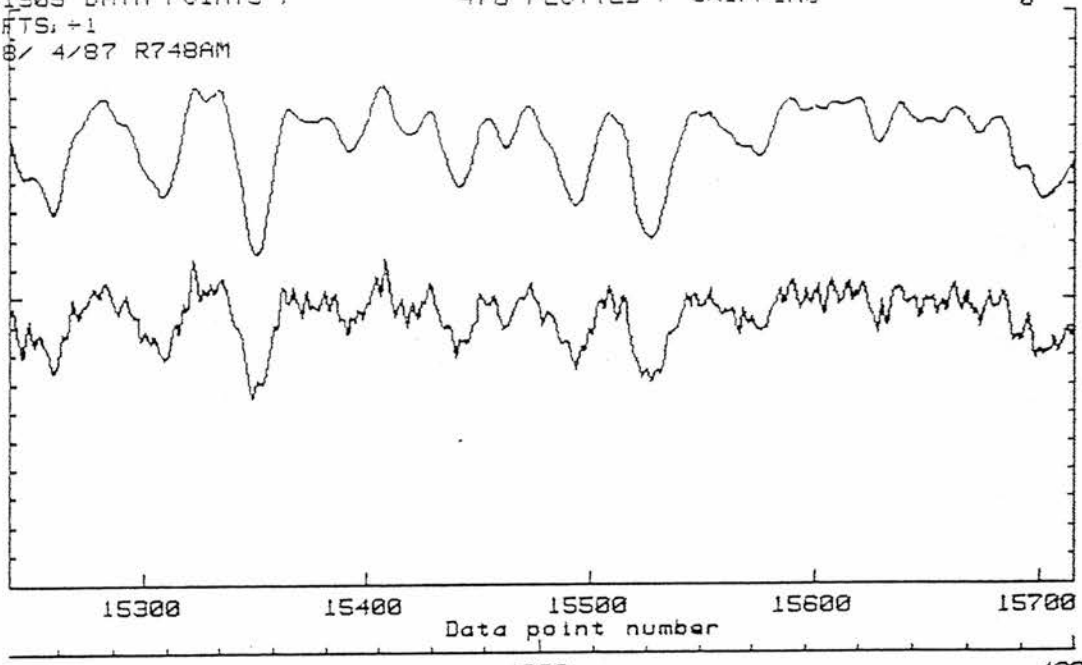
Though cross-correlation is now possible, it is expected that in choosing a wide window, blending may occur with closely adjacent spectral lines. The

21905 DATA POINTS ,
R748AM. FTS, +1
11:20 8/ 4/87 R748AM

476 PLOTTED , SKIPPING

0

0
1
0

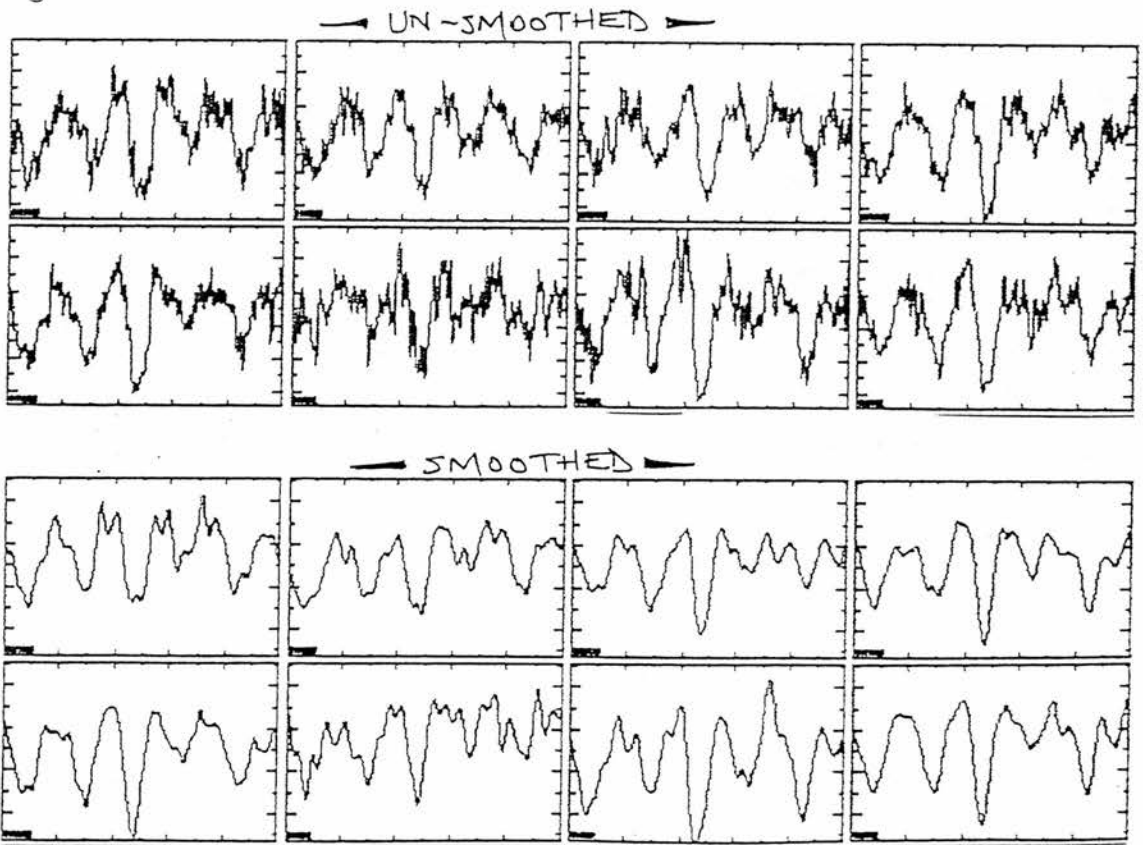


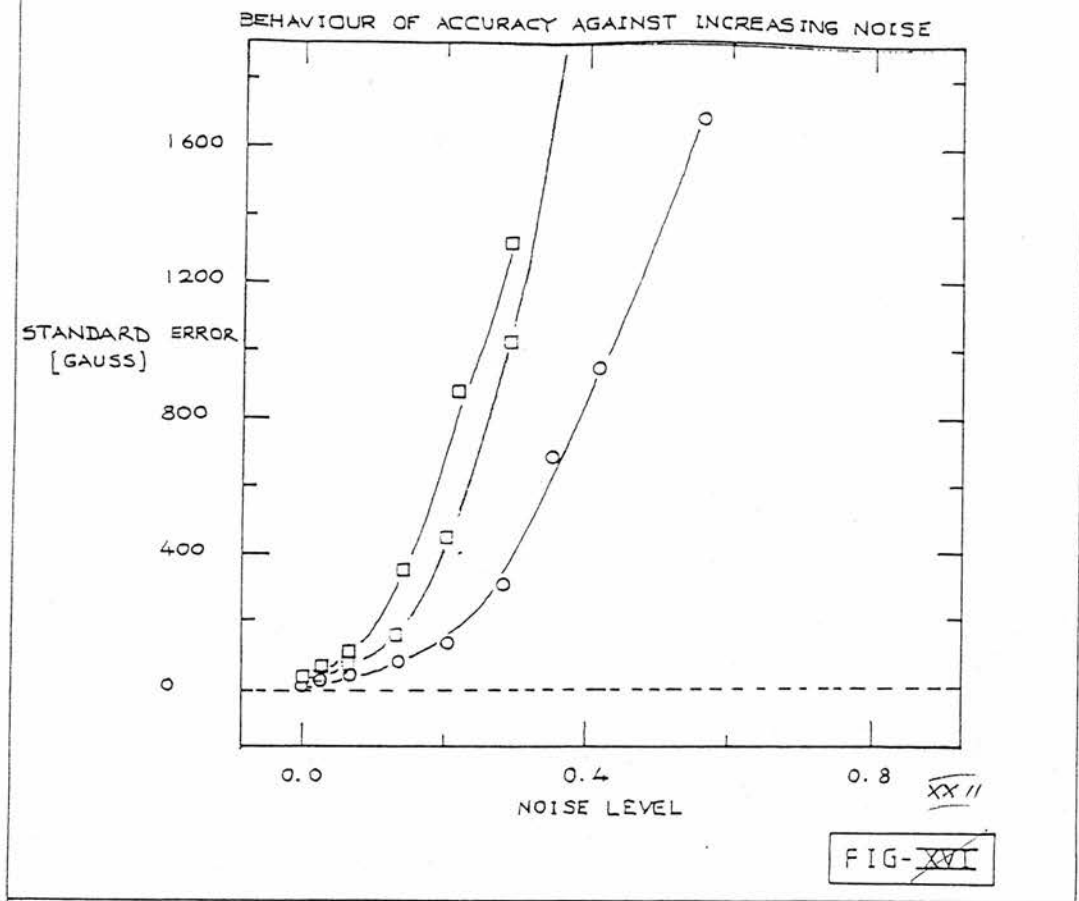
4250
Wavelength-Angstrom

Fig-XXI a

4270

errors incurred by this blending may yet invalidate the procedure, by destroying magnetic shift.





I.10.2 Results of Smoothing

To test to what extent blending destroys the magnetic field measurement, synthetic lines, created as previously mentioned, were subjected to the smoothing procedure and subsequently studied. By cross-correlating a smoothed spectrum with the original the discrepancy created by the smoothing may be evaluated. No systematic shift in either direction is detected from such experiments, although, as noise is increased, individual measurements do diverge from zero. The errors incurred within a large set are plotted against noise as before in fig (XXII).

It is found that the smoothing algorithm decreases the attainable accuracy considerably, resulting in, at medium noise levels, errors in excess of 100%, and providing inferior accuracy to either of the template or classical measurement systems.

On investigating the distribution of individual magnetic field measure-

ments, this decrease in accuracy is found to result from a small proportion of values, greatly divergent from the bulk of the set. These results may be identified with the blending caused by closely-adjacent lines incorporated into the primary line profile by the smoothing. The accuracy obtainable for the discussed noise level of 30% could then be as poor as ± 1000 gauss (50%), unless a method for the elimination of such spurious measurements is achieved.

In order to remove objectively any divergent field measurements from a given data set, it is necessary to devise an automated method for estimating the parameters of the parent distribution from a regular sample of data values devoid of erroneous measurements.

The central limit theorem states that if $x_1, x_2, x_3 \dots, x_n$ are independent random variables having the same distribution, with mean μ and variance σ^2 , then as $n \rightarrow \infty$, the limiting distribution of the random variable \bar{X} is the standard normal distribution with mean μ and variance $\frac{\sigma^2}{n}$. Although the result is true for any parent population with a first and second moment, it is often assumed that a set of measurements is like a random sample from a normal distribution for which the probability density is given by

$$f_x(x) = \frac{1}{\sigma\sqrt{2\pi}} \exp \left\{ -\frac{1}{2} \left(\frac{x - \mu}{\sigma} \right)^2 \right\} \quad (1.65)$$

and then to test the individual values for possible membership of this parent population, using unbiased estimates of the population mean μ and variance σ^2 . Alternatively, the central limit theorem may be used iteratively in the following manner:

Let the observed data set consist of n unsorted results, including possibly erroneous values. The inequality (1.66) states that an obtained mean value \bar{x} may be considered to have originated from a parent population with mean μ

and variance σ^2 if

$$\frac{\bar{x} - \mu}{\left(\frac{\sigma}{\sqrt{n}}\right)} < Z \quad (1.66)$$

where Z is dependent upon a confidence limit based on the requirement that the exclusion of an individual measurement should only change the mean \bar{x} by less than $\frac{Z\sigma}{\sqrt{n}}$.

Initially, let \bar{x} be evaluated from the n data values, with μ and σ^2 from the data set of $n - 1$ values obtained by omitting the first. If the inequality (1.66) is satisfied, then the omitted data point is accepted as a member of the original data set, and the next member is similarly tested. If the inequality (1.66) is not satisfied, the exclusion of the first data point has significantly altered the mean of the set, and may therefore be discarded. A new mean \bar{x} is then created from the remaining data points and new estimates of μ and σ^2 made as before, followed by a test against the inequality (1.66) with the current value of n . This process is repeated until all of the data points have been tested. In this manner, a value of \bar{x} may be formed from the original data set from which the rogue values have been removed.

Since the process is iterative, it is conceivable that, when automated, it could discard all of the data. To avoid this, the high confidence limit of $Z = 4$ was taken. However, since the process involves discarding a confirmed rogue candidate and then recalculating estimates of μ and σ^2 , with a consequent reduction in the variance, the high initial stringency is thereby somewhat relaxed.

This procedure then allows for the rejection of rogue values in an automated fashion. By comparison with preliminary procedure of Bonsack for the rejection of lines in establishing a satisfactory line list for classical measurement, only a small number of additional lines are eliminated in the cross-correlation process by applying the above procedure. The data points discarded are found

to be extreme values, which, by visual inspection would have been rejected out of hand, but in the automated method they must be statistically identified and systematically rejected by means of an objective criterion.

I.11.1 Conclusions

As a result of the conducted testing procedure, it is apparent that it is feasible to apply cross-correlation to the measurement of stellar magnetic variability. It is also suggested that the following procedure will minimize errors in the measurement procedure.

Preliminary Analysis

Straight cross-correlation of large spectral ranges may be conducted to indicate the existence of global magnetic field variability. The measured shift may then be calibrated, as indicated in Section (I.9.4.3), to give the global magnetic field. The advantage of this technique is that it may be completed within a short time scale, frequently one hour, resulting in a first approximation to the results.

Further Analysis

A more detailed analysis may then be conducted using either of the two individual line-measurement systems. Consideration of plate noise as given in sect (I.8.3) will then enable a clear choice between the two to be made. Smoothing must then be performed to remove secondary lines and to enable measurement. Once this has been completed, individual lines may be measured, and magnetic field variations for each element attained. Greatly divergent measurements may be removed subject to failing the statistical group test, resulting in a clean sample from which the measured field and probable error may be derived.

It is envisaged that the entire process, from line identification to magnetic field attainment may be easily conducted within a few days, with accuracy comparable, if not better, than the classical comparator methods of such as Pilachowski (1974).

II.1.0 Analysis applied to HD49976

II.1.1 The A0p star HD49976

The feasibility of applying ZCROSS to the problem of magnetic-field measurement of synthetic data has been extensively investigated. Such an application is found to be feasible, and may reproduce accuracy better than the traditional measurement system. ZCROSS is now applied to HD49976, an Sr-Cr A0p star with particularly strong Sr-II variation, as a final test of the measurement system proposed.

Babcock mentions HD49976 in his catalogue of magnetic stars (1958), where he acquires only one measurement of the magnetic field, though many of his plates exhibit evidence of a medium strength field. Since many of the spectral lines are broad and shallow, Babcock was unable to attain more information than to state the existence of a polarity change in the observed magnetic field and possible non-uniform variation in amplitude.

Van de Heuvel (1970) encountered similar problems, and though attaining a value of 1496 ± 618 gauss on one plate, was unable to acquire further information, and concluded that the star may be magnetic.

The first extensive investigation was completed by Pilachowski et al (1974). Nineteen spectrograms obtained at the coudé focus of the 2.24 m telescope on Mauna Kea, were taken at $6.8\text{mm}^{-1}A^0$ on baked Kodak IIa0 plates. Their analysis indicated the existence of a double-wave magnetic variation with period of 2.976 days, consistent with spectroscopic and photometric observations.

Through the good offices of Professor Stibbs and the generosity of Dr. Bonsack fifteen of the spectrograms were kindly made available by the Institute for Astronomy of the University of Hawaii for re-analysis in St. Andrews by ZCROSS, although two spectrograms were subsequently found to be unsuitable. Consequently, the data set used in this re-analysis, is based upon 13

spectrograms, and by comparison with the results of Pilachowski an estimate upon the accuracy of ZCROSS may be attained.

II.2.1 Reduction

The spectrograms were kindly digitized at the Dominion Astrophysical Observatory (DAO) by Dr. Graham Hill with the PDS microdensitometer, and associated software (Hill 1986, previously Fisher 1983). By use of this software, accuracy comparable to that obtained upon the Abbe comparators is attained while allowing speeds of $12\text{mm}\cdot\text{sec}^{-1}$ to be obtained. Scanning is performed by a number of 'cuts' (a single line of the scan) dependent upon the type of spectra measured: Clear-plate scans are created by one cut along along the spectrum, and one outside of the arcs, parallel to the first; Arcs by one cut along each arc, the results being combined into a single file; Stellar spectra scans by multiple cuts dependent upon the width of the spectra. Once all spectra have been scanned, with respect to a known wavelength, all data are stored in FITS format (Wells 1981), for the compactness and flexibility that this format provides. All subsequent processing is conducted using this format, specifically the data reduction programs REDUCE (Hill et al 1982), and ZCROSS.

Conversion of the PDS data array, density against position in microns, to a wavelength linearized spectrum is attained with resort to the arc files appropriate to each plate. The position of a number of arc lines are evaluated by means of user-defined parabolic line-profile fitting. Once a small sample of the 100 arc lines have been measured by this process, REDUCE will then run through the remainder automatically. The difference between the arc placements and a predicted standard plate is then calculated, creating a 'correction curve' which may be fitted by a fifth or sixth order polynomial. The coefficients are then used to convert the stellar scale in microns, to that of wavelength.

The clear plate is subsequently subtracted from the stellar spectra, and density to intensity calibration attained, by use of the calibration wedge. Each

resulting spectrum now approximates the real stellar intensity as opposed to photographic plate density. In order to remove the superimposed black-body profile, rectification is performed by the placement of 25 points along the spectra. Fitting of a polynomial to these points defines unit intensity as a function of wavelength, from which the real intensity is scaled to create a rectified-to-unity intensity scale across the plate. From this format, all further processing, including the ZCROSS application, is conducted.

II.3.1 Measurement strategy

Testing of the measurement procedure indicated that an invaluable precursor to detailed measurement is application of the Weiss sectional cross-correlation method. In this manner, global magnetic field data may be obtained, providing a quantitative variation against which further detailed analysis may be compared.

The method may be applied in two successive applications. Straight cross-correlation of sections, resulting in a wavelength shift, may be used to determine the magnetic variation, though absolute values of the field strength are not obtained. An extension of this requires the identification of spectral lines within the sections involved, and evaluation of the weighted mean value of $Z\lambda^2$.

II.3.2 Weiss sectional cross-correlation

The choice of spectral sections and appropriate sectional windows may be made with resort to the following considerations. Though evaluation of the magnetic field from the mutual shift is independent of wavelength to the extent that the variation is eliminated by calculation of the weighted mean of the free parameters, choice of a very wide section, $> 100A^0$, will broaden the cross-correlation peak. This broadening will subsequently introduce inaccuracy in the peak position, on account of the parabolic fitting procedure. Thus, although increased accuracy is gained by the inclusion of many spectral lines, this accuracy is bounded, if to attain a greater accuracy a wide spectral range is adopted.

Similarly, though the weighed mean value of $Z\lambda^2$ incorporates variations in line depth, it has been assumed that the width of all lines be invariant. Large-line width variations within the adopted section will invalidate the elimination of the width parameter in Eq. (1.60), requiring a modified weighting of the form of $D_0^2\sigma$.

It is thus expedient in the choice of appropriate sections to choose windows of $50 - 100A^0$ width within which lie a large number of discernible lines, and that exclude broad features: In application to HD49976 and to Ap stars in general, the hydrogen lines and the very variable lines CaII 3933A⁰, and SrII 4215A⁰. Variation in line strength will obviously decrease the accuracy of the weighting, since the variability in depth will increase and decrease the weighting contributed by the line. Ca II must also be eliminated due to extensive wings apparent between phase 0.10 - 0.30, which will bias the measurement and depress the depth component of adjacent lines.

II.3.3 Measurement and Calibration

The wavelength sections defined in this analysis are 4000 - 4050A⁰, 4170 - 4200A⁰, and 4390 - 4410A⁰. For the purpose of sectional analysis, ZCROSS, the speciality of which is individual line measurements, is replaced by the parent program VCROSS, standard to radial velocity sectional measurements. On application of VCROSS, the mutual shift between O and E spectra is obtained and calibration of the shift measurement is then completed through calculation of the D_0^2 weighted mean $Z\lambda^2$.

Table (V) shows the prominent lines of central depth greater than 0.1 in depth below the continuum. Lines of lesser depth may be ignored since the weighting they receive (1/200) will be considerably smaller than the weighting of the average lines. Z-values may be obtained from the multiplet number, assuming pure LS coupling as discussed earlier, for unmeasured lines. Calculation of the weighted mean reveals,

$$\langle Z\lambda^2 \rangle_{D_0^2} = 2.148 \times 10^7 \quad (2.1)$$

---Table (V)---

λ_0	Element	D	Z	λ_0	Element	D	Z
4003.764	Fe-I	0.3	1.25	4045.815	Fe-I	0.5	1.25
4005.246	Fe-I	0.5	1.50	4049.140	Cr-II	0.4	0.97
4007.277	Fe-I	0.3	0.89	4170.906	Fe-II	0.45	1.50
4009.714	Fe-I	0.1	1.48	4173.450	Fe-II	0.4	1.49
4012.467	Fe-II	0.5	0.40	4179.430	Cr-II	0.55	1.21
4014.899	Ce-II	0.15	1.66	4181.758	Fe-I	0.35	1.50
4017.156	Fe-I	0.2	1.49	4184.895	Fe-I	0.3	1.47
4017.960	Cr-II	0.35	1.80	4187.802	Fe-I	0.25	1.47
4020.898	Co-I	0.1	1.33	4190.724	Si-II	0.15	1.10
4021.869	Fe-I	0.1	1.07	4191.436	Fe-I	0.35	1.50
4022.360	Fe-I	0.35	1.03	4195.410	Cr-II	0.35	1.40
4025.136	Ti-II	0.45	1.06	4198.310	Fe-I	0.55	1.50
4028.332	Ti-II	0.25	1.06	4390.585	Mg-II	0.25	1.08
4030.499	Fe-I	0.6	0.80	4391.753	Cr-I	0.2	2.00
4033.073	Mn-I	0.4	1.40	4394.057	Ti-II	0.15	1.34
4034.490	Mn-I	0.15	1.70	4395.031	Ti-II	0.25	1.07
4035.631	V-II	0.15	0.75	4395.848	Ti-II	0.2	1.21
4038.030	Cr-II	0.2	1.05	4398.020	Y-II	0.05	1.00
4039.100	Cr-I	0.2	1.14	4400.355	Sc-II	0.2	1.08
4041.361	Mn-I	0.1	1.56	4404.752	Fe-I	0.25	1.13
4044.614	Fe-I	0.25	1.30	4407.714	Fe-I	0.1	1.83

Application of this value into the standard zeeman separation formula,

$$H = \frac{\Delta\lambda}{4.67 \times 10^{-13} \times \left(\frac{\langle Z\lambda^2 \rangle}{2}\right)} \quad (2.2)$$

gives $H = 49280 \Delta\lambda$

This supplies the calibration constant of

$$0.01 A^0 = 498 \text{ gauss} \quad (2.3)$$

enabling the scaling of the mutual shift to magnetic field as shown in fig (XXIII).

The results obtained compare favourably to the values obtained by Pila-chowski, as seen in fig (XXIV). Section (I.5.4.3) showed that errors arising from the weighting of D_0^2 amount to only 1.7%, and thus errors in these results arise totally from the dispersion of individual-magnetic field measurements and from line variability.

VCROSS may be used to assign errors to the measured fields, since errors based upon the precision of the parabolic fitting are produced by the system. These errors may be used as an approximate guide, though are found to be invariably smaller than expected. It is found from the analysis of predetermined errors in the testing of VCROSS (Hill 1983) that the real errors may be 2-4 times the value output from VCROSS. The error bars in fig (XXIII) are calculated in this manner, with recourse to the intermediate value of three times the parabolic goodness-of-fit. It is stressed that the errors are highly subjective, although the relative errors between measurements may be considered as correct. Exact errors could only be attained by a considerable detailed analysis, of the internal errors of VCROSS. As this technique is only to be regarded as a preliminary system of measurement, such an analysis is considered to be inappropriate.

GLOBAL MAGNETIC FIELD VARIATIONS FOR WEISS SYST

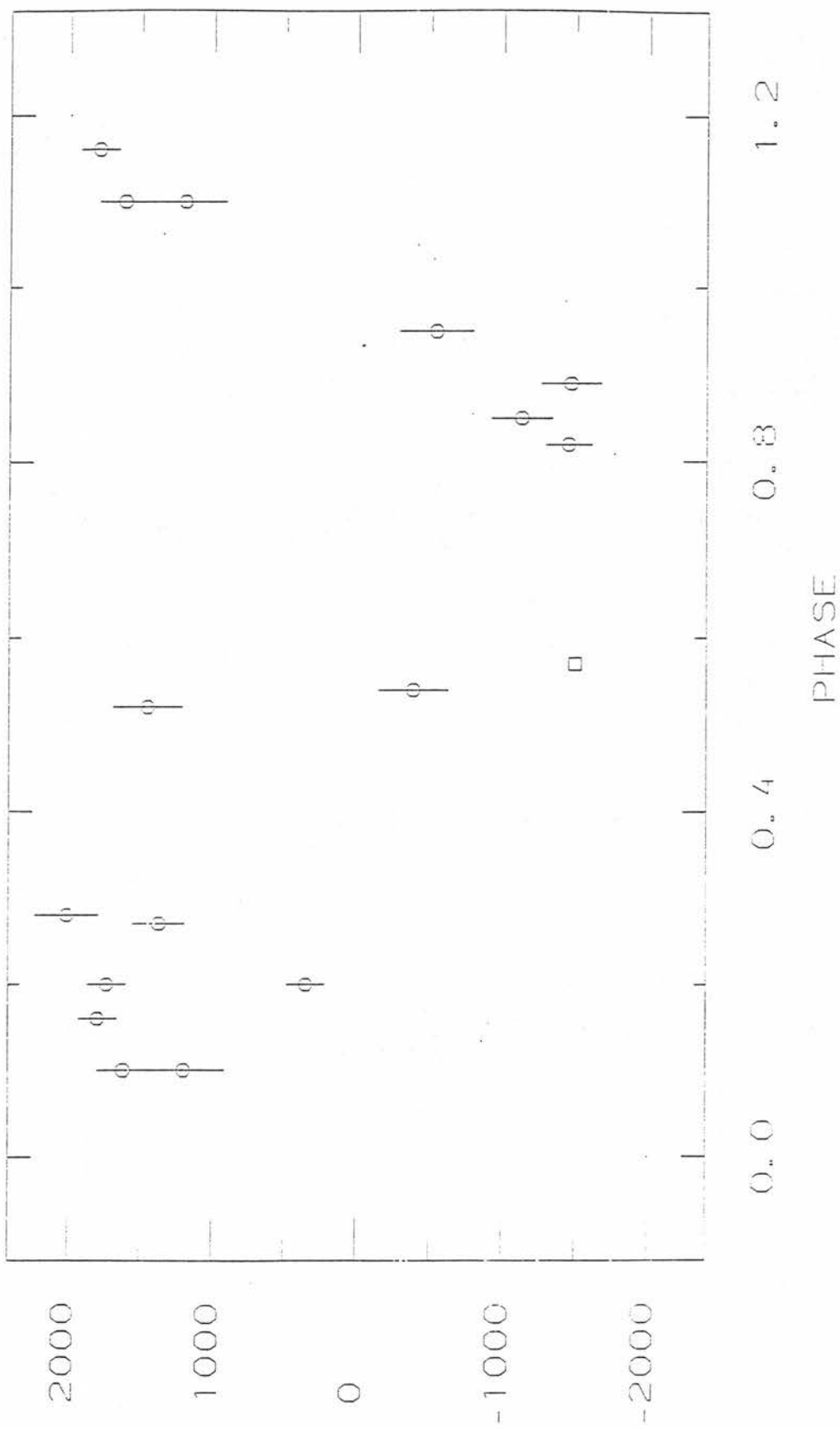
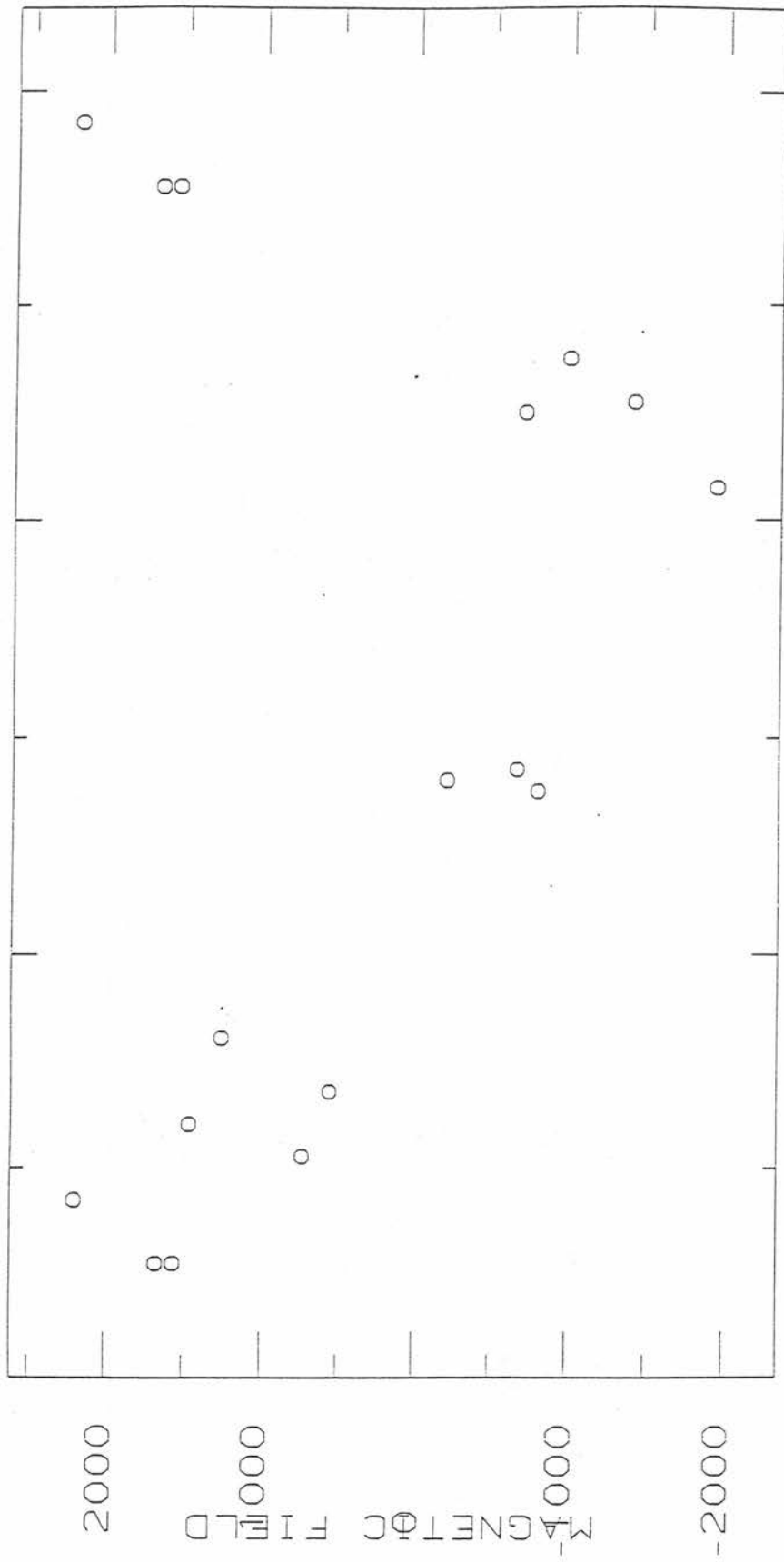


Fig- XXIII

BONASCK MEASUREMENTS PHASED TO 2D. 9754



PHASE

Fig-XXIV

An immediate comparison of speed reveals the importance of even this preliminary analysis. The entire measurement process, from control-file delimitation, through measurement of line strengths and mutual shift, was completed within two hours. In comparison, the non elemental segregated results of Pilachowski are estimated to have been the result of a month's work. This enhancement in speed, considered with the accuracy attained, vindicates the use of cross-correlation, even at this preliminary stage.

II.4.0 Individual line analysis

II.4.1 Definition of noise level

Central to the choice of method for further analysis is the noise level incident upon the spectra. In order to evaluate this parameter, consideration must be given to the lines to be used prior to proceeding. To facilitate identification of spectral lines, all 13 unsmoothed spectrograms were co-added. Noise is hereby eliminated, producing a composite spectrum depicting clearly the individual lines.

The spectra of HD49976 is found to be composed principally of Iron lines. Iron I is predominant, although many lines of Chromium, and a few Titanium are well aspected. Elements other than these do not show sufficient lines with which to apply effectively the measurement process since, at most, only 3 to 4 lines for the rare earth elements are attained. Subsequently, further analysis will be confined to Iron, Chromium, and Titanium.

Individual lines were admitted to the line list for magnetic field measurement on fulfilling the following criteria:

- (i) Lines to be visibly unblended by adjacent features
- (ii) No other line in the line list may be within $0.5A^0$ of the rest-wavelength position.

The second criterion was adopted since HD49976 is a spectrum variable. It is conceivable that since identification is based upon a co-added spectra, a variable line, strong over a short part of the cycle, may not produce a visible profile in the vicinity of stronger lines. This blending would distort measurement and is thus to be avoided if at all possible.

A total of 122 lines were identified by this method, resulting in the line list given in Appendix-A. Also given in the appendix are the identified lines of

minor elements, although the sparseness of these lines precludes measurement. Evaluation of the noise level may now be conducted. From the line list, the average depth is found to be 0.27 ± 0.13 . Since the random fluctuations described in Section (I.4.3) have a mean depth of 0.07, the noise level may be defined as 0.25 ± 0.16 . Since this result does not include the variable effects of blending, it is expected that the noise level is marginally higher than stated. With reference to fig (XVI), either measurement method is suggested as appropriate at this level, with errors of $\pm 15\%$, and consequently, both methods will be applied.

II.4.2. Window definition

As highlighted in Section (I.9.2.1), the definition of the cross-correlation window is of critical importance. A wide window may mask the primary cross-correlation peak by adjacent 'noise', though too narrow a definition eliminates valuable data in the line wings. Radial velocity variations over the cycle also provide an additional consideration. Unless windows are defined for each spectra, the window width must allow for radial velocity variations of both O & E spectra on all plates.

The co-added spectrum provides the simplest means of definition, since by its construction it incorporates all variations in rest wavelength. No supposition regarding the radial velocity variations is required, and adjacent line blendings may be eliminated. The mutual shift between O & E spectra is also included within the spectra, allowing window determination to incorporate the complete line in both polarized spectra.

For each line under consideration an individual window was defined from the accumulated spectra. Measurements were taken so as to maximize the window width without inclusion of adjacent features. These windows are also shown in Appendix-A. Though these windows are large in comparison to a single line on a given plate, the accuracy lost due to small scale noise inclusion

is expected to be minimal compared to the possible error caused by radial-velocity variations carrying the line wings outside of the window.

II.4.3 Additional template considerations.

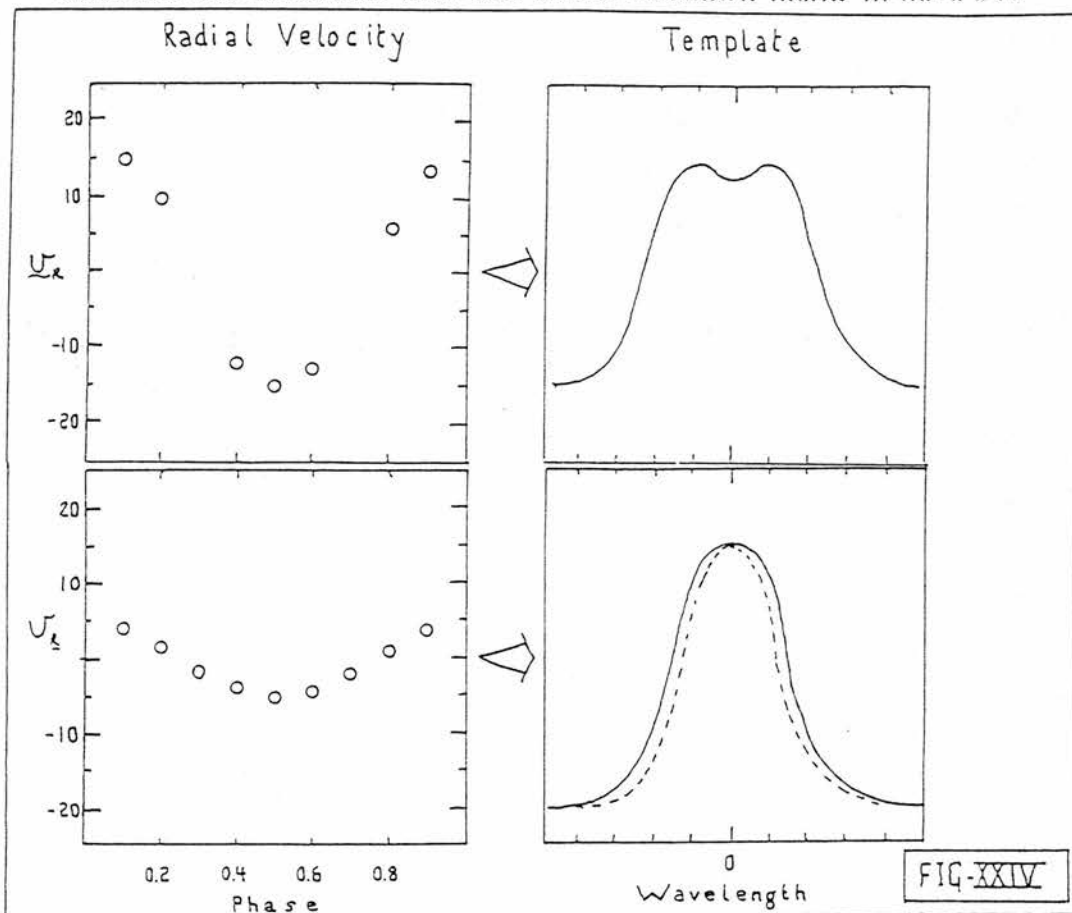
In designing a template to cross-correlate with O/E spectra, it is important to mimic the line parameters as accurately as possible. Deviation will reduce contrast in the cross-correlation function as discussed in Section (I.4.2). Additionally, the template must be constructed suitably close to the studied lines in order to minimize the window width. It is unsuitable to create a synthetic line at rest wavelength with which to cross-correlate with both O & E spectra, since the stellar systematic velocity of 19.5 km.s^{-1} would require an additional window width of $0.3A^0$. It is consequently expedient to place the template as close to the studied lines as possible.

Since the line strengths of the various elements are expected to vary over phase, a known extreme example being Strontium-II, for maximum accuracy in replication, the mean line strength parameters must be used. Any variation in line profile would thus still resemble the template, whereas a template defined from the maximum profile strength may be unusable at the opposite extremum.

The accumulated spectrum may be used to furnish the requisite parameters, but more importantly, may itself be used as a template. The sum of the 13 spectrograms is essentially noise free, exhibits mean parameters for the line profiles, with lines centred at heliocentric velocity-corrected positions. Only the velocity variations over a cycle deform the co-added spectrum, creating a broader template than the studied line. Since the intensity of the cross-correlation peak is dependent upon the smaller of the line widths (eq. (1.61)), this broadening is expected to introduce minimal inaccuracy in this case because the velocity variations are small.

The creation of a template by co-addition in a high velocity-variation spectrum is expected to be inaccurate. High velocity variations creating a significant shift in the rest-wavelength, compared to the line width would severely deform the template.

Consider measurements over one period as shown below in fig XXIV



The incomplete phase coverage, and high velocity shift to line width ratio, conspire to skew, and double the template line. The subsequent use of this line as a template, quite apart from the resultant deformed fourier transform, will produce multiple errors in the cross-correlation function.

Pilachowski et al. report Iron and Chromium radial velocity variations of amplitude $\pm 6 \text{ km.s}^{-1}$. This is sufficiently small in comparison to the broad line widths encountered in HD49976 to allow a template to be derived in this manner.

II.4.4 Measurement of magnetic field and radial velocities

Once windows have been delineated, the magnetic field measurements are acquired by running ZCROSS once for each element under consideration. The position of individual cross-correlation peaks are measured by automatic parabolic curve fitting to the top 15% of the peak.

The O/E cross-correlation was performed once for O/E, though measurement of the radial velocities, required a second run with a template spectrum situated at rest wavelength against either O or E for absolute measurements. Radial velocity variations may subsequently be obtained by computing the mean O/E shift, and adding the shift determined from Template / O spectra cross-correlation.

In contrast, the template measurement requires one run of O/E vs Template, and one additional cross-correlation, of rest wavelength template versus co-added spectra. One elemental segregated run by either method may be completed in 2 hours at most, for typical line list numbers of 20 lines, on each of the 13 spectrograms.

II.5.1 Data Analysis

The resultant shift measurements supplied by ZCROSS, now require reduction to maximize recovery of pertinent data. It is expected that two main errors exist within the attained measurements.

- (i) Errors due to invisible blending of the lines studied.
- (ii) Errors arising from the failure to cross-correlate satisfactorily. Due to inaccurate window-fitting, rogue line profiles, or other such random occurrences, may cause a cross-correlation peak to be unobtainable.

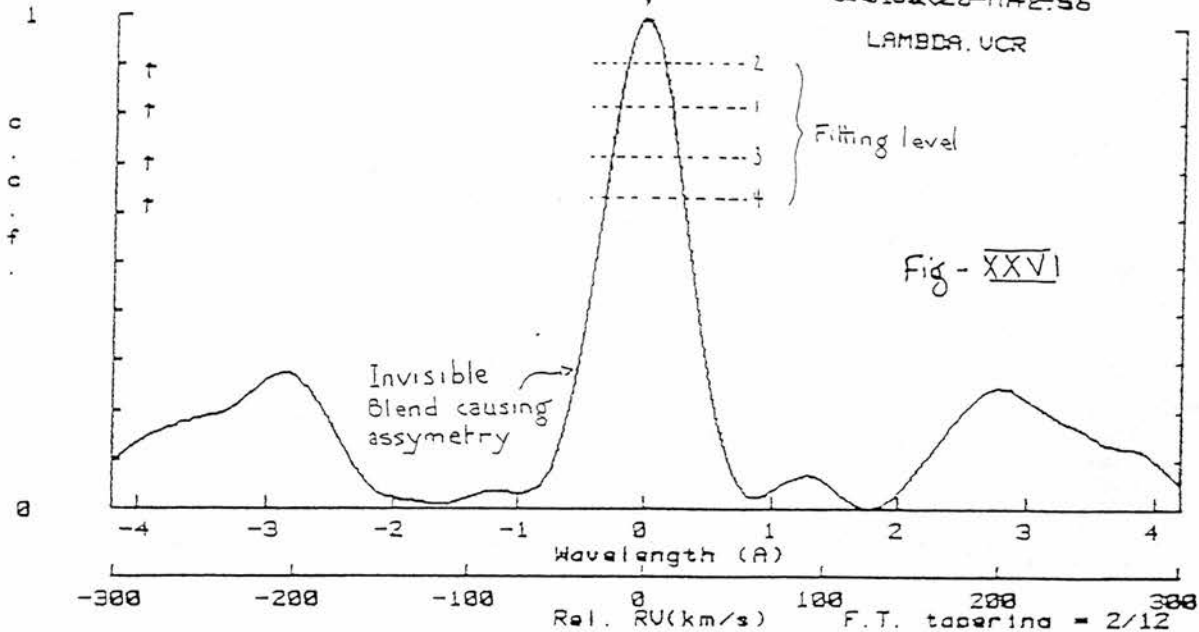
II.5.1.1 Line blending errors

Methods for the elimination of the most frequently encountered error were the subject of much analysis. A line, invisibly blended, will on cross-correlation produce an erroneous cross-correlation peak measurement. However, it may be possible to attach qualitative errors to measurements from analysis of the resultant cross-correlation peak profile.

A symmetric line, blended on one side, cross-correlated with a second symmetric line will produce an asymmetric cross-correlation peak. It was proposed that this asymmetry may be evaluated by fitting a parabola at two levels such as 85% and 65% of the peak height. The resultant shift between measurements would imply asymmetry as indicated in figure (XXVI).

In practice, this method proves insensitive, since small asymmetries exist in most cross-correlation profiles, and the smoothing tends to diminish small asymmetries, regardless of blending. The required level of discrimination between valid and erroneous results was found to be unrealizable and the method discarded.

Level	Program *	RZ41AS	KE741A	HD49976	-4.78	4202			
	Comp *	R741AM	KE741A	HD49976	-4.78	4202	RU	0.00	k/s
1	D(0	0	0	0	0	0	0	0
2	D(0	0	0	0	0	0	0	0
3	D(0	0	0	0	0	0	0	0
4	D(0	0	0	0	0	0	0	0



If blending is caused by the existence of hitherto unobserved secondary lines, then since the blending secondary line, unless variable, will result in blending on all plates, a spectral line that produces consistently erroneous results may be considered for elimination.

This criterion, used by Pilachowski et al. in their zeeman-shift reductions, may be formulated according to Bonsack (1987) in the following way. The magnetic field may be evaluated from the zeeman shift by means of the formula,

$$\gamma = ZH_i \tag{2.4}$$

where

$$\gamma = \frac{\Delta\lambda}{\Lambda^2} \tag{2.5}$$

and Λ incorporates the proportionality constant, since $\Delta\lambda$ is measured in Angstroms,

$$\Lambda = \frac{\lambda}{1.033 \times 10^6} \tag{2.6}$$

The final value of the magnetic field, $\langle H_z \rangle$ may be acquired by least squares fitting to the displacements weighted by Z ,

$$\langle H_z \rangle = \frac{\sum \gamma_i Z_i}{\sum (Z_i)^2} \quad (2.7)$$

The estimated variance of $\langle H_z \rangle$ may be calculated as

$$S_H^2 = \frac{\sum \gamma_i^2 - \langle H \rangle \sum \gamma_i Z_i}{(n-1) \sum Z_i^2}$$

where n is the number of lines under consideration. Individual measurements of line magnetic field H_z , may be obtained from Eq. (1.48) and the index D_H formed where

$$D_H(i) = \frac{|H_i - \langle H \rangle|}{n^{1/2} S_H} \quad (2.8)$$

If a given spectral line exhibits considerably anomalous values of the index D_H on a significant proportion of the plates, the line may be eliminated from all plates, on the hypothesis that blending with an invisible secondary line is the root cause of the error. Bonsack suggests that elimination be conducted for $D_H > 5$, though, this value was found to be indiscriminately high. As such, lines were eliminated if, over phase, a line exhibited an average $D_H > 1$. This would compare to Bonsack if his definition of 'significant proportion' is regarded as one quarter.

II.5.1.2 Cross-correlation errors

Though the statistical method proposed by Bonsack will eliminate consistently blended lines, the occurrence of a single erroneous measurement will not be identified.

The effects of smoothing and its necessity were detailed in Section (I.10), where it was noted that smoothing may amplify blending from the few closely adjacent lines. A statistical method for the removal of these rogue results is also suggested. By application of this method, following elimination as suggested by Bonsack, the majority of errors are removed from the data set.

II.5.2 Magnetic field determinations

Figs (XXVII a-f) and (XXVIII a-f) illustrate the magnetic field derived by the O/E cross-correlation and the template measurement system respectively. The global magnetic field measures may be compared with the results of Pilachowski and the preliminary analysis by the Weiss sectional cross-correlation method. It is seen that all four sets show intrinsically similar variations, suggesting that large discrepancies are not incurred by application of any one method. In particular, there appears to be strong correlation between the results obtained by the Weiss method and that of the template application. Both show a pronounced depression of the field strength at phase 0.20, suggesting that this measurement is not an inaccuracy introduced by an individual method. This local depression is also apparent within measurements obtained classically by Pilachowski, though the spread of data at this phase results in a less obvious anomaly.

The least-defined variation appears to be the O versus E cross-correlation method, which exhibits a considerable spread of individual results at 0.80 and 0.20 phase, similar to those of Pilachowski et al.

A comparison of the errors evaluated from least-squares fitting of the shift measurement to magnetic field, shows that in many of the plates, errors of $\pm 250 - 300$ gauss are obtained in both cross-correlation systems, in accordance with the expected errors of the testing procedure. The slight decrease observed from that expected may be attributed to the smoothing process, which would produce a general lowering of the noise level, once blended lines are discarded.

The large errors incurred at phase 0.90 and around 0.50 are found to result from a very diverse data set at these two phases. Individual line magnetic fields obtained at these two phases show large internal disparity, which exaggerates the difficulties in discriminating between the true and erroneous results, by both Bonsack's rejection technique and the set sampling detailed in section I.10.2. Consequently, the data is largely unprocessed at these points.

The individual element magnetic fields with the exception of Titanium also reveal periodic variations similar to the global magnetic field measurements. The increased errors may be explained purely on statistical grounds, since the measurements are attained from a smaller sample.

It is also noteworthy that in each graph, the anomalously-low magnetic field measurement at phase 0.20 is present. In all the considered elements, the value given by this measurement remains invariant within errors at around 500 gauss. This all but eliminates the possibility that the value observed in the global field be the result of random bias. To eliminate the possibility of calibration errors on arc-measurement processing, both arcs were scrutinized to determine the existence of any bias in the polynomial fitting. A consistent residual difference from the correction curve would suggest that the spectra of either O or E had been shifted as a result of faulty measurement. No such bias was observed to exist, supplying credence to the 'reality' of this point. It was concluded that the observed magnetic field fluctuation is likely to be real as no

systematic processing error was found for its explanation.

The close correspondence between the results of both cross-correlation processes is further evidence of the relationship between noise level, and the incurred errors. As illustrated in section (I.9.3), the expected noise level predicts little preference between methods should exist. The similarity between the obtained results may be taken as corroborative evidence, though, due to the unique relationship at this 'noise level', does not verify the nature of either predicted error relation.

If any variation between methods is to be deduced, it is that the template measurement system provides more consistent measurements, showing an harmonic variation with few, if any third or higher terms. The verification of the first-order variation, the existence of which this method suggests, may only be attained with additional data at the incomplete phases.

Titanium shows the only distinctly-different variations. Results obtained show large errors and fluctuate unlike the other chemical elements. An explanation could be that as relatively few lines of Titanium were measured, accurate definition of a magnetic field by the least-squares procedure was not possible. However, results could also be explained by a large second-order variation creating magnetic positive maxima at 0.40 and 0.90 phase, with negative maxima at 0.15 and 0.65. Though a variation of this kind is not exhibited by other elements, a quadrupole field may provide an explanation coupled with an equatorial abundance anomaly of Titanium. However, considering the errors, incomplete phase coverage, and the basically dipolar field exhibited by the other elements, the titanium results are more likely to reflect a loss of accuracy because of the limited number of lines.

In concluding the discussion of these magnetic field results, it must be emphasised that HD49976 exhibits broad, shallow lines due to rotational broad-

ening. Consequently, though aimed at a global magnetic field, the difficulties inherent in the traditional, visual-measurement systems have precluded determination of the individual elemental magnetic variations. The accuracy of ZCROSS is thus demonstrated, when consideration is given to the low sample size for individual chemical element species, only 10 lines in some cases, and the relative consistency of the results as a function of phase.

II.5.3 Radial velocity variations

The use of a template in cross-correlation simplifies the measurement of the radial velocity variations. The mean of the shift from both O and E vs template may be calibrated by cross-correlating the template with a second template at rest wavelength. The radial velocity is thus a by-product of the measurement system, derived by

$$\Delta\lambda_v = \Delta\lambda_T + \left(\frac{\Delta\lambda_o + \Delta\lambda_e}{2} \right) \quad (2.9)$$

where

$\Delta\lambda_o$	= shift of O spectrum vs template
$\Delta\lambda_e$	= shift of E spectrum vs template
$\Delta\lambda_T$	= shift of template with rest wavelength template

The radial velocity variations for individual elements are depicted in figs (XXIX a-e).

Fitting of the harmonic-analysis equation

$$r_v = a_0 + a_1 \cos \theta + a_2 \cos 2\theta \quad (2.10)$$

as illustrated in the analysis of Mihalas (1970), reveals the stellar heliocentric radial velocity to be $18.54 km.s^{-1} \pm 0.39 km.s^{-1}$. Second-order terms are given in Table (VI).

Element	a0	a1	a2
Cr-I	18.47	+2.14	+7.40
Cr-II	17.55	+1.83	-3.33
Fe-I	19.13	+1.63	-2.58
Fe-II	17.78	+1.64	-2.63
Ti-II	19.82	-0.69	+3.35

— Table (VII) —

This result is in close agreement with the 19km.s^{-1} quoted by Pilachowski et al. Since a substantial part of the cycle is uncovered by data, great reliance upon the second order terms is perhaps unjustified. However, it is useful to show that the elements fall into one main category (Fe-I, Fe-II, Cr-II) and two possible alternative groups, Ti-II and Cr-II respectively.

II.6.1 Additional data: Equivalent width measurements

To complete the analysis of HD49976, the appropriate element equivalent-width variations were studied. Both Deutsch (1958) and Mihalas (1973) provide methods for harmonic analysis, requiring simultaneous measurements of radial velocity, equivalent width, and in Deutsch's method, the magnetic field. Since spectacular variation of Sr-II 4215.4⁰ and Ca-II 3933.4⁰ was noted by Pilachowski et al, an investigation of the equivalent width and radial velocity variations of both elements was also conducted.

REDUCE (Hill 1983) enables such an analysis to be conducted through the use of the VLINE routine. Following user definition of the continuum levels straddling the studied line, appropriate FWHM and central depth positions, VLINE fits a predetermined profile to the data. Though the user-defined parameters may be subject to small errors, the fitting routine CURFIT, by iteration, will converge on the proper values, eliminating the need for very accurate initial placements. VLINE then produces equivalent width variations, radial velocity, depth, FWHM, and possibly $v \sin(i)$ measurements.

To investigate the elemental variations, two strong unblended lines of each element were chosen. Measurements were performed upon both O and E spectra for the equivalent width, and the mean taken. A second-order Fourier series was subsequently fitted to both lines, to enable the mean of both variations to be evaluated, allowing subsequent scaling to be performed to create overall variations in equivalent width. The equivalent width variations are depicted in Fig (XXX a-g) and the Sr-II, Ca-II radial velocity variations in figs (XXXI a-b).

Though a primary peak is seen at phase 0.2, in most elements, the remainder of the cycle is insufficiently sampled to enable the resolution of a secondary peak observed by both Pilachowski, and Maitzen & Albrecht (1974). The tail

end of such a secondary peak is partly visible in the Cr-II variation, as are possible trends in Ti-II, Fe-II, and Cr-I. It is evident that any analysis primarily dependent upon accurate determination of the equivalent width variations would prove highly inaccurate as a result of the paucity of data between 0.3 - 0.8 in phase.

Only Fe-I is found to have a significantly different variation within the set. No such clear delineation of variation is seen, as in the remainder of the elements, and considering the individual scatter in measurements, there is no evidence for variation within this element.

In sharp contrast, Sr-II, and Ca-II exhibit large variations in equivalent width. The presence of a sharp primary maximum at phase 0.25 is evident in both, though no evidence for a secondary peak is found in the \mathcal{K} -line. Considering the rapid increase in equivalent width, it is conceivable that an unobserved peak similar to that of Sr-II occurs between 0.5 - 0.8 phase. The corresponding VLINE radial velocity variations are shown in figure (XXXI a-b) depicting, in the case of Sr-II, variations comparable to the elemental radial velocities obtained by ZCROSS, although with greater amplitude, and the mean radial velocity is considerably higher than the $18.54 \text{ km} \cdot \text{sec}^{-1}$ found earlier.

Calcium, however, behaves entirely differently. The radial velocity maximum is found to coincide with the equivalent width maximum, a variation that is incompatible solely with the motion of a surface spot region as concluded by Pilachowski et al.

II.6.2 Calcium 3933A⁰: The \mathcal{K} -line behaviour

For much of the cycle, the radial velocity of the \mathcal{K} -line is constant at approximately 16km.s^{-1} , save at magnetic maxima, where a sharp increase in the radial velocity is observed. To explain this variation then requires answers on two points: Firstly, the increase in equivalent width, caused by broadening of the \mathcal{K} -line profile; and secondly, the surface-wards velocity observed at magnetic maxima.

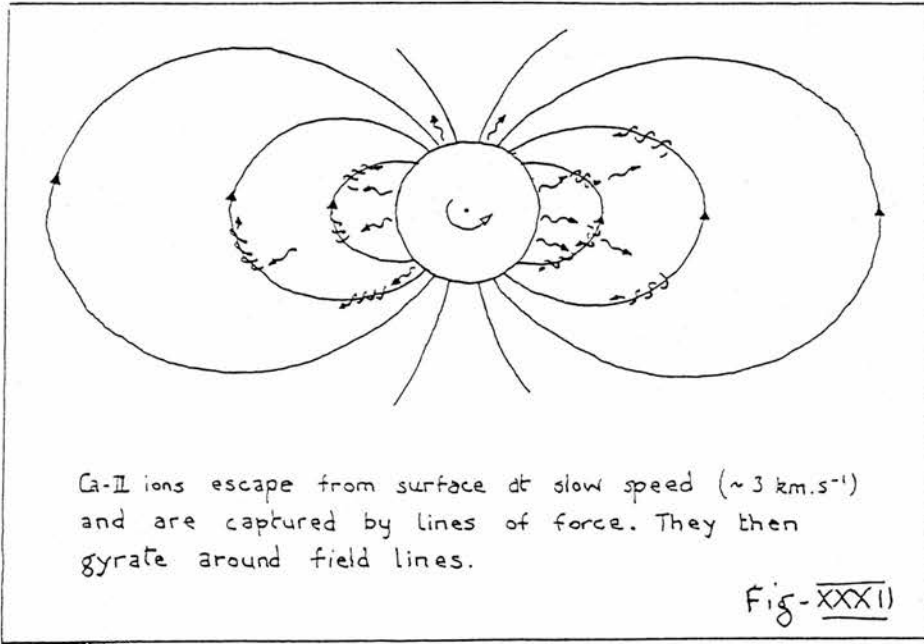
Thomas & Athay (1961) suggest that the broadening of the \mathcal{K} -line profile found in the solar chromosphere, and particularly spicules, may be caused by forced gyration of the ionized Ca-II around the field lines found in spicules. They also consider that the explanation of self-absorption, for the broad shallow lines, to be inadequate.

In a low-density plasma, a Ca-II ion would gyrate around the field lines in a field as small as 1 gauss. Though their discussion is limited to the solar chromosphere, it is useful to consider whether such effects could be the cause of the broadened \mathcal{K} -line in the Ap stars and HD49976.

The spicules seen in the solar chromosphere, are found to follow the field lines at the edges of the granulation cells. These cells and their product, the spicules are thus a product of the convective motions and the rising magnetic field. However, Ap stars are found to have a minimal convective envelope and so spicules will not occur in great numbers as seen in the solar chromosphere. However, the emergent field lines at the poles, assuming an oblique rotator model (Section III.1) will provide lines of force around which the Ca-II may gyrate.

It is thus feasible that the large global magnetic field, and not the microscopic sunspot fields be the source of the Ca-II gyration. Consider the following hypothetical model:

Assuming a slow outflux of Ca-II from the stellar surface, indicated by the overall lower radial velocity of 16 km.s^{-1} , into the surrounding low-density plasma, any Ca-II ions, will, upon meeting a line of magnetic force, gyrate around the line. Since in a low-density plasma the magnetic Reynolds number R_M is greater than unity, the Ca-II ion will be trapped to that flux loop. The Ca-II ion will then only be able to move along the lines of force, as seen in figure XXXII.



The angle between the magnetic and rotational axes, evaluated from derived r -values for the magnetic extrema (section III.3), indicates for HD49976 a value of $\beta = 90^\circ$. Taking a co-ordinate frame co-rotating with the stellar surface, since the field lines follow lines of stellar latitude, the Ca-II ions, in undergoing motion along the field lines are not constrained to co-rotate with the stellar surface, but may flow 'backwards' along the field lines until subjected to a retarding force. Such a force will appear as the Ca-II ions approach the magnetic poles.

As the magnetic lines of force approach the poles, the magnetic flux density increases, and through the properties of a magnetic mirror, the v_{\parallel} of the Ca-II

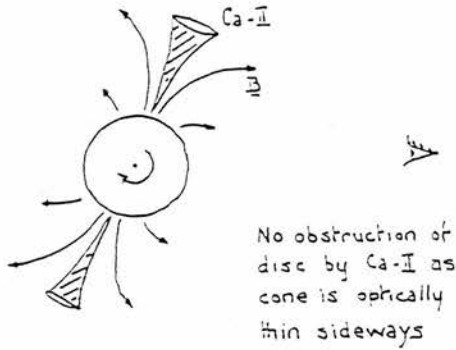
ions tends to zero. Since the field lines descend to the surface at the poles, the Ca-II ions will descend likewise, causing an increase in the radial velocity field, before being halted by the increased flux density and mirroring.

Ca-II ions, originally rising from the stellar chromosphere, will be channelled to the polar regions by the lines of force. Some Ca-II will, due to small pitch angle of gyration around the field lines, escape the mirror, and descend to the surface of the star at the poles, satisfying continuity of Ca-II ions. However the majority will not descend to the surface and will reverse direction. Due to the deceleration of the ions towards the poles, the trapped Ca-II ions will spend the majority of time in the vicinity of the poles while travelling along the field lines, though may even be confined to the poles by the balancing of the mirroring force, and the stellar rotational force.

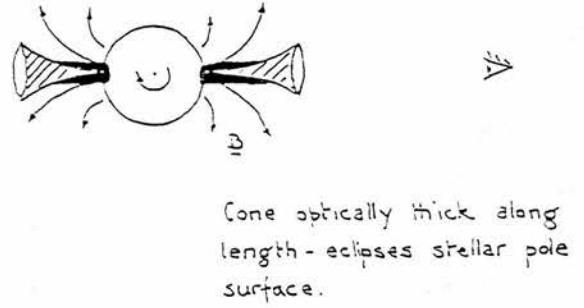
This hypothesis then leads to the picture of a concentration of Ca-II ions suspended, in either dynamical or static equilibrium, above the poles of the star causing an increased equivalent width to be measured. The geometry of this concentration would follow the magnetic field lines, leading to a conical geometry, as seen in figure (XXXIII). Observable features of such a concentration would be coincidence of magnetic field and equivalent width maxima, and an increase in the radial velocity variation at the poles. Additionally, if the Ca-II cone is optically thick lengthwise, obscuration of surface details on the star would occur. This would provide an explanation for the discrepant value at 0.20 phase in the magnetic field variations. At this phase, the angle between the cone axes of symmetry and the line of sight will be a minimum, causing maximum optical thickness. At other phases, since the cone is optically thinner in section than length, surface details are visible. Such variation is shown in figure (XXXIII).

Though this argument may appear to be highly speculative, the chan-

Concentration of Ca-II and illustration of possible surface eclipsing



Small Ca-II absorption profile.



Max Ca-II equivalent width.

Fig - XXXII

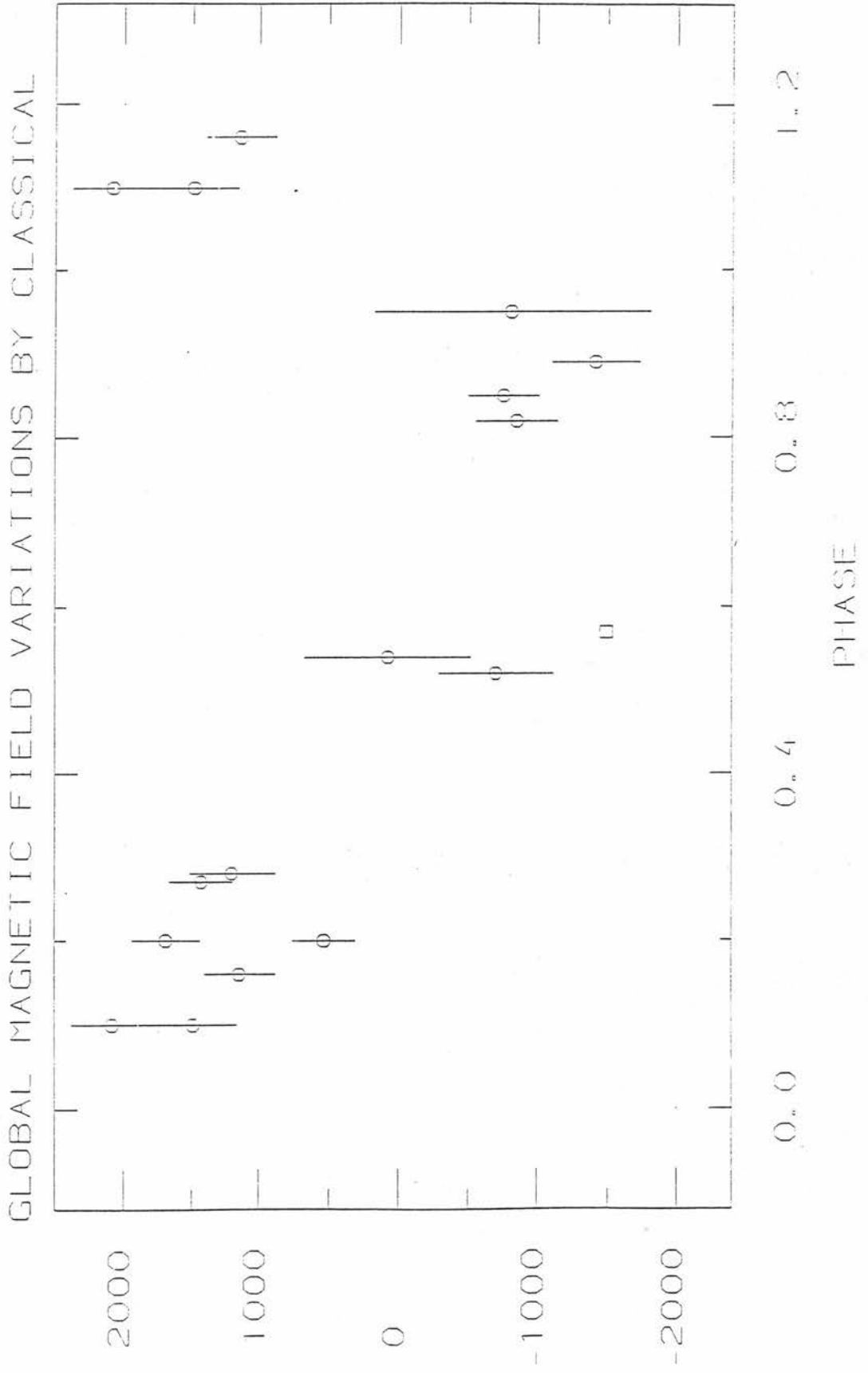
nelling of ion species by the magnetic fields of Ap stars is readily acceptable. The hypothesis outlined above bears some semblance to the abundance anomaly theory of Havnes & Conti (1971), save that in this case it is presumed that the Ca-II ions originate from the star, and are not accreted from the interstellar medium, as proposed by the previous authors.

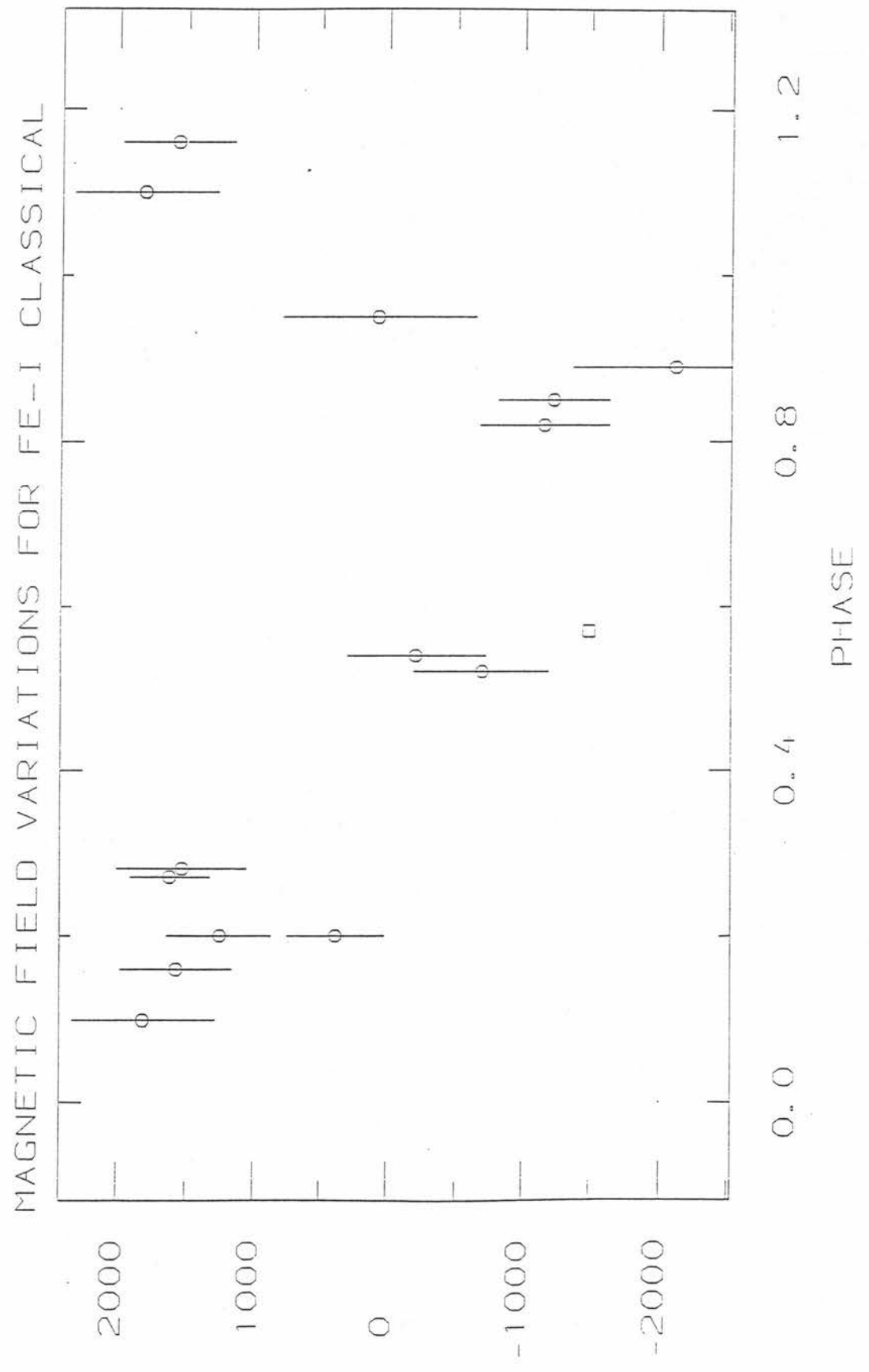
II.7.1 Conclusions

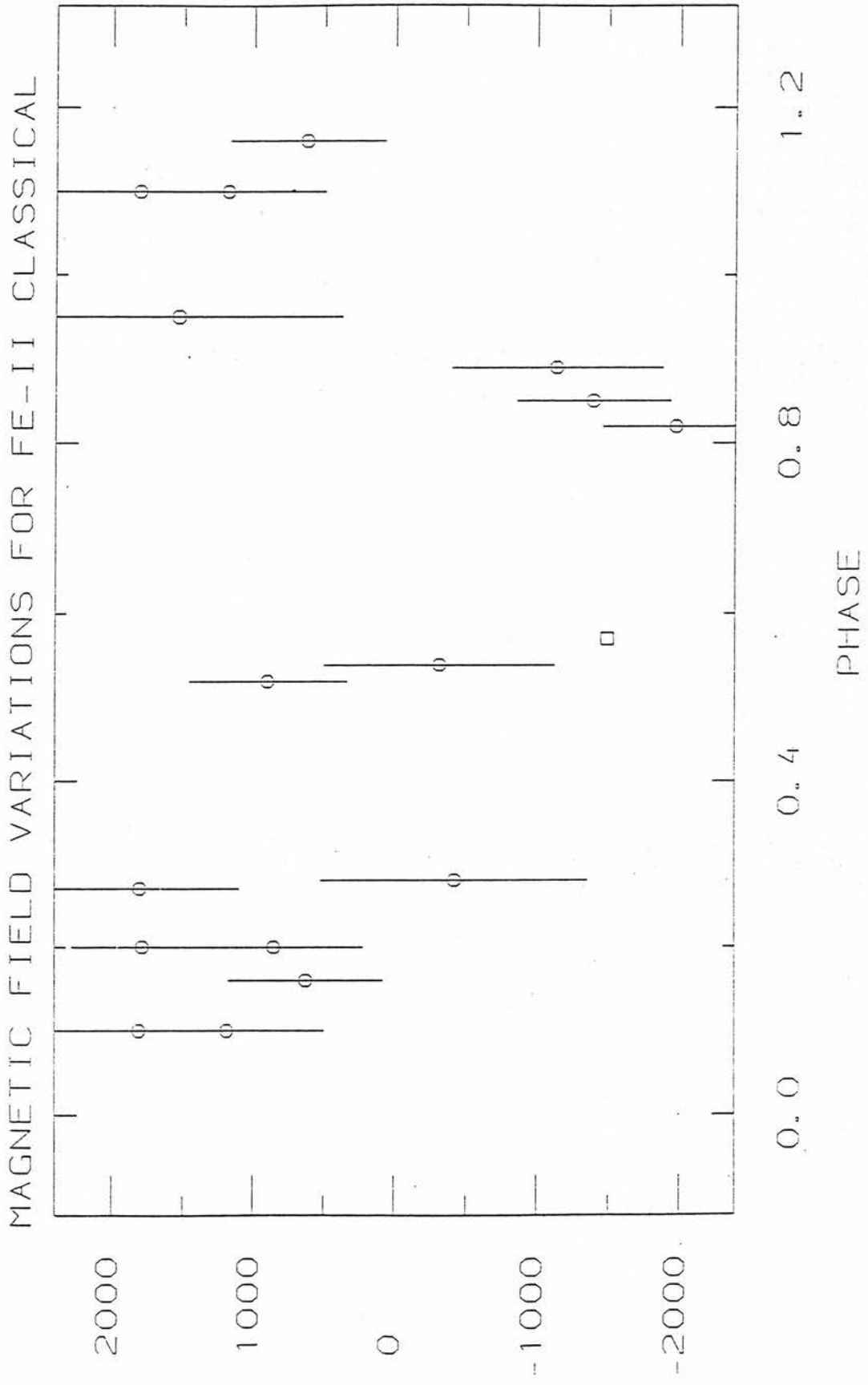
From the close correlation of results between those of the cross-correlation method, and those of Pilachowski et al, it is seen that cross-correlation will function very effectively on real data, and not just synthetic data, as concluded in section I.11.1. The results obtained, quite apart from the ease and speed of attainment, show comparable accuracy and internal consistency at phases where multiple measurements are obtained. The close correlation of error values between Pilachowski's and those contained here, perhaps indicate that the errors are a function of the spectrogram quality, and not dependent upon the accuracy of measurement. Since it is now possible, with the use of Reticon and CCD detectors to obtain better quality spectra, it is expected that the errors incurred by cross-correlation will be lower using contemporary detectors, than the baked photographic emulsion used in this analysis.

The procedures described should enable the automated, fast reduction of magnetic-field data and, though not completely user independent, allow for a considerable enhancement in ease of data reduction.

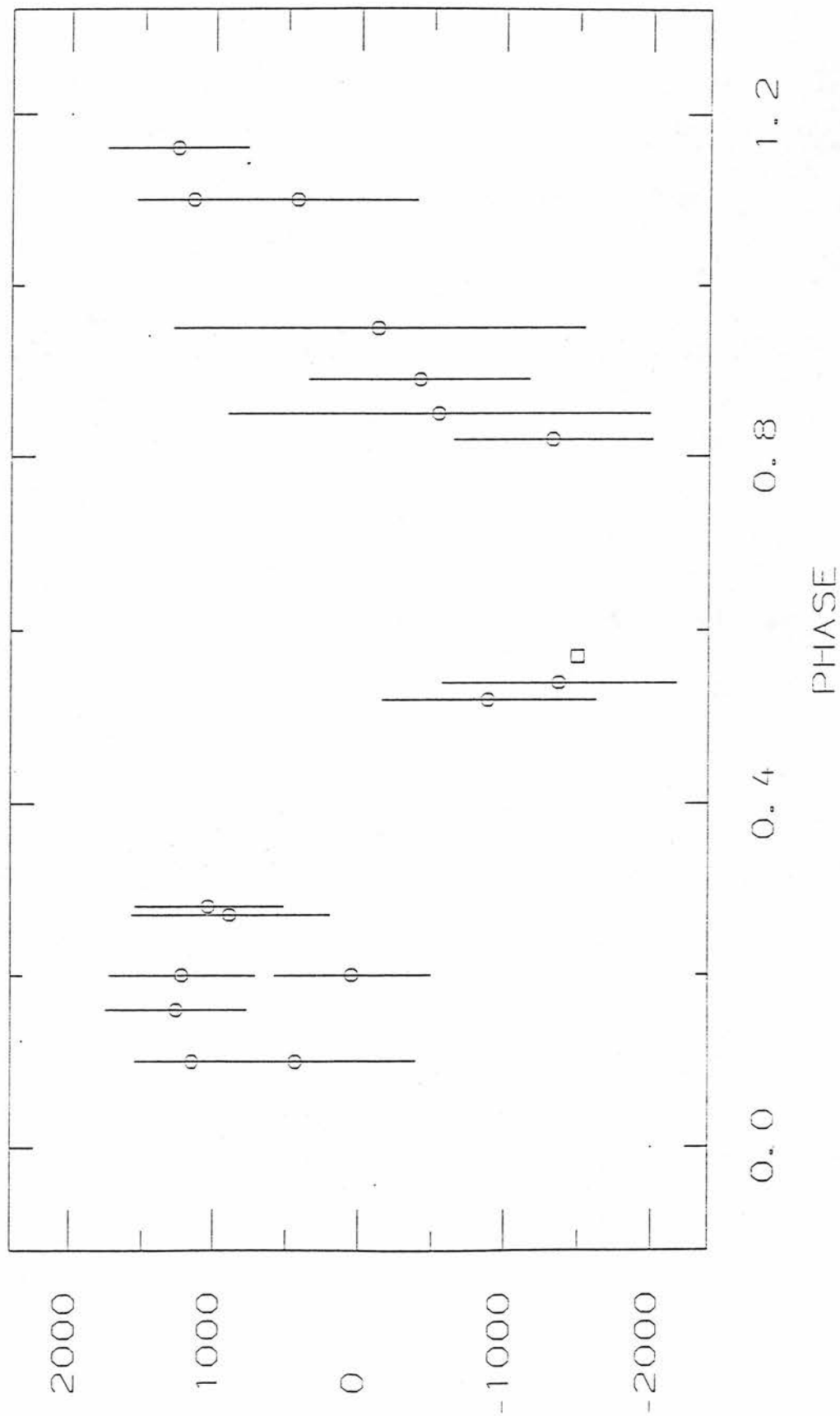
Fig - XXVI a

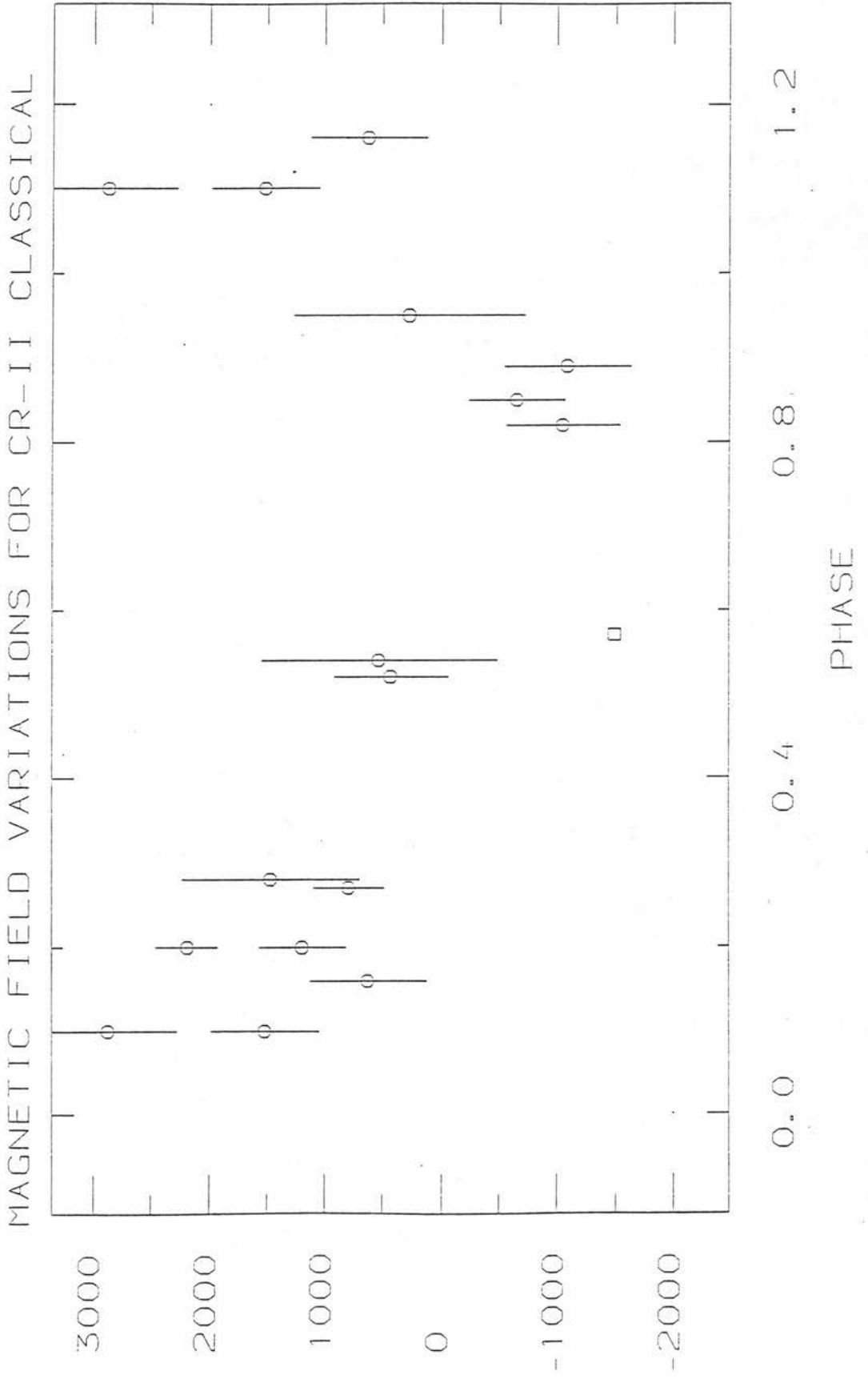






MAGNETIC FIELD VARIATIONS FOR CR-I CLASSICAL





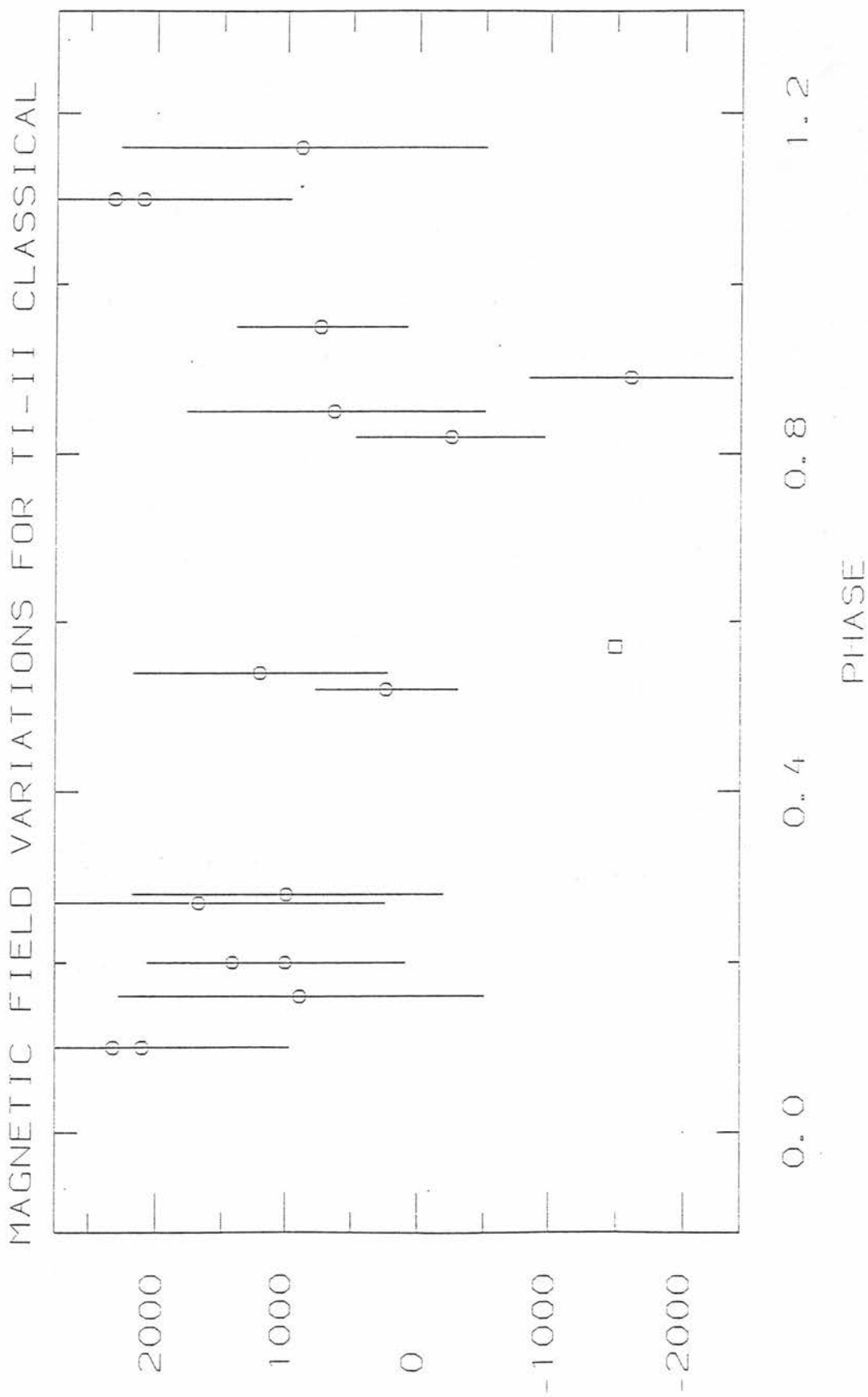
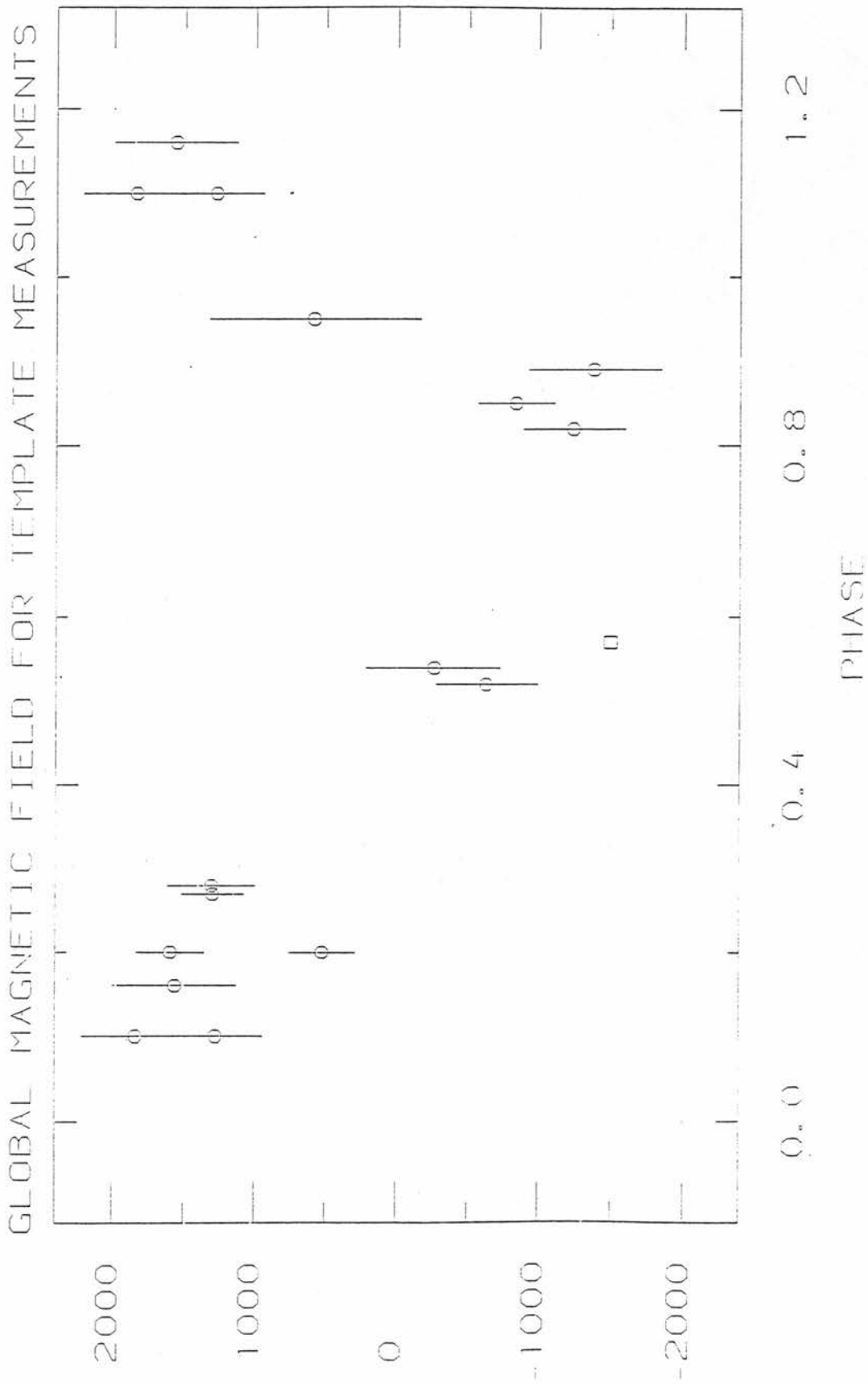
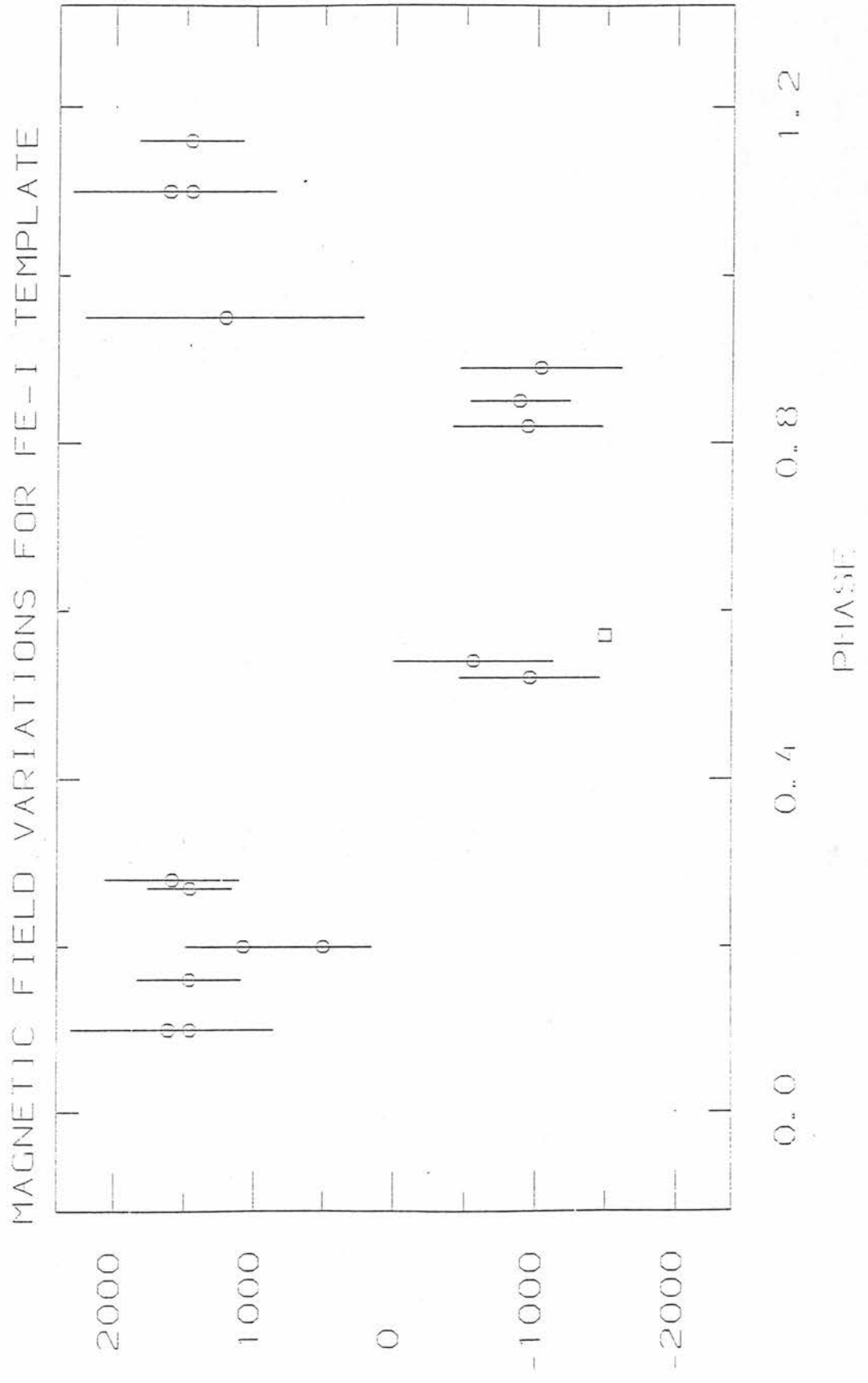
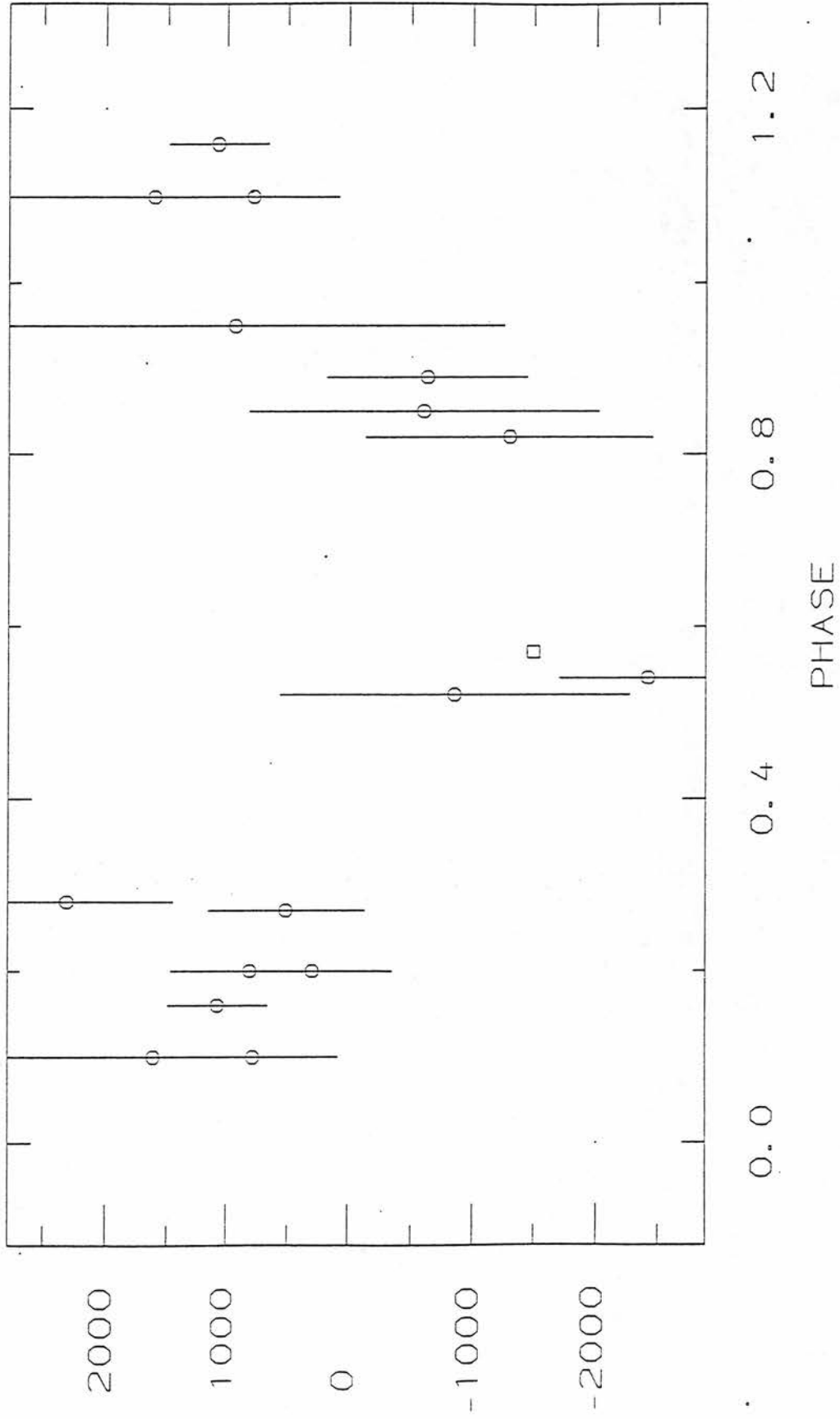


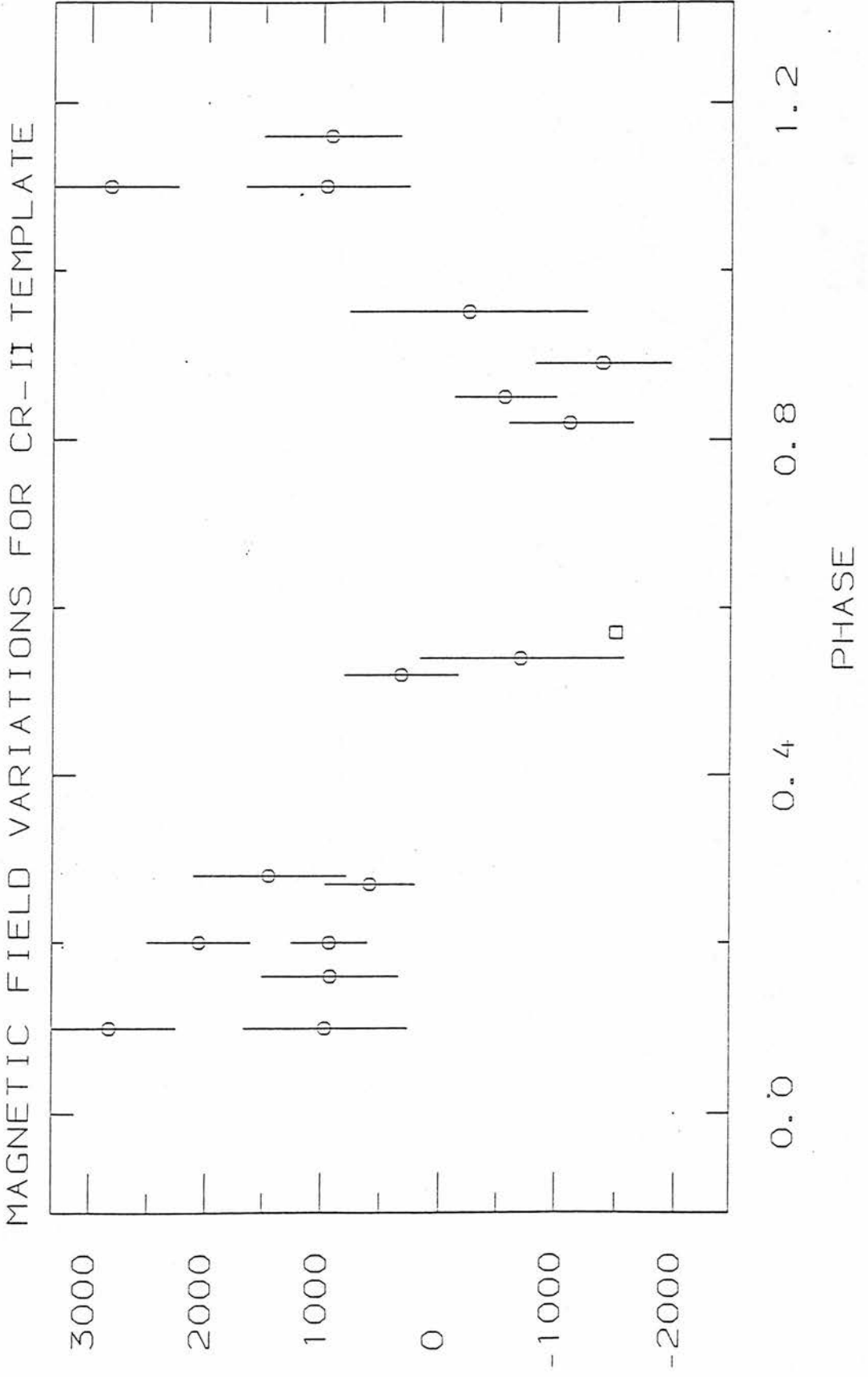
Fig - XXVIII a





MAGNETIC FIELD VARIATIONS FOR CR-I TEMPLATE





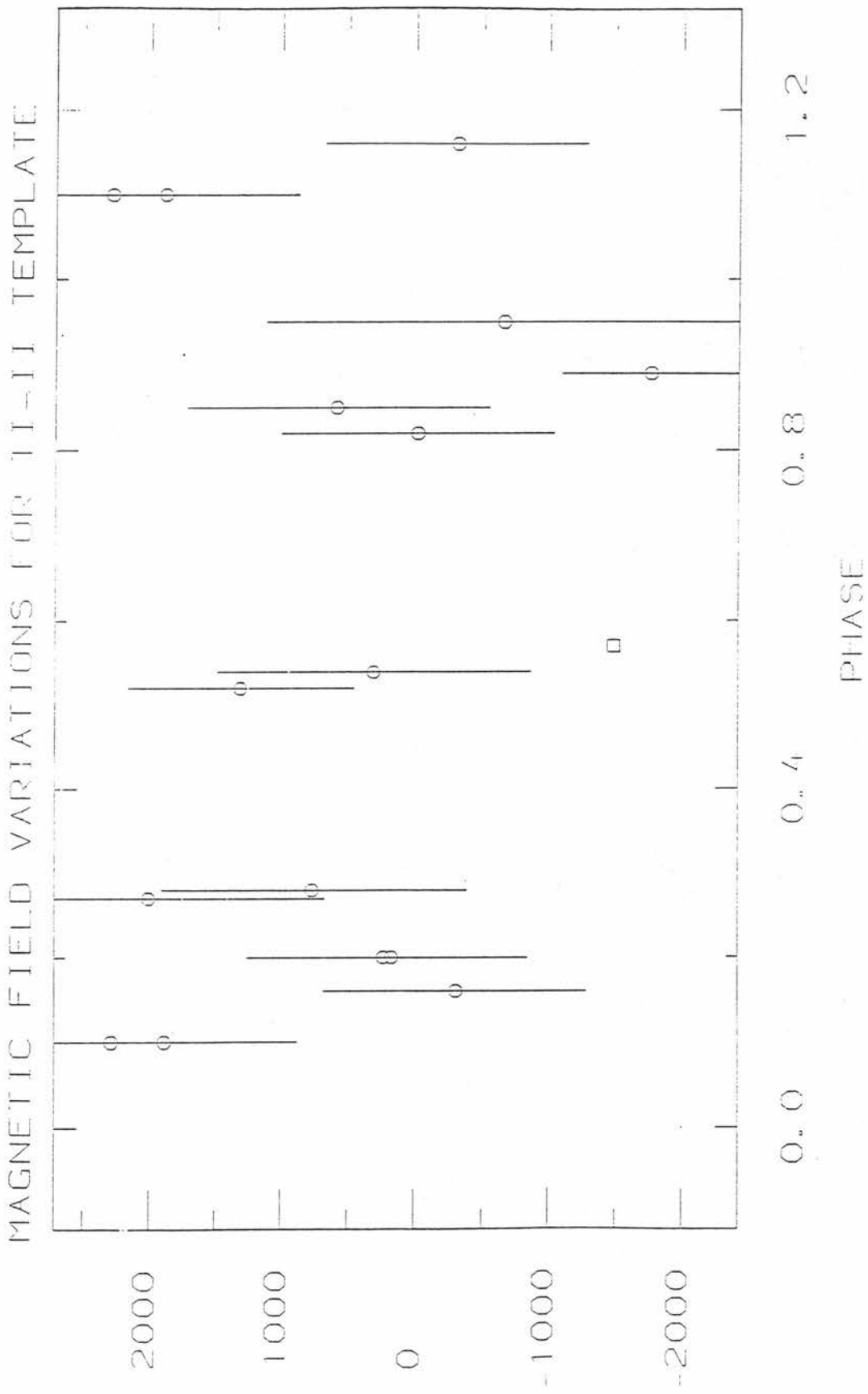
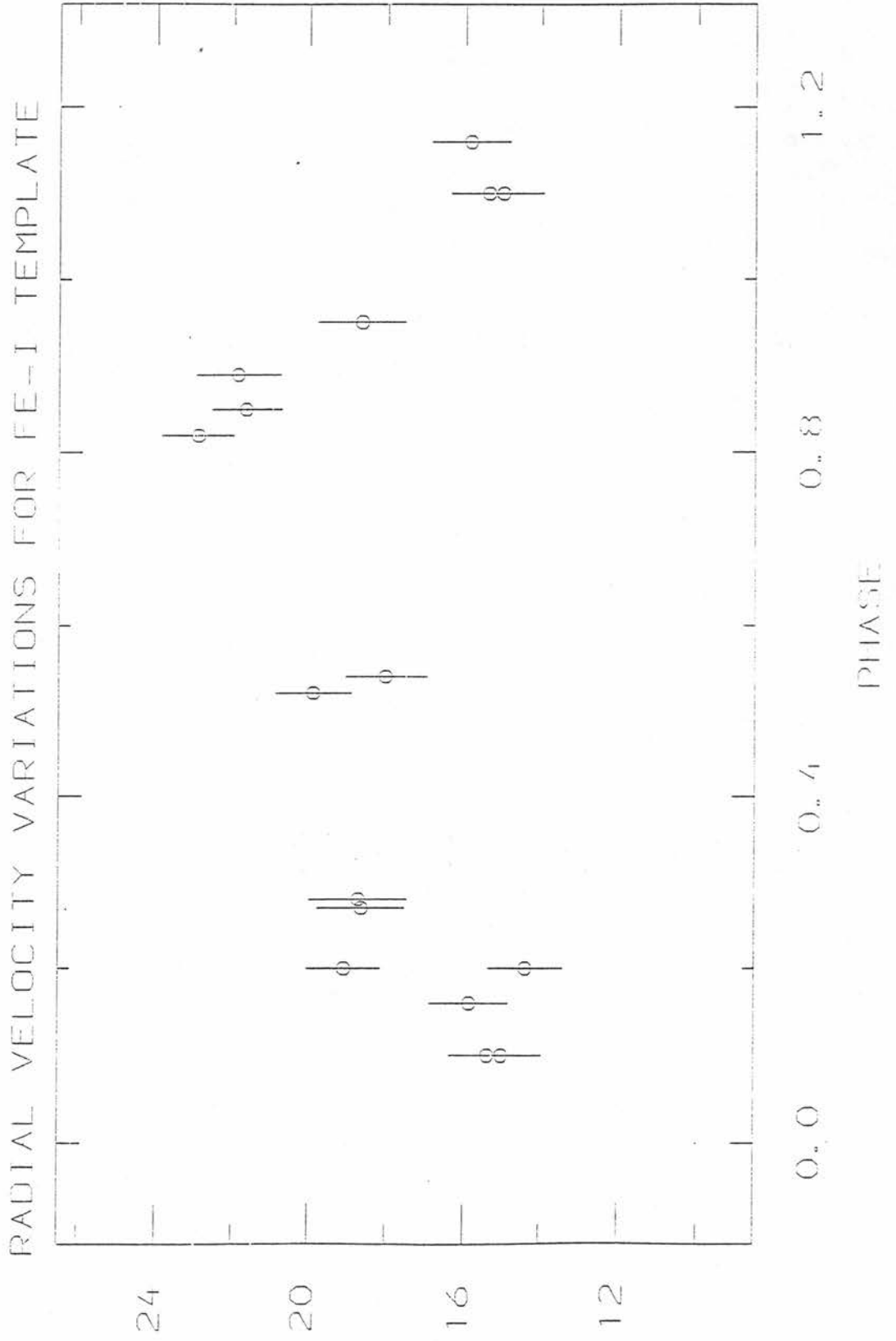
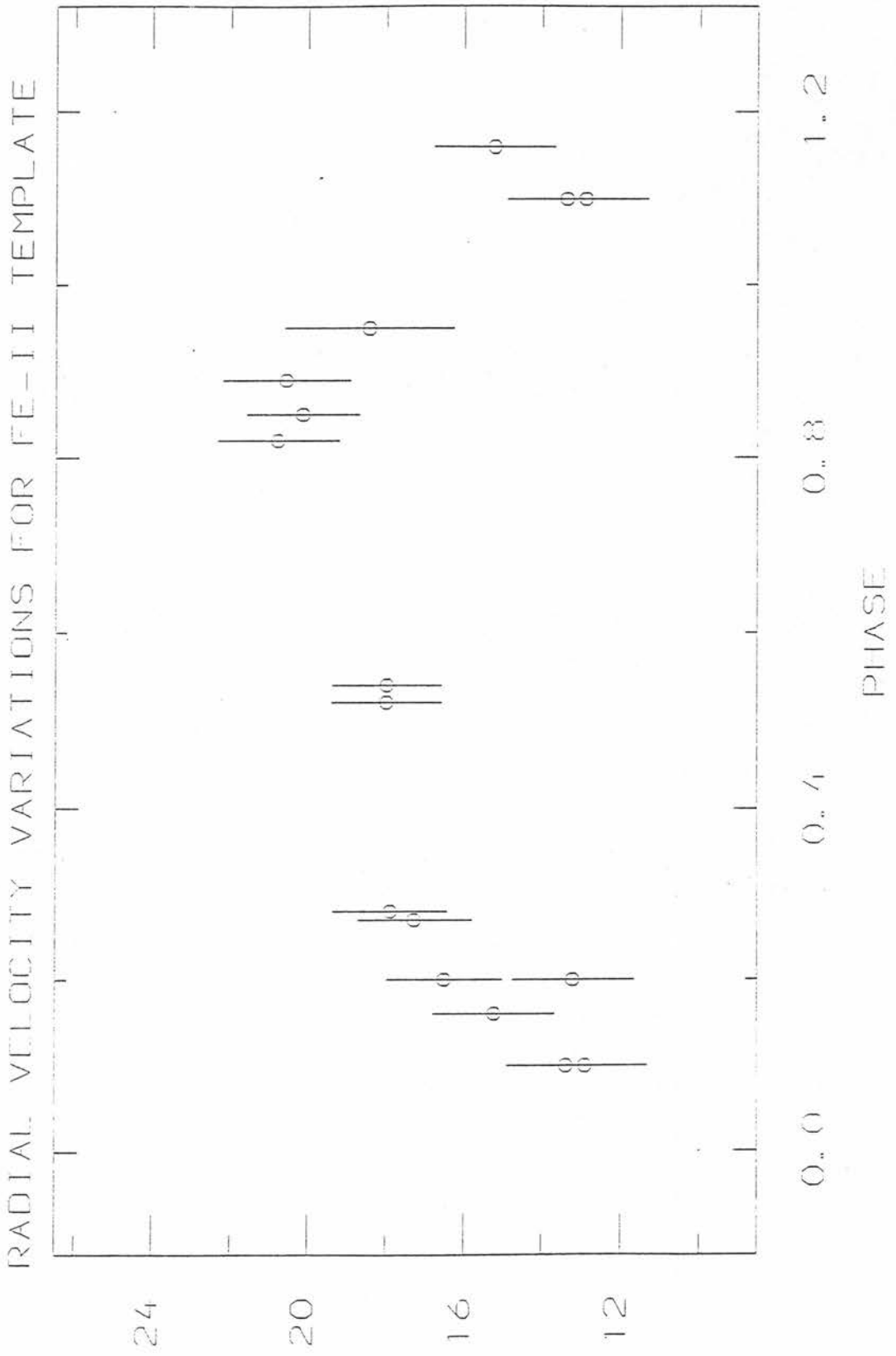
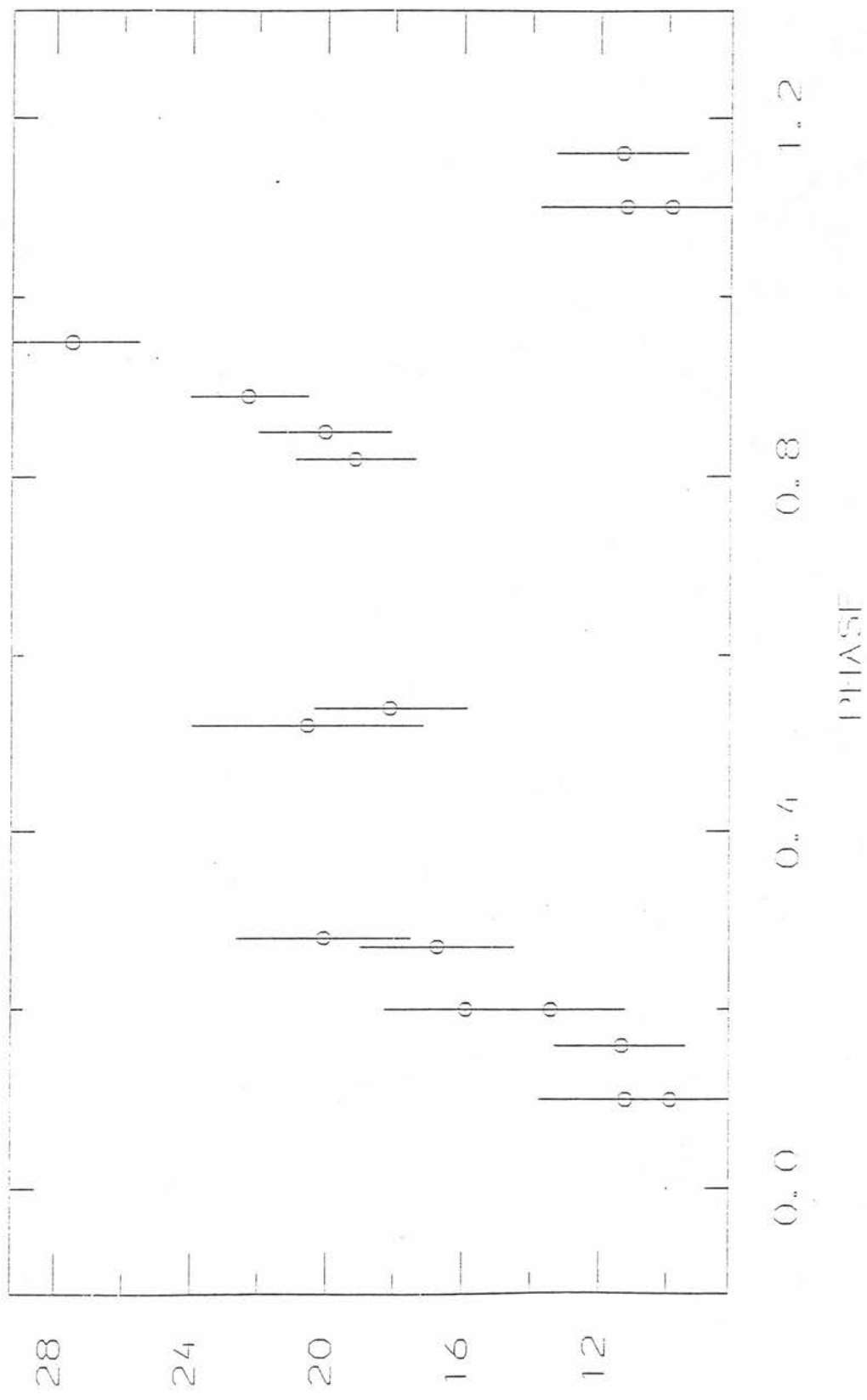


Fig - XXIX a

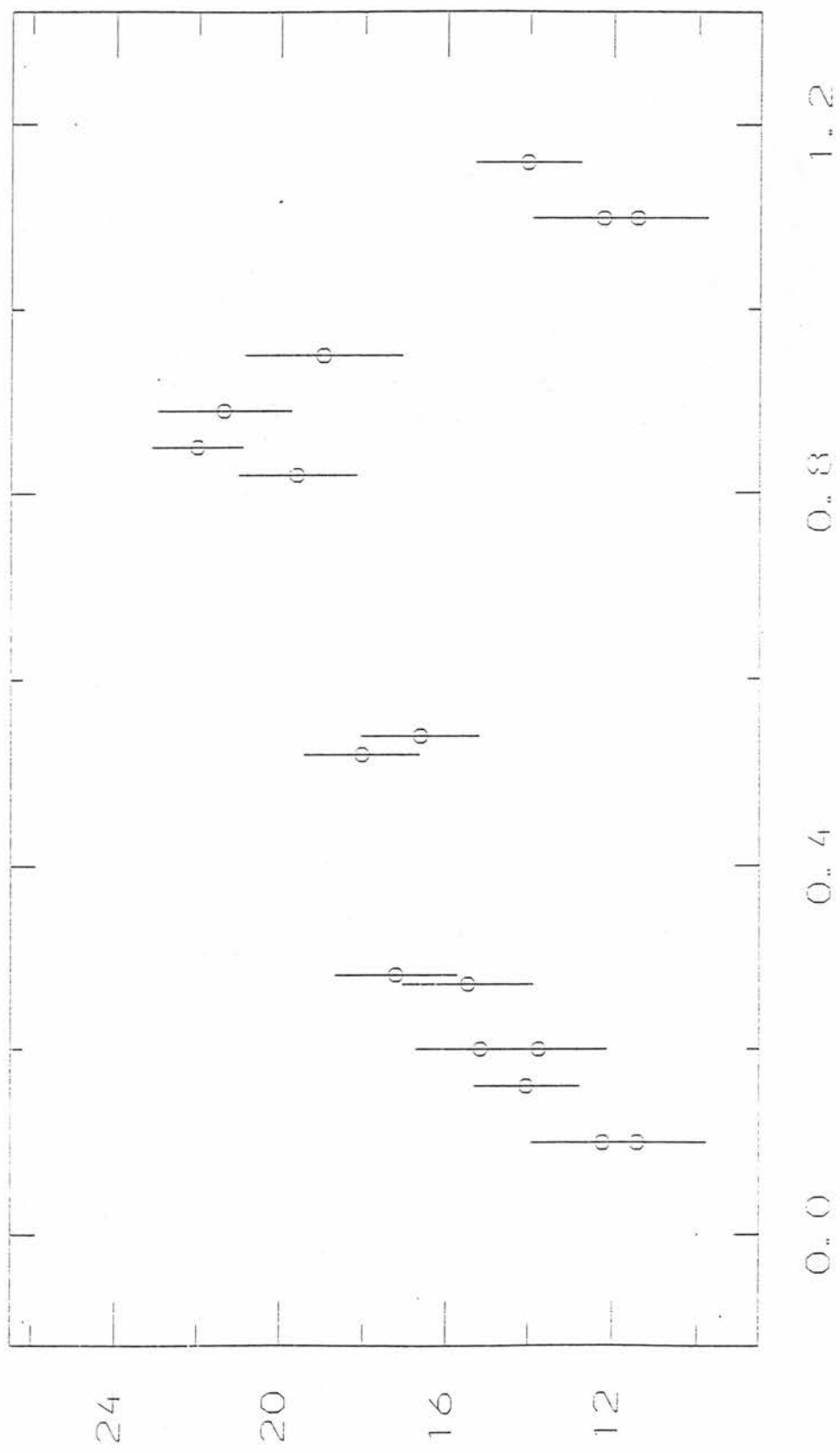




RADIAL VELOCITY VARIATIONS FOR CR-I HD49976



RADIAL VELOCITY VARIATIONS FOR CR-II TEMPLATE



PHASE

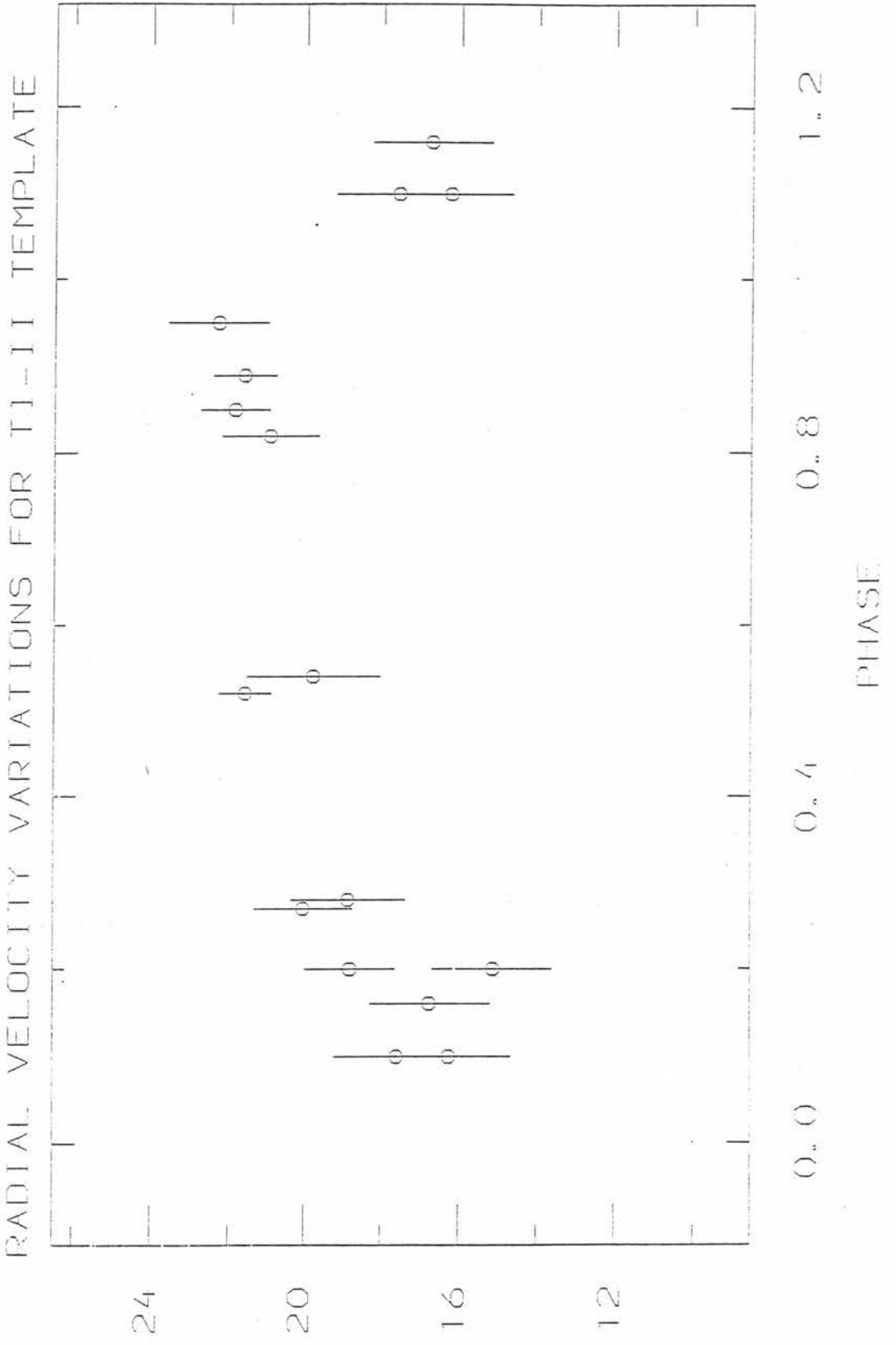
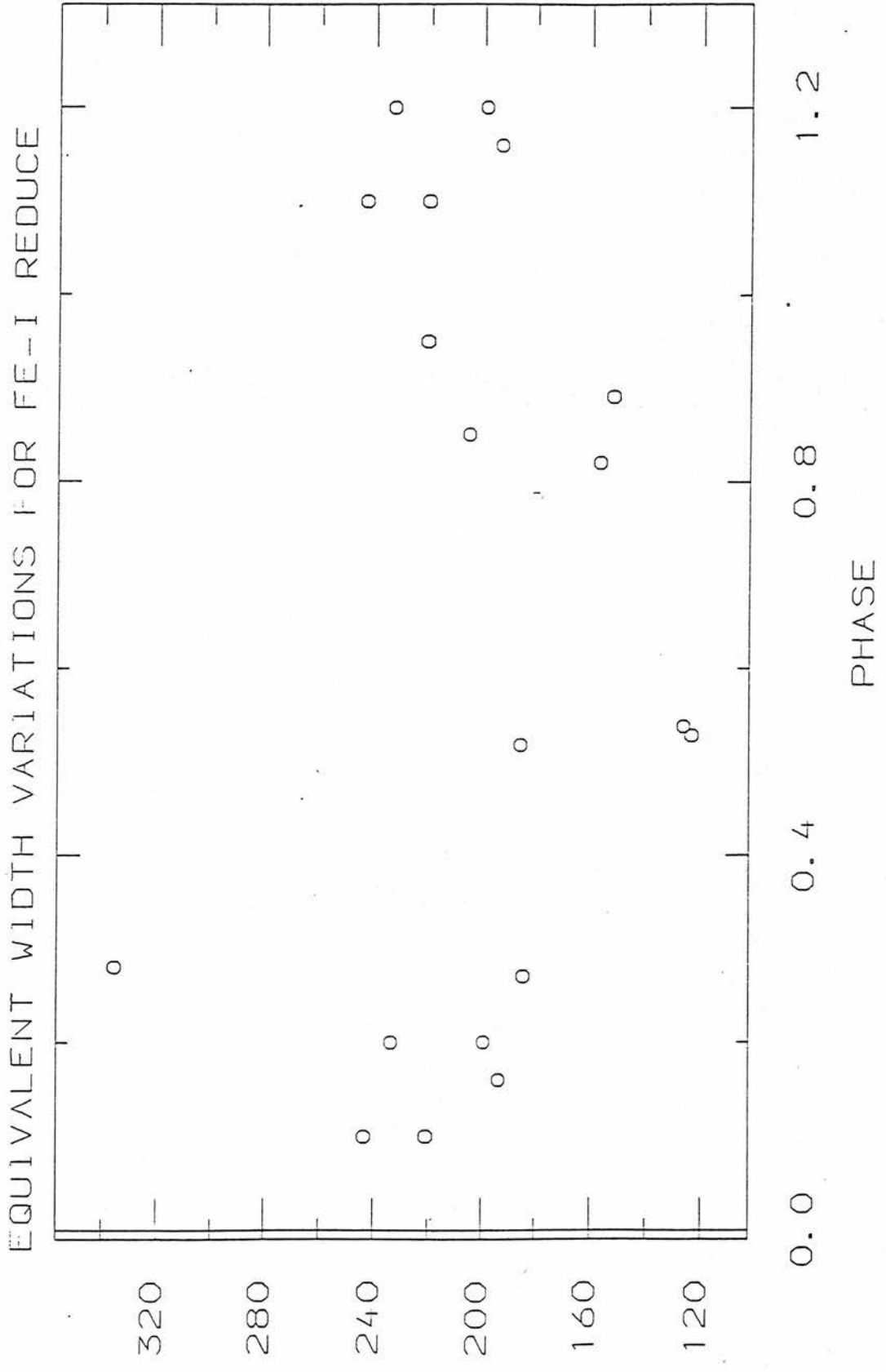
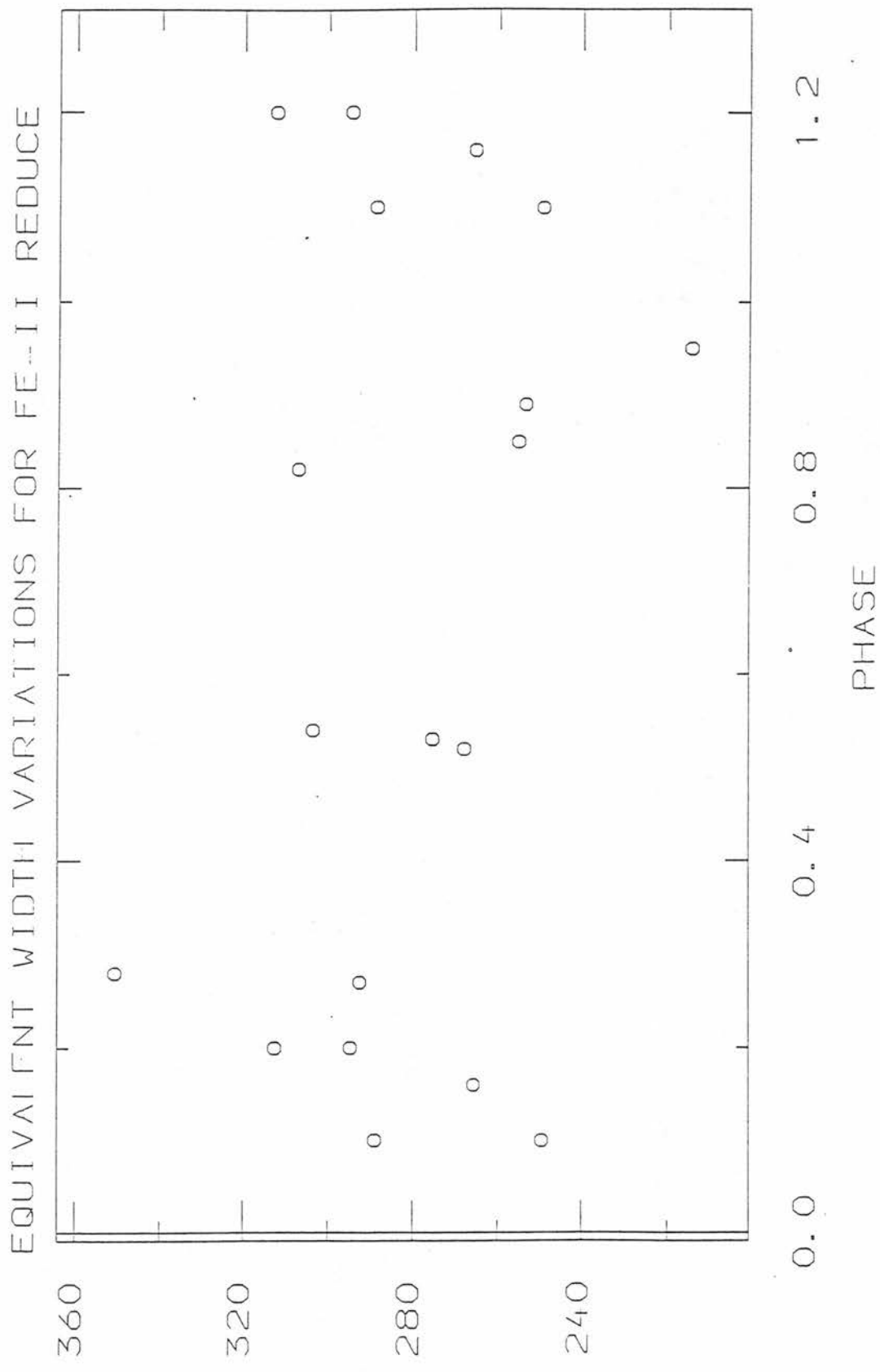
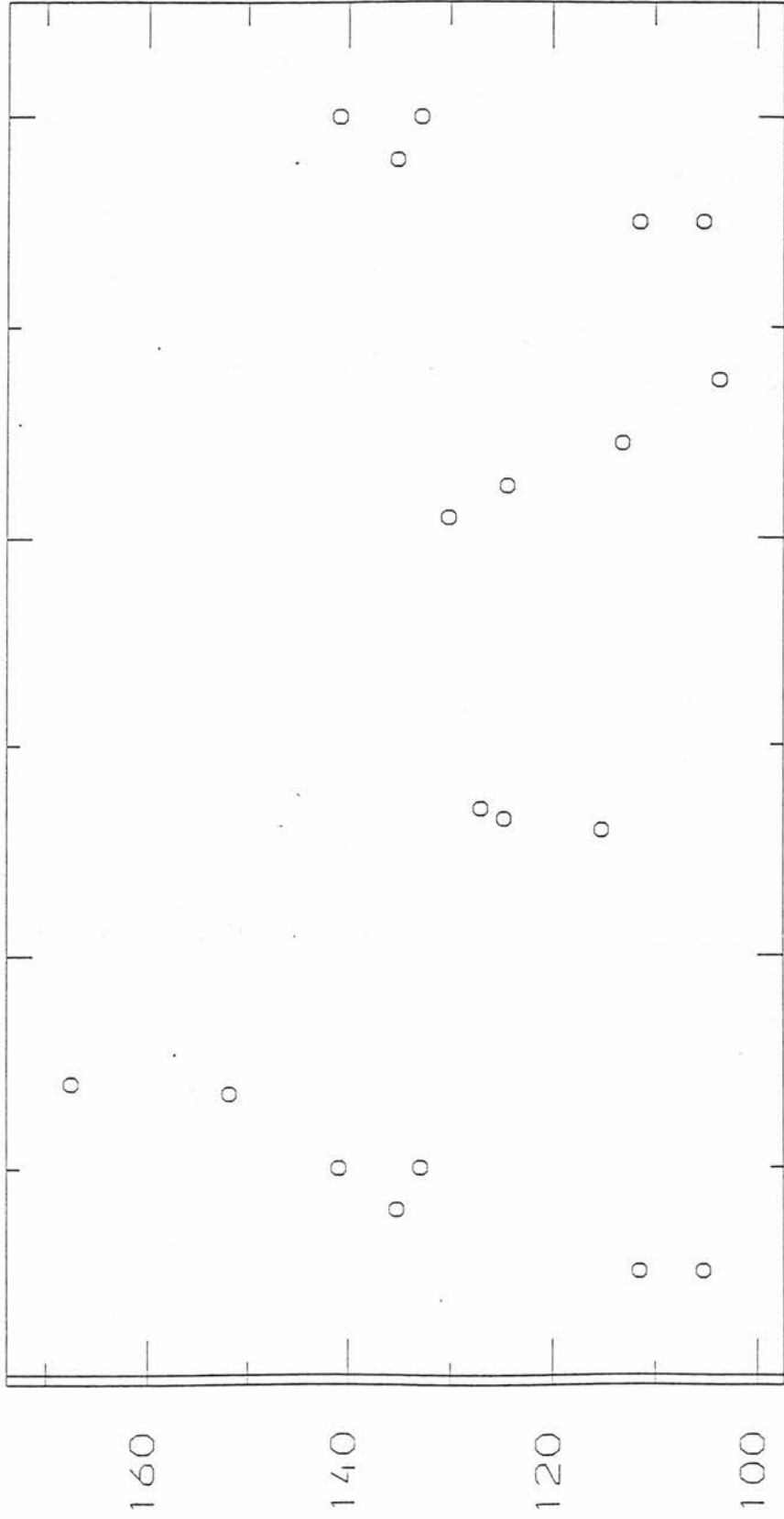


Fig - XXX a





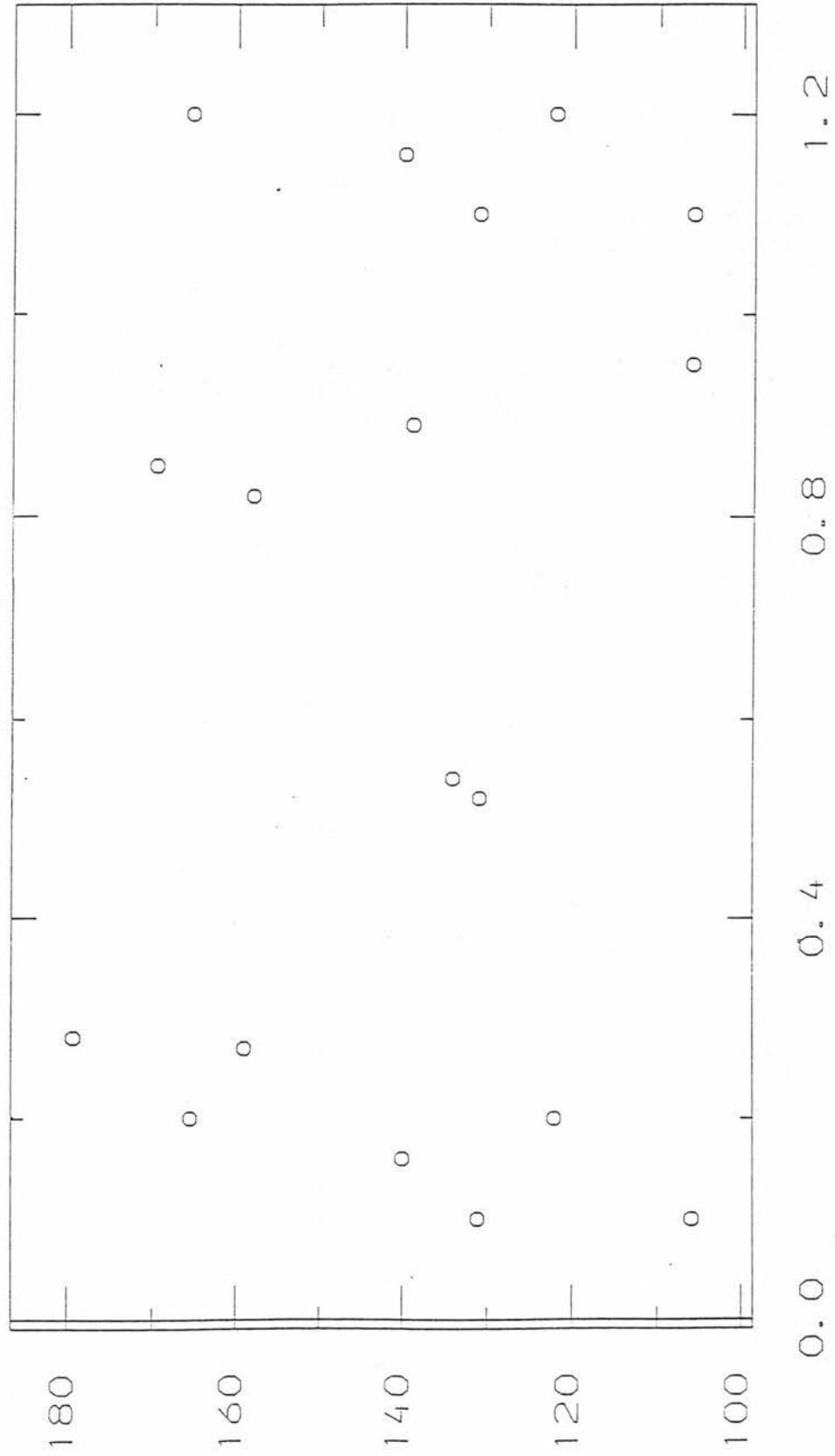
EQUIVALENT WIDTH VARIATIONS FOR CR-I REDUCE



0.0 0.4 0.8 1.2

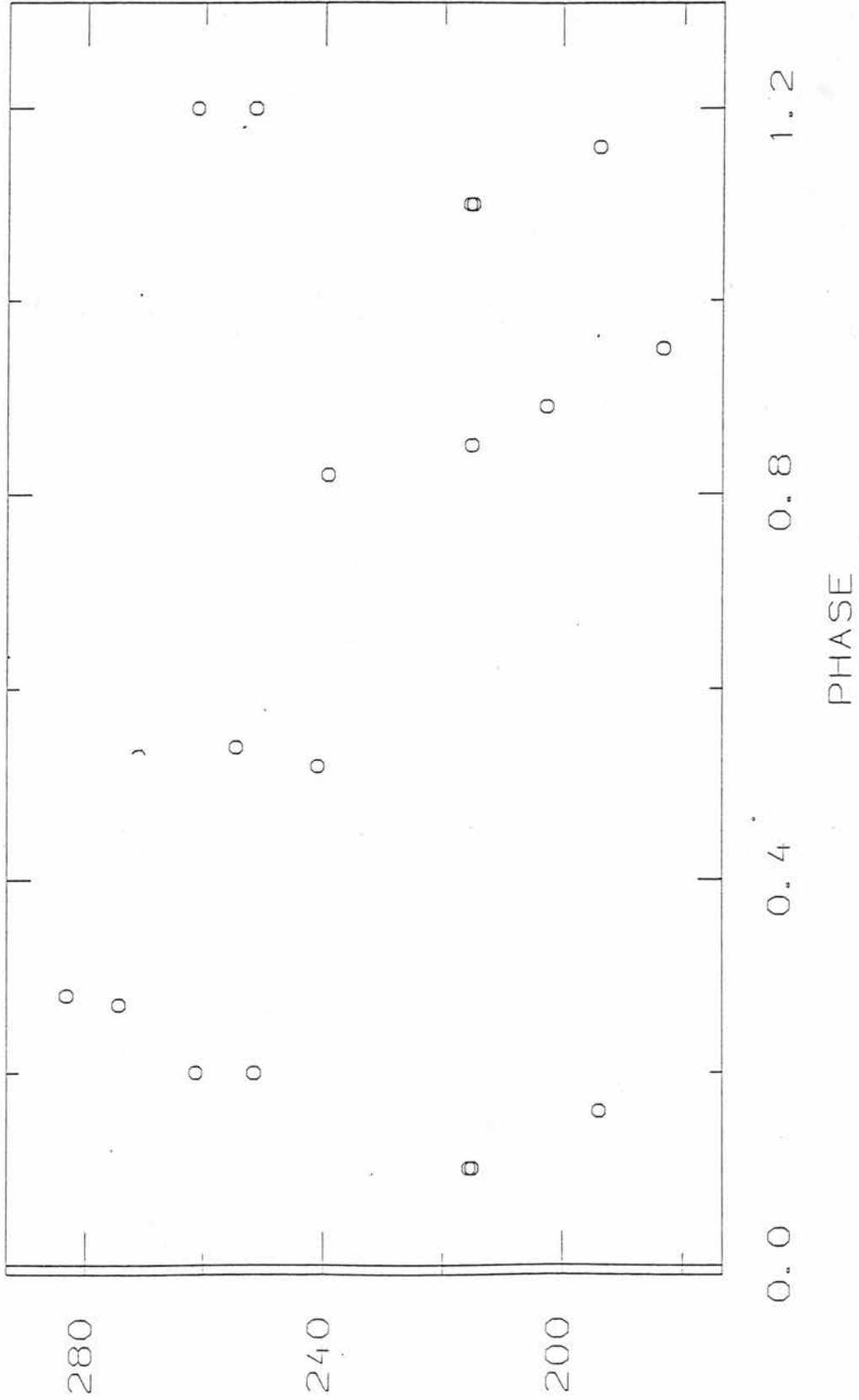
PHASE

EQUIVALENT WIDTH VARIATIONS FOR CR-11 REDUCE



PHASE

EQUIVALENT WIDTH VARIATIONS FOR TI-II REDUCE



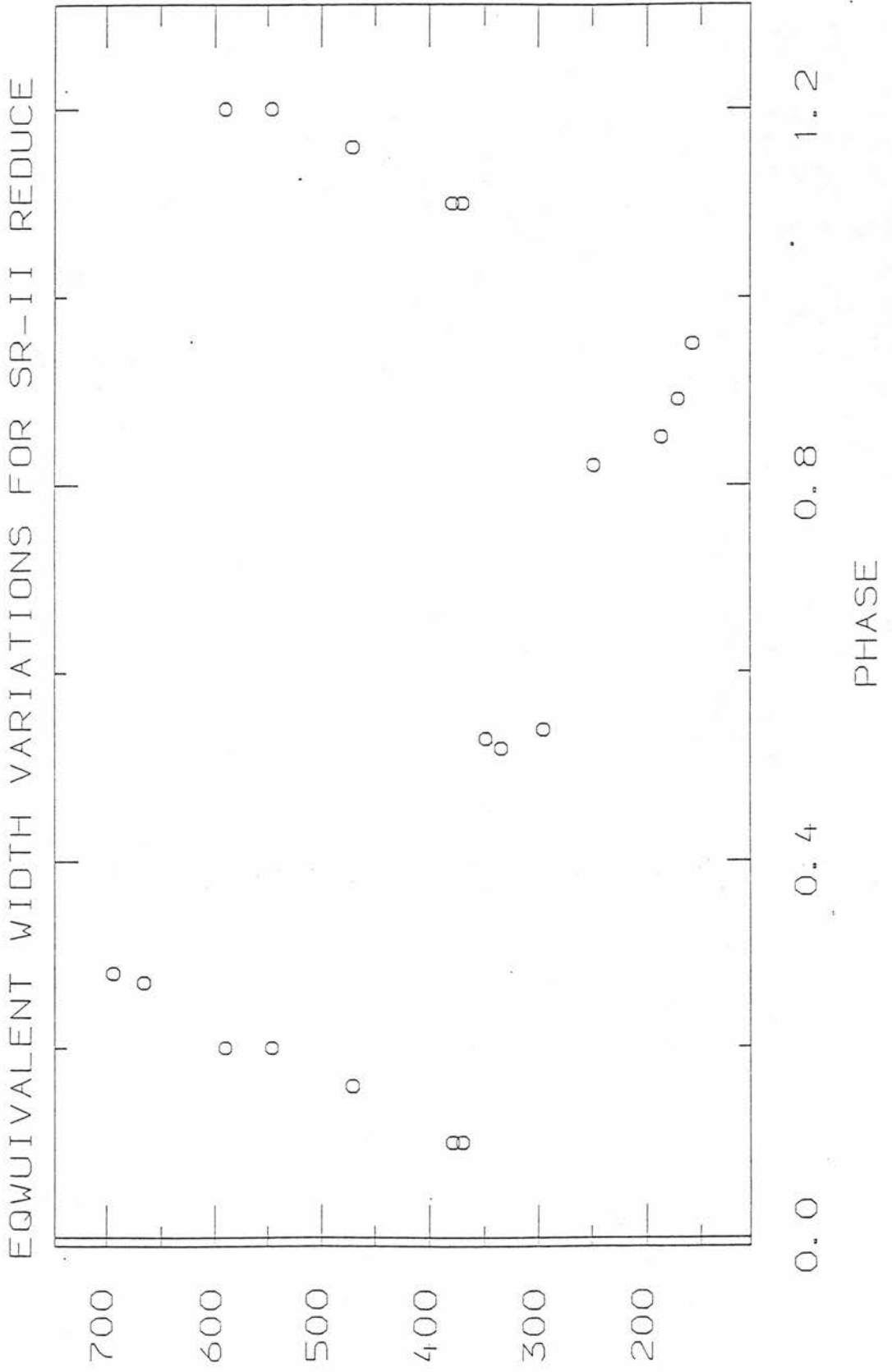


Fig - XXXI a

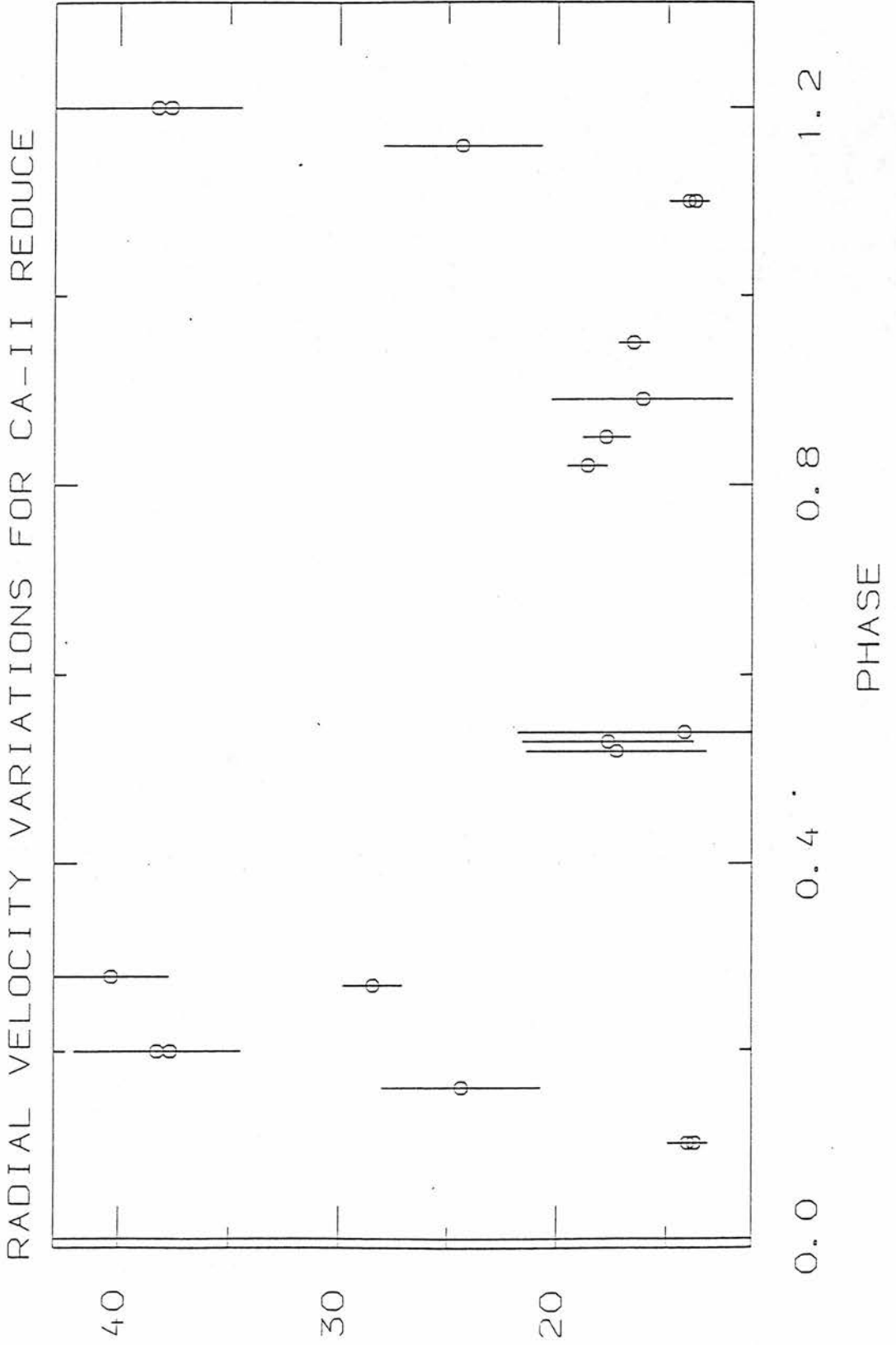
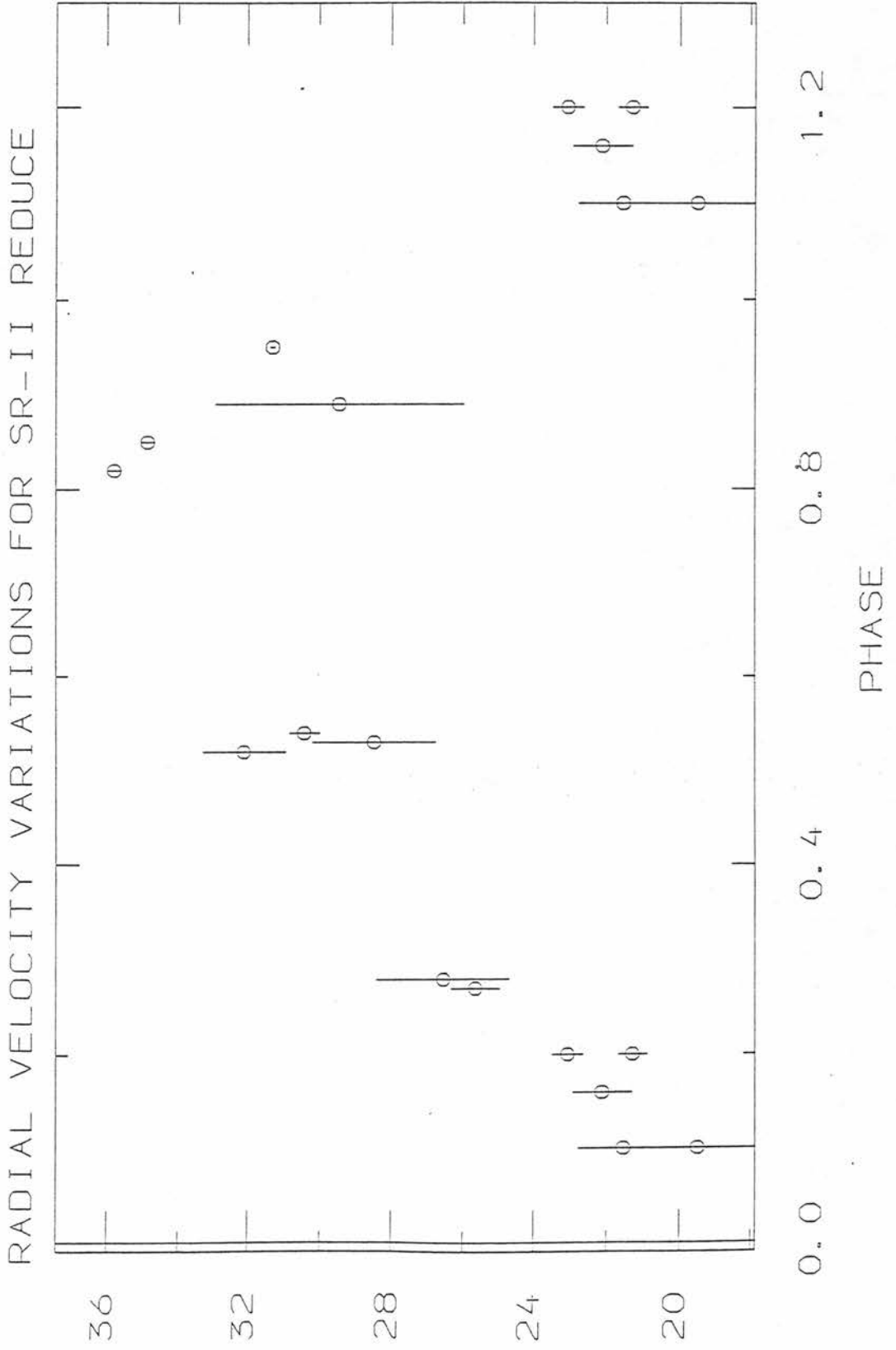


Fig-XXXI b



III. Modelling and theories of magnetic variation

III.1.0 The oblique rotator

Rationales for the observed field variation may be divided into two groups: The variation may be caused by hydromagnetic turbulence within the stellar atmosphere, or by the rotation of the star causing the two poles, one after the other, to become visible.

Oscillation theories such as those proposed by Schwarzschild (1949), Cowling (1941) and Steinitz (1965), though explaining some of the magnetic variation manifested, do not account for such observed features as polarity reversal and elemental abundance variations.

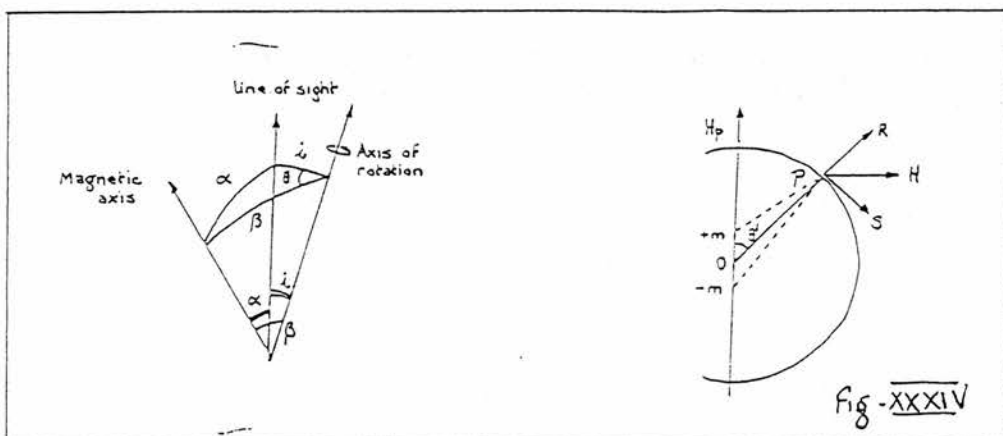
On the basis of this, Stibbs (1950) proposed that the field variations be caused by different aspects of an inclined dipole being observed as the star rotates. This elegant and simple explanation has since become the accepted origin of the observed variations following the work of Deutsch (1958), Pyper (1969), Preston (1970) and many others. The perhaps decisive proof of this theory was conducted by Borra & Vaughan (1976).

Borra & Vaughan proposed to measure the variation of the electric vector for incident light as a function of phase. After Borra, the π component of the zeeman pattern is linearly polarized with electric vector perpendicular to the field, while the σ components, in general elliptically polarized, have electric vector elliptically parallel to the field. In the oblique rotator model, as the star rotates, the magnetic field and electric vector of the polarized light will describe a 360° rotation, as the linearly polarized light undergoes transformation into circular polarized, and back again.

Borra & Vaughan found that rotation of the electric vector was indeed observed in accordance with the oblique rotator, and importantly, that no other explanation for the observed rotation could be subscribed to. Rotation was also

observed by Kemp & Wolstencroft (1974) in the continuum polarization of 53 Cam. Though in keeping with the oblique rotator model, other non-magnetic origins have been suggested for this polarization, defying conclusive proof in this case.

Stibbs considered the expected magnetic field that may be observed, assuming a centered dipole whose inclination to the line of sight α , and with inclination to the rotational axis β . This geometry, (fig (XXXIV)) allows the calculation of the observed integrated zeeman splitting over the visible hemisphere, corresponding to the spectroscopically measured quantity, H_z .



Assuming a linear law of limb darkening,

$$I(\theta) = I_0(1 - u + u \cos \theta) \quad (3.1)$$

The measured effective field is then given by the integrated effect of the longitudinal field H_z over the visible hemisphere,

$$\langle H_z \rangle = \frac{\int_0^{\frac{\pi}{2}} \int_0^{2\pi} H_z(\theta, \phi) I(\theta) \sin \theta \cos \theta d\theta d\phi}{\int_0^{\frac{\pi}{2}} \int_0^{2\pi} I(\theta) \sin \theta \cos \theta d\theta d\phi} \quad (3.2)$$

The magnetic potential at any point on the stellar surface, P, with magnetic colatitude θ' is given by,

$$V = \frac{M \cos \theta'}{r^2} \quad (3.3)$$

where $M = md$, the dipole strength caused by magnetic poles of strength $\pm m$, separated by a distance d . Differentiation with respect to r , and θ' gives the radial and transverse components of the field,

$$R = -\frac{\delta V}{\delta r} = \frac{2M \cos \theta'}{r^3} \quad T = -\frac{1}{r} \frac{\delta V}{\delta \theta'} = \frac{M \sin \theta'}{r^3} \quad (3.4)$$

In order to calculate the longitudinal field H_z , it is necessary to compute the components H_x, H_y, H_z where X, Y, Z are the co-ordinates of P from

$$H_z = R \cos \theta' - T \sin \theta' = \frac{M}{r^5} (2Z^2 - X^2 - Y^2) \quad (3.5)$$

$$H_x = (R \sin \theta' + T \cos \theta') \cos \eta' = \frac{3M}{r^5} XZ$$

Where

$$\cos \eta' = \frac{X}{(X^2 + Y^2)^{\frac{1}{2}}}$$

The longitudinal magnetic field then follows as

$$H_z = H_Z \cos \alpha - H_X \sin \alpha \quad (3.6)$$

Performing a co-ordinate transform from the magnetic axes X, Y, Z to the rotational axes x, y, z where

$$X = x \cos \alpha - z \sin \alpha \quad Y = y \quad Z = z \cos \alpha + x \sin \alpha \quad (3.7)$$

and then changing to spherical polar co-ordinates

$$x = r \sin \theta \cos \phi \quad y = r \sin \theta \sin \phi \quad z = r \cos \theta$$

we obtain H_z in terms of $H_z(\theta, \phi)$. The effective magnetic field $\langle H_z \rangle$ may then be evaluated according to the recursion relations,

$$F_{m,n} = \int_0^{\frac{\pi}{2}} \sin^m \theta \cos^n \theta d\theta = \begin{cases} \frac{n-1}{m+n} F_{m,n-2} & n > 1 \\ \frac{m-1}{m+n} F_{m-2,n} & m > 1 \end{cases} \quad (3.8)$$

Evaluation obtains,

$$\begin{aligned} \langle H_z \rangle &= \frac{M \cos \alpha}{10r^3} \frac{15 + u}{3 - u} \\ &= \frac{1}{20} H_p \frac{15 + u}{3 - u} \cos \alpha \end{aligned} \quad (3.9)$$

where H_p is evaluated from,

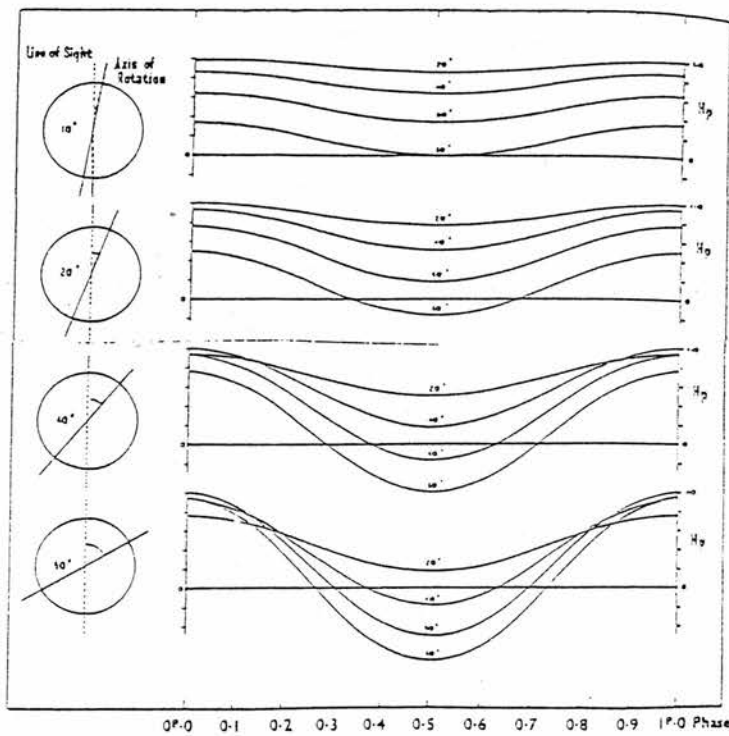
$$H_p = -\left(\frac{\delta V}{\delta r}\right)_{\theta'=0} = \frac{2M}{r^3}$$

α may be evaluated by consideration of the two angles i, β as,

$$\cos \alpha = \cos i \cos \beta + \sin i \sin \beta \cos \theta \quad (3.11)$$

where θ varies from zero to 2π .

Stibbs then computed theoretical variations for any given angles of i, β (fig (XXXV)) showing unequivocally that magnetic polarity reversal may be observed for values of $i + \beta > \frac{\pi}{2}$



Using the following definition for the ratio of the magnetic extrema,

$$r = \frac{\langle H_z(max) \rangle}{\langle H_z(min) \rangle} = \frac{\cos(i + \beta)}{\cos(i - \beta)} \quad (3.12)$$

the values of r may be linked to the geometry of an observed star by means of Eq. (3.12). When $i=0$ then the star is viewed along the axis of rotation and no variation in the magnetic field strength will be observed, regardless of β . If $i + \beta = \frac{\pi}{2}$, corresponding to $r = 0$, then magnetic variation will occur decreasing to $\langle H_z \rangle = 0$, though polarity reversal does not occur. Finally, if $i + \beta > \frac{\pi}{2}$ then polarity reversal will occur.

Though this model explains many of the gross features of the magnetic field, variation of magnetic field with phase and polarity reversal in some cases, later work by Deutsch (1958) and Pyper (1969) required that the assumption of a central dipole be modified to explain the anharmonic variations observed. As such, Landstreet (1970) and Preston (1970) proposed that a required field configuration may be produced by the evaluation of the effects of non-central dipole, shifted by a fractional amount a , along the magnetic axis.

III.1.1 The decentred dipole

Following Henseberge et al (1977), the polar field strengths are equal to,

$$\pm \frac{H_p}{(1 \mp a)^3} \quad (3.13)$$

and the longitudinal field is

$$H_z = -\frac{H_p}{2} \left[(1 + a \cos \theta - 2a^2) \cos i + 3(1 - \rho^2)^{\frac{1}{2}} (a - \cos \theta) \right] \times (1 + a^2 - 2a \cos \theta)^{-\frac{5}{2}} \quad (3.14)$$

where ρ, ω are polar co-ordinates upon the visible disc, and $\rho = \sin u$. The integrated magnetic field over the visible hemisphere is then

$$H_e = \frac{\int \int H_z I \rho d\rho d\omega}{\int \int I \rho d\rho d\omega} \quad (3.15)$$

In general, the longitudinal field components H_z may be written as a power series in a

$$H_z = \sum_{n=0}^{\infty} \frac{a^n}{n!} \left(\frac{d^n H_z}{da^n} \right)_{a=0} \quad (3.16)$$

resulting in

$$H_e = H_e(a=0, i, \beta) + \frac{3\beta H_p}{3-\beta} \sum_{n=1}^{\infty} a^{2n-1} \sum_{m=0}^{\infty} C_{2n-1,m} (\cos^2 i)^m + \frac{3(1-\beta)H_p}{3-\beta} \sum_{n=1}^{\infty} a^{2n} \cos i \sum_{m=0}^n C_{2n,m} (\cos^2 i)^m \quad (3.17)$$

where β is the limb darkening co-efficient and $C_{2n-1,m}, C_{2n,m}$ are real numbers, resulting from integrals over ρ, ω . The polynomials in $\cos i$ are found to be proportional to Legendre polynomials for $n=1\dots 5$. Assuming that this

proportionality may be extended to the range $n = 1 \dots \infty$, Eq. (3.16) may be transformed to an absolutely convergent series

$$H_e = \frac{3H_p}{3-\beta} \left\{ \frac{1}{4} \left(1 + \frac{\beta}{15} \right) \cos i + \beta \sum_{n=1}^{\infty} E_{2n-1} a^{2n-1} P_{2n}(\cos i) \right. \\ \left. + (1-\beta) \sum_{n=1}^{\infty} E_{2n} a^{2n} P_{2n+1}(\cos i) \right\} \quad (3.18)$$

where

$$E_{2n-1} = \frac{(-1)^{n-1} (2n+1)!!}{2^n (n+1)(n+2)(2n-1)(n-1)!} \quad E_{2n} = \frac{(-1)^n (2n+1)!!}{2^{n+1} (n+2)n!} \quad (3.19)$$

and

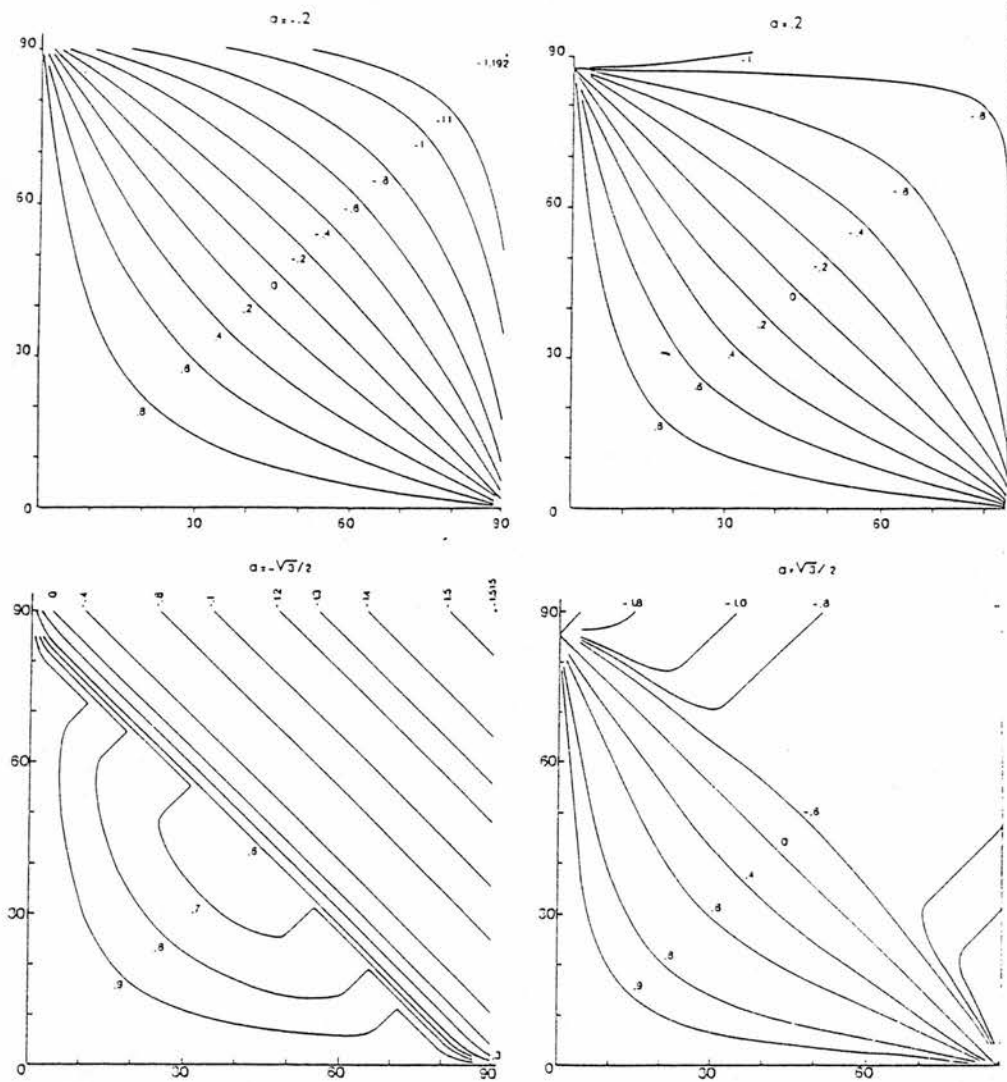
$$(2n+1)!! = (2n+1)(2n-1)(2n-3) \dots (5)(3)(1) \quad (3.20)$$

and by using the recurrence relations

$$E_1 = \frac{1}{4} \quad E_{2n} = \frac{(n+1)(2n-1)E_{2n-1}}{2n} \quad E_{2n+1} = \frac{2n+3}{(n+3)(2n+1)} E_{2n} \quad (3.21)$$

this equation may be analytically evaluated.

Fig (XXXVI) depicts the solution of Eq (3.18) for values of the decentering parameter $a = \pm 0.2, \pm \frac{\sqrt{3}}{2}$. Given an experimental value of r (Eq.3.12) and values of i, β from the oblique rotator model, or other analyses such as that of Deutsch, the decentering parameter may be found with recourse to fig(XXXVI) or another graph of appropriate limb-darkening parameter, β .



Typical curves with constant r in the (27) diagram for various a and $\beta = 0.45$. Each curve is labelled with its corresponding r value

Fig - XXXVII

III.1.2 The Oblique rotator: Quadrupole symmetry

In addition to describing the required surface field as due to a centred or de-centred dipole, the surface field due to a quadrupole may be calculated similarly.

Schwarzchild's (1950) solution for a centred quadrupole produces, for the effective magnetic field

$$H_e = \frac{u}{3-u} H_p \frac{(1 + 3 \cos 2i)}{16} \quad (3.22)$$

Incorporating this additional field into the oblique rotator model, the quadrupole component within a basic oblique rotator in the centred dipole model may eas-

ily be evaluated (Borra (1980)), leading to

$$r = \frac{\kappa_1 \cos(i + \beta) + \kappa_2 Q [1 + 3 \cos 2(\beta + i)]}{\kappa_1 \cos(-i + \beta) + \kappa_2 Q [1 + 3 \cos(\beta - i)]} \quad (3.23)$$

where

$$\kappa_1 = \frac{15 + u}{4(15 - 5u)} \quad \kappa_2 = \frac{u}{16(3 - u)} \quad (3.24)$$

and Q determines the relative strengths of the dipole and quadrupole field. The ratio between the magnetic field strength at the two poles is then given by

$$\frac{1 + Q}{(Q - 1)} \quad (3.25)$$

and by inverting Eq. 3.25, the polar field may be obtained from

$$H_e(\text{extrema}) = H_p \left\{ \kappa_1 \cos(\beta \pm i) + \frac{Q \kappa_2 [1 + 3 \cos 2(\beta \pm i)]}{1 + Q} \right\} \quad (3.26)$$

III.1.3 The symmetric rotator

Another variation of the oblique rotator model was proposed by Krause (1971), Krause & Oetken (1976) and Oetken (1977). This model 'the symmetric rotator' proposed that magnetic stars have field distributions that are either symmetric, or antisymmetric under reflection within the magnetic equator. Krause states that this may be attained by judicious application of dipole and quadrupole fields, such as a dipole lying in the rotational equator, and a quadrupole, parallel to the rotational axis. A second field distribution of both dipole and quadrupole parallel to one another, within the rotational equatorial plane was suggested to explain radial velocity variations in $\alpha^2 CVn$.

However, this model was found by Borra & Landstreet (1978) to be unable to mirror the field variations found in HD215441. The symmetric rotator is physically very similar to the oblique rotator save in cases where polarity reversal is absent. Only in the a case of non-reversal is it possible to test the veracity of the theory. As HD215441 was found to have a non-reversing field, the failure to achieve a 'symmetric rotator' solution, while achieving field geometries for the decentred dipole model with $a = 0.2 - 0.3$, suggested that this model was not valid.

III.2 Harmonic analysis

III.2.1 Deutsch's harmonic analysis

Deutsch, Ledoux & Renson (1966), Bohm-Vitense (1965, 1966, 1967), Preston and others have strengthened the case for the oblique rotator, resulting in its near-universal acceptance. Based upon this model, Deutsch (1958) devised a mapping algorithm with which to investigate the abundance anomalies, and distribution of the magnetic field. The analysis was first applied to HD125248, for which a low resolution map of the stellar surface was obtained. Since then, his technique has been applied by Pypers (1969) to map the surface of $\alpha^2 CVn$ and by many other authors.

The geometry of Deutsch's model is shown in fig (XXXVII) where P_0 is the pole of rotation, with subsolar point S , and angle of inclination between rotational and the line of sight given by χ . At an arbitrary point P on the stellar surface, the polar distance is ψ with azimuth ν , measured from the co-moving meridian, with $\nu = 0$ along the meridian that passes through the sub-solar point at phase $\Phi = 0$.

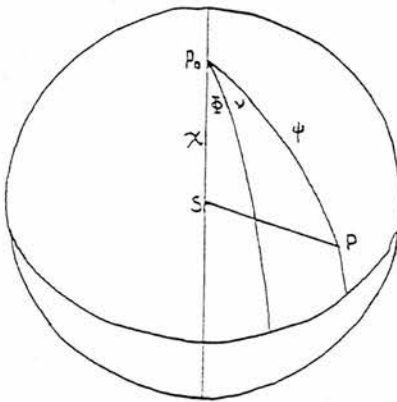


Fig - XXXVII

Let $\xi(\psi, \nu)$ be the distribution function for a given spectral line, emergent

at a point upon the disc, given by the real part of the Laplacian series,

$$\xi(\psi, \nu) = \text{Re}(\Xi(\psi, \nu)) = \sum_{r=0}^{\infty} \sum_{m=-n}^n A_n^m \exp^{im\nu} P_n^{|m|} \cos \theta \quad (3.27)$$

Assuming a linear law of limb darkening,

$$\Lambda = 1 - \mu + \mu \cos \theta \quad (3.28)$$

and analogous line weakening,

$$J = 1 - \kappa + \kappa \cos \theta \quad (3.29)$$

then letting,

$$\Lambda_0 = \int_0^{\frac{\pi}{2}} \int_0^{2\pi} \Lambda \cos \theta \sin \theta d\theta d\phi \quad (3.30)$$

the equivalent-width variation may be written as,

$$\mathcal{W} = \frac{\langle W \rangle}{\Lambda_0} = \text{Re} \left\{ \int_0^{\frac{\pi}{2}} \int_0^{2\pi} \Xi J \Lambda \cos \theta \sin \theta d\phi d\theta \right\} \quad (3.31)$$

It is convenient to express the distribution function $\Xi(\psi, \nu)$ in terms of polar coordinates $\Xi(\theta, \phi)$ which may be completed by the use of the extended addition theorem (Schmidt 1899) for spherical harmonics,

$$e^{im\nu} P_n^{|m|}(\cos \psi) = C_n^m(\theta, \phi, \chi) e^{-im\phi} \quad (3.32)$$

The functions C_n^m may be written, after Sâto (1950) in the form,

$$C_n^m = \sum_{\kappa=0}^n Q_n^{m\kappa} P_n^{\kappa}(\cos \theta) \quad (3.33)$$

where

$$Q_n^{m\kappa} = \begin{cases} (-1)^{\frac{|m|}{2}} [X_n^{m\kappa} \cos \kappa\phi + iY_n^{m\kappa} \sin \kappa\phi] & m=\text{even} \\ (-1)^{\frac{|m|-1}{2}} [-Y_n^{m\kappa} \cos \kappa\phi + iX_n^{m\kappa} \sin \kappa\phi] & m=\text{odd} \end{cases} \quad (3.34)$$

and where $X_n^{m\kappa}, Y_n^{m\kappa}$ are functions of χ . Thus,

$$\Xi(\theta, \phi) = \langle W \rangle \sum_{n=0}^{\infty} \sum_{m=-n}^n B_n^m C_n^m e^{-im\phi} \quad (3.35)$$

and, substituting into eq (3.31),

$$\mathcal{W} = \frac{\langle W \rangle}{\Lambda_0} = \int_0^{\frac{\pi}{2}} \int_0^{2\pi} \langle W \rangle \sum_{n=0}^{\infty} \sum_{m=0}^n B_n^m C_n^m e^{-im\phi} \Lambda \cos \theta \sin \theta d\phi d\theta \quad (3.36)$$

By letting,

$$\begin{aligned} \mathcal{B}_n^m &= \frac{1}{\Lambda_0} \int_0^{\frac{\pi}{2}} \int_0^{2\pi} C_n^m J \Lambda \cos \theta \sin \theta d\phi d\theta \\ D_{-m} &= \sum_{n=m}^{\infty} \mathcal{B}_n^m A_n^m \end{aligned} \quad (3.37)$$

we obtain the fourier series.

$$\mathcal{W} = \langle W \rangle \sum_{m=0}^{\infty} D_{-m} e^{-im\phi} \quad (3.38)$$

\mathcal{B}_n^m may be expanded to

$$\mathcal{B}_n^m = p_n \begin{cases} -1^{\frac{m}{2}} X_n^{m0} & m=\text{even} \\ -1^{\frac{(m+1)}{2}} Y_n^{m0} & m=\text{odd} \end{cases} \quad (3.39)$$

where,

$$p_n = \frac{2\pi}{\Lambda_0} \int_0^{\frac{\pi}{2}} P_n(\cos \theta) J \Lambda \cos \theta \sin \theta d\theta \quad (3.40)$$

Evaluation of the first three terms gives terms totally dependent upon the the limb-darkening and line-weakening coefficients,

$$\begin{aligned} p_0 &= \frac{2\pi}{\Lambda_0} [0.500 - 0.167(\kappa + \mu) + 0.083\kappa\mu] \\ p_1 &= \frac{2\pi}{\Lambda_0} [0.333 - 0.083(\kappa + \mu) + 0.033\kappa\mu] \\ p_2 &= \frac{2\pi}{\Lambda_0} [0.125 + 0.009(\kappa + \mu) - 0.017\kappa\mu] \end{aligned} \quad (3.40a)$$

It is thus found that variation in equivalent width may be approximated by fitting of a straight-forward second-order fourier series. It is also found, that if the curvature in the curve of growth is neglected, this variation suffices to describe all lines of one element.

Though it is now possible, from the coefficients A_n^m , χ , μ , and κ , to describe the variation over phase, the inverse problem of defining the distribution function coefficients from the variation is still undefined. The radial velocity variations may be treated in a similar manner by considering the radial velocity at a point P on the stellar surface,

$$v = V_e \sin \chi \sin \theta \sin \phi \quad (3.41)$$

Weighting the radial velocity by local equivalent width and incorporating the limb darkening leads to,

$$\mathcal{V} = \frac{V_e \sin \chi}{\Lambda_0 \left(\frac{W}{\langle W \rangle} \right)} \int_0^{\frac{\pi}{2}} \int_0^{2\pi} \Xi J \Lambda \cos \theta \sin \theta \sin \phi d\phi d\theta \quad (3.42)$$

and by using Eqs (3.32) in analogy to the equivalent width variations, we may write

$$\begin{aligned} \mathcal{D}_n^m &= \frac{1}{\Lambda_0} \int_0^{\frac{\pi}{2}} \int_0^{2\pi} C_n^m J \Lambda \cos \theta \sin^2 \theta \sin \phi d\phi d\theta \\ E_{-m} &= \sum_{n=m}^{\infty} \mathcal{D}_n^m A_n^m \end{aligned} \quad (3.43)$$

resulting in

$$\left(\frac{W}{\langle W \rangle} \right) \mathcal{V} = (v_e \sin \chi) \sum_{m=0}^{\infty} E_{-m} e^{im\phi} \quad (3.44)$$

This produces a second fourier series where

$$\mathcal{D}_n^m = iq_n \begin{cases} -1^{\frac{m}{2}} Y_n^{m1} & m=\text{even} \\ -1^{\frac{m-1}{2}} X_n^{m1} & m=\text{odd} \end{cases} \quad (3.45)$$

and

$$q_n = \frac{\pi}{\Lambda_0} \int_0^{\frac{\pi}{2}} P'_n(\cos \theta) J \Lambda \cos \theta \sin^2 \theta d\theta \quad (3.46)$$

Again, the first three terms may be evaluated to give

$$\begin{aligned} q_0 &= 0 \\ q_1 &= \frac{\pi}{\Lambda_0} [0.250 - 0.117(\kappa + \mu) + 0.067\kappa\mu] \\ q_2 &= \frac{\pi}{\Lambda_0} [0.400 - 0.115(\kappa + \mu) + 0.070\kappa\mu] \end{aligned} \quad (3.47)$$

It now only remains to describe the variation of magnetic field which Deutsch computes on the assumption that the magnetic field is irrotational (Cowling 1952). By considering the field in similar manner the fourier series,

$$\frac{W}{\langle W \rangle} \mathcal{H}_e = \sum_{r=-\infty}^{\infty} \mathcal{G}_r e^{ir\phi} \quad (3.48)$$

may be constructed, where

$$\mathcal{G}_r = \frac{1}{4\pi} \int_0^{2\pi} \sum M_n^m \mathcal{K} \left[A_\alpha^\beta (\mathcal{F} - \mathcal{J}) e^{-i\beta\phi} + A_\alpha^{\beta*} (\mathcal{F} + \mathcal{J}) e^{i\beta\phi} \right] e^{-i(m+r)\phi} d\phi \quad (3.49)$$

The three fourier series, (Eq. 3.38, 3.44, 3.48) may be expanded, ignoring terms of second degree or higher. This simplification is justified by Deutsch in that any higher order terms would cause deformation of the line profiles to an extent

where deformation may be recognised and analysis not performed.

$$\begin{aligned}
 \frac{W}{\langle W \rangle} &= 1 + d_{-1} \cos \phi + \delta_{-1} \sin \phi + d_{-2} \cos 2\phi + \delta_{-2} \sin 2\phi \\
 v \left(\frac{W}{\langle W \rangle} \right) &= (v_e \sin \chi) [e_{-1} \cos \phi + \varepsilon_{-1} \sin \phi + e_{-2} \cos 2\phi + \varepsilon_{-2} \sin 2\phi] \\
 H_e \left(\frac{W}{\langle W \rangle} \right) &= g_0 + (g_{-1} + g_1) \cos \phi + (\eta_{-1} - \eta_1) \sin \phi \\
 &\quad + (g_{-2} + g_2) \cos 2\phi + (\eta_{-2} - \eta_2) \sin 2\phi
 \end{aligned} \tag{3.50}$$

Fitting the fourier series to the equivalent width, radial velocity and magnetic field variations by a least-squares method then enables calculation of the coefficients in Eq (3.50) and, subsequently, 14 equations may be written down from the expansion of the fourier series (Eq. (3.50), with appropriate values of the limb darkening and line weakening coefficients κ, μ . Deutsch calculates the relevant constants for HD125248 to be,

$$\mu = 0.62 \quad \kappa = 0.16 \quad \frac{\Lambda_0}{\pi} = 0.793 \tag{3.51}$$

creating the equations,

$$d_0 = 0.948a_0^0 + 0.680a_1^0 \cos \chi + 0.082a_2^0(1 + 3 \cos 2\chi) = 1 \tag{3.52}$$

$$d_{-1} = 0.680a_1^1 \sin \chi + 0.492a_2^1 \sin 2\chi \tag{3.53}$$

$$\delta_{-1} = 0.680\alpha_1^1 \sin \chi + 0.492\alpha_2^1 \sin 2\chi \tag{3.54}$$

$$d_{-2} = 0.984a_2^2 \sin^2 \chi \tag{3.55}$$

$$\delta_{-2} = 0.984\alpha_2^2 \sin^2 \chi \tag{3.56}$$

$$e_0 = 0 \tag{3.57}$$

$$e_{-1} = -0.207\alpha_1^1 - 0.363\alpha_2^1 \cos \chi \tag{3.58}$$

$$\varepsilon_{-1} = 0.207a_1^1 + 0.363a_2^1 \cos \chi \tag{3.59}$$

$$e_{-2} = -0.726\alpha_2^2 \sin \chi \quad (3.60)$$

$$\varepsilon_{-2} = 0.726a_2^2 \sin \chi \quad (3.61)$$

$$\begin{aligned} g_0 &= 0.656a_0^0(m_1^0 \cos \chi) + (0.640 + 0.363 \tan^2 \chi)(a_1^0 \cos \chi)(m_1^0 \cos \chi) \\ &\quad + (0.502 + 0.364 \cot^2 \chi) [(a_1^1 \sin \chi)9m_1^1 \sin \chi) + (\alpha_1^1 \sin \chi)(\mu_1^1 \sin \chi)] \\ &\quad + 0.030a_0^0m_2^0(1 + 3 \cos 2\chi) \end{aligned} \quad (3.62)$$

$$\begin{aligned} g_{-1} + g_1 &= 0.656a_0^0(m_1^1 \sin \chi) + 0.277(a_1^0 \cos \chi)(m_1^1 \sin \chi) \\ &\quad + 0.277(a_1^1 \sin \chi)(m_1^0 \cos \chi) + 0.177a_0^0m_2^1 \sin 2\chi \end{aligned} \quad (3.63)$$

$$\begin{aligned} \eta_{-1} + \eta_1 &= 0.656a_0^0(\mu_1^1 \sin \chi) + 0.277(a_1^0 \cos \chi)(\mu_1^1 \sin \chi) \\ &\quad + 0.277(\alpha_1^1 \sin \chi)(m_1^0 \cos \chi) + 0.177a_0^0\mu_2^1 \sin 2\chi \end{aligned} \quad (3.64)$$

$$\begin{aligned} g_{-2} + g_2 &= 0.138 [(a_1^1 \sin \chi)(m_1^1 \sin \chi) - (\alpha_1^1 \sin \chi)(\mu_1^1 \sin \chi)] \\ &\quad + 0.354a_0^0m_2^2 \sin^2 \chi \end{aligned} \quad (3.65)$$

$$\begin{aligned} \eta_{-2} + \eta_2 &= 0.138 [(a_1^1 \sin \chi)(\mu_1^1 \sin \chi) + (\alpha_1^1 \sin \chi)(m_1^1 \sin \chi)] \\ &\quad + 0.354a_0^0\mu_2^2 \sin^2 \chi \end{aligned} \quad (3.66)$$

Having obtained the 17 fourier terms, the values of the Laplace co-efficients

$$a_0^0, a_1^0, \alpha_1^1, a_2^0, a_2^1, \alpha_2^1, a_2^2, \alpha_2^2$$

$$m_1^0, m_1^1, \mu_1^1, m_2^0, m_2^1, \mu_2^1, m_2^2, \mu_2^2$$

χ

may be solved for.

From Eq's (3.55, 3.56, 3.60, 3.61) the value of v_e may be obtained allowing the solving of Eq's (3.53, 3.54, 3.58, 3.59) to give,

$$a_1^1 \sin \chi \quad \alpha_1^1 \sin \chi \quad a_2^1 \sin 2\chi \quad \alpha_2^1 \sin 2\chi$$

This still requires the evaluation of eleven unknowns from only 6 equations.

Deutsch circumnavigates this problem by noting that nine of the unknowns,

the magnetic field Laplace coefficients, will be invariant regardless of abundance differences between elements. Thus by subjecting three groups of elements, each displaying distinct variations, fifteen equations may be created with the addition of only four unknowns: a_0^0, a_1^0 for each elemental group. Qualitatively, the inclusion of three groups enables the magnetic field parameters to be obtained by considering a greater portion of the stellar surface. With three distinct elemental distribution functions, a greater portion of the surface of the star is covered by measurements of the magnetic field, enabling the obtainment of a greater number of unknowns.

It is thus essential to be able to define at least three distinct variations within the elements considered. Deutsch found that Eu-II, Gd-II, Ce-II all display similar variations, while being distinct from two other groups comprised of Cr-I, Cr-II, Sr-II, and Fe-I, Fe-II, Ti-II respectively.

It is now possible to solve the fifteen unknowns from the fifteen non-linear equations by standard linearization of the equations. This will create a set of fifteen linear equations that may be solved by an iterative process. The mapping may then be performed by substitution of the Laplace coefficients into,

$$\begin{aligned} \frac{\xi}{\langle W \rangle} &= a_0^0 + a_1^0 \cos \psi + (a_1^1 \cos \nu - \alpha_1^1 \sin \nu) \sin \psi \\ &+ \frac{1}{4} a_2^0 (3 \cos 2\psi + 1) + \frac{3}{2} (a_2^1 \cos \nu - \alpha_2^1 \sin \nu) \sin 2\psi \\ &+ \frac{3}{2} (a_2^2 \cos 2\nu - \alpha_2^2 \sin 2\nu) (1 - \cos 2\psi) \end{aligned} \quad (3.67)$$

$$\begin{aligned} \mathcal{S} &= R \left\{ \left(\frac{R}{r} \right)^2 [m_1^0 \cos \psi + (m_1^1 \cos \nu - \mu_1^1 \sin \nu) \sin \psi] \right. \\ &\left. + \left(\frac{R}{r} \right)^3 \left[\frac{1}{4} m_2^0 (3 \cos 2\psi + 1) + \frac{3}{2} (m_2^1 \cos \nu - \mu_2^1 \sin \nu) \sin 2\psi \right] \right\} \end{aligned}$$

$$+ \frac{3}{2}(m_2^2 \cos 2\nu - \mu_2^2 \sin 2\nu)(1 - \cos 2\psi) \Big] \Big\} \quad (3.68)$$

for the stellar co-ordinate values ψ , and ν .

Though this process produces elemental distributions and depicts the position and strength of the magnetic poles, its usefulness is limited by the criteria required for its application, namely the necessity to observe three distinct variation groups, and sufficient phase coverage and data to enable a unique solution to be attained from the fourier series fitting. Incomplete phase coverage will not only mask the stellar aspect at the considered phase, but uncertainty will be introduced into neighbouring phases, dependent upon the limb darkening law, as observations are the result of integration over the visible disc.

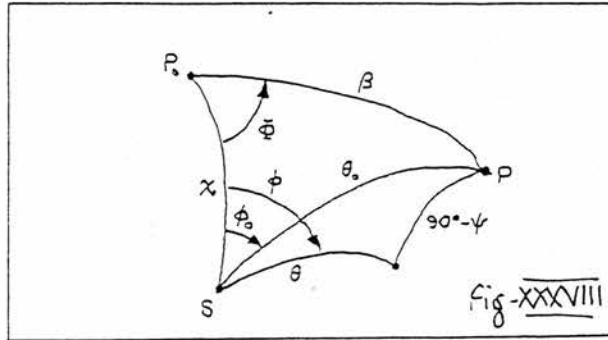
III.2.2. Mihalas' analysis

Though intrinsically simpler than Deutsch's analysis, the harmonic method proposed by Mihalas (1973) to investigate helium abundances in 56 Ari, may be used to gain considerable insight into the surface geometry of the star. Whereas Deutsch's method produces cartographic detail of the stellar surface, Mihalas' approach attempts to define an axis of abundance symmetry. This limitation considerably simplifies the harmonic analysis while, by computing the rotational to symmetric axis angle β , and attaining the rotational to line-of-sight inclination χ , still producing effective results. The attainment of these two angles then allows further substitution into the oblique rotator models to compare with experimental results. It is assumed that the axis of symmetry found by this method coincides with the axis of primary symmetry of the magnetic field distribution.

The analysis is also better suited to stars with non-ideal data sets. Mihalas applies it to 56 Ari, which exhibits particularly large noise, and, while

the solution is probably not unique, a two-cap model for the observed helium abundance is created. As such, a data set failing to satisfy the criteria for Deutsch's analysis may still reveal significant information under this approach.

The formalism of Mihalas' model is similar to Deutsch's, though with simplified geometry depicted in fig (XXXVIII).



To avoid confusion, the limb darkening and line weakening functions used by Deutsch will be carried forward to this analysis, though Mihalas defines them by different means.

Assuming the equivalent width distribution may be written as,

$$\Xi(\cos \psi) = \sum a_n P_n(\cos \psi) \quad (3.68)$$

and letting $\langle W \rangle \Xi$ describe the surface distribution. Then by using the standard addition theorem,

$$P_n(\cos \psi) = \sum_{m=0}^n \epsilon_m \frac{(n-m)!}{(n+m)!} P_n^m(\cos \theta) P_n^m(\cos \theta_0) \cos [m(\phi - \phi_0)] \quad (3.69)$$

upon,

$$\frac{W(\Phi)}{\langle W \rangle} = \int_0^{2\pi} \int_0^{\frac{\pi}{2}} \Lambda(\theta) J(\theta) \Xi(\theta, \phi) \cos \theta \sin \theta d\theta d\phi \quad (3.70)$$

and substituting Eq (3.68) into (3.70) along with subsequent integration and expression of (θ_0, ϕ_0) in terms (χ, β, ϕ) gives,

$$\frac{W(\Phi)}{\langle W \rangle} = A_0 + A_1 \cos \Phi + A_2 - 2 \cos 2\Phi \quad (3.71)$$

where,

$$\begin{aligned} A_0 &= a_0 p_0 + a_1 p_1 \cos \chi \cos \beta + a_2 p_2 \left[\frac{3}{2} (\cos^2 \chi \cos^2 \beta + \frac{1}{2} \sin^2 \chi \sin^2 \beta) - \frac{1}{2} \right] \\ A_1 &= a_1 p_1 \sin \chi \sin \beta + \frac{3}{4} a_2 p_2 \sin 2\chi \sin 2\beta \\ A_2 &= \frac{3}{4} a_2 p_2 \sin^2 \chi \sin^2 \beta \end{aligned} \quad (3.72)$$

The limb-darkening coefficients p_0, p_1, p_2 correspond to the equivalent parameters in Deutsch's analysis. By least-squares fitting it is then possible to obtain $A_{0,1,2}$ though, since there are five basic unknowns, without prior knowledge of two, the solution is indeterminate.

The rotational velocity variations may be written similarly to Deutsch as,

$$v \left(\frac{W}{\langle W \rangle} \right) = v_e \sin \chi \int_0^{2\pi} \int_0^{\frac{\pi}{2}} \Lambda(\theta) j(\theta) \Xi(\theta, \phi) \cos \theta \sin^2 \theta d\theta d\phi$$

which, assuming only first or second order variations may then be reduced to,

$$v \left(\frac{W}{\langle W \rangle} \right) = (v_e \sin \chi) (B_1 \sin \phi + B_2 \sin 2\phi) \quad (3.74)$$

where,

$$\begin{aligned} B_1 &= a_1 q_1 \sin \beta + \frac{\sqrt{3}}{2} a_2 q_2 \cos \chi \sin^2 \beta \\ B_2 &= \frac{\sqrt{3}}{2} a_2 q_2 \sin \chi \sin^2 \beta \end{aligned} \quad (3.75)$$

and q_1, q_2 are as in Deutsch's analysis. These five non-linear equations now enabling $a_0, a_1, a_2, \chi, \beta$ to be explicitly determined.

Though this set may be solved by linearization and subsequent iteration, a simpler method may be completed. By evaluating a_0, a_1, a_2 for a range of χ, β , from Eq. (3.75), many possible solutions of χ, β may be eliminated since by their adoption, negative distribution functions occur. Expanding the Laplace series to second order, the requirement for acceptance of a given χ, β may be seen to be,

$$a_0 + a_1 \cos \psi + a_2 \left[\frac{3}{2}(\cos^2 \psi) - \frac{1}{2} \right] > 0 \quad (3.76)$$

for all values of ψ . The remaining 'solutions' of χ, β and respective a_0, a_1, a_2 may then be substituted into Eq (3.74) to create theoretical radial velocity variations with which to compare the observed variations.

A range of χ, β will then be observed, within which $\Xi(\psi) > 0$. These solutions will be either symmetric ($a_1 = 0$) with reflection in the magnetic equator, or antisymmetric, implying non-equal polar abundance. By choosing suitable symmetric solutions, it is possible to obtain relatively accurate values for χ, β .

III.2.3 Application of Mihalas' harmonic analysis

The application of harmonic analysis to HD49976 is limited, since a large proportion of the cycle is uncovered by data, particularly the phase at which negative maximum is expected to occur. In these circumstances, fitting of Deutsch's five-term fourier series is thought to be unjustified. Additionally, though titanium may show distinct variations from the remaining elements, the measurements of elemental magnetic field, radial velocity, and equivalent width for the elements studied do not allow the definition of three elemental groups. This requirement, central to the use of Deutsch's algorithm, is not satisfied in the case of HD49976 with the present data, and a simplified approach must be made.

III.2.3.1 A Model atmosphere

The first step in the calculation of μ, κ is to define an effective temperature for HD49976. According to Morton & Adams (1968), an effective temperature of 9600 K is appropriate for a star of MK classification A0 with $\log(g) = 4.0$. Olson (1974) supplies calibration of $(b - y)$ photometric observations to T_e , providing a second mechanism for determination of T_e . Since light variations occur, and extensive line blanketing is suggested by Pilachowski et al, the appropriate value of $(b - y)$ must be taken from Pilachowski's data, when line blanketing is expected at a minimum. Sr-II equivalent width shows a minimum at phase 0.90, corresponding to a value of $(b - y) = -0.006$. Assuming a value of $\log(g) = 4.0$, this implies an effective temperature of 9750 K.

Shallis & Blackwell (1979) state that the observed colours may not accurately define the effective temperature. Comparison of T_e for $\alpha^2 CVn$ and $\gamma Equulei$ by conventional colours and the infra-red flux method proposed, suggest that the $(b - y)$ colour measurement may over-estimate the effective tem-

perature. In the case of $\alpha^2 CVn$, this overestimate may be as great as 1000 K, whereas for $\gamma Equulei$, the overestimate ranges from 100 - 500 K. Theoretical considerations for a cooler effective temperature is provided by Hubbard & Dearborn (1982). They propose that the moderate magnetic field seen in Ap stars may be sufficient to expand the outer 10^{-8} of the mass of a $2M_o$ star, increasing the radius by 20%. This expansion, would create a general reddening of the outer stellar envelope providing an alternative explanation for the UV line blanketing for depressed flux measurements in the blue region. The increase in radius, more dramatic in stars of $M_o = 3.0$, would then result in inaccurate T_e , which is determined from line blanketing compensated data.

From these considerations, a temperature of 9500 K will be assigned to HD49976, from Olson et al, allowing for a small decrease in temperature, from enlarged-radius reddening.

Chandrasekhar (1950) shows that the limb darkening in the continuum may be written as,

$$\Lambda = \frac{I(0, \cos \theta)}{I(0, 1)} = \frac{\mathcal{F}\left(\frac{h\nu}{kT_e}, \frac{\kappa\nu}{\langle \kappa \rangle \cos \theta}\right)}{\mathcal{F}\left(\frac{h\nu}{kT_e}, \frac{\kappa\nu}{\langle \kappa \rangle}\right)} \quad (3.77)$$

and has tabulated the function \mathcal{F} . Using $T_e = 9500$, and an electron pressure of 10^4 cgs, the results of Chandrasekhar & Munch (1946) indicate that

$$\frac{\kappa\nu}{\langle \kappa \rangle} \simeq 0.4 \quad \text{at} \quad 4000A^0 \quad (3.78)$$

By interpolation from Chandrasekhar's results, the value of Λ may be acquired as,

$$\Lambda = \frac{\mathcal{F}(3.68, \frac{0.4}{\cos \theta})}{\mathcal{F}(3.68, 0.4)} \simeq 0.506 \cos \theta + 0.579 \quad (3.79)$$

We thus adopt $\mu = 0.506$ and $\frac{\Lambda_0}{\pi} = 1 - \frac{1}{3}\mu = 0.847$. The coefficient of line weakening may be evaluated from Wrubel's (1949, 1950) curves of growth for

a Milne-Eddington atmosphere. Expanding the Planck function as a Taylor series in τ , the optical depth in the continuum,

$$B(\nu, \tau) = a_\nu + b_\nu \tau \quad (3.80)$$

and assuming $T_e = 9500$, $\frac{\kappa}{\langle \kappa \rangle} = 0.4$, then in Wrubel's notation,

$$\frac{B^{(0)}}{B^{(1)}} = \frac{1}{3} \quad (3.81)$$

Using the value of $\frac{B^{(0)}}{B^{(1)}}$, and the value $\log(a) = -2.20$, where a is the ratio of thermal to doppler width, we can calculate the mean ratio of the equivalent width at centre of the disk W_0 , to that in the flux W_F , as $\frac{W_0}{W_F}$. Then, by taking a mean value of $\log \frac{W_0}{W_F}$ from Wrubel's tables against ν we get a value of

$$\frac{W_0}{W_F} = 1.06$$

Now, writing

$$W_F = \frac{2\pi}{\Lambda_0} \int_0^{2\pi} W_0 J \Lambda \cos \theta \sin \theta d\theta = \frac{1}{1.06}$$

we find that after substitution in Eq(3.28, 3.29) that,

$$\kappa = 1 - \frac{1}{2 - \mu} \left[\frac{2(3 - \mu)}{1.06} - (4 - \mu) \right] \quad (3.82)$$

giving $\kappa = 0.19$ for $\mu = 0.506$. Substituting into the Eqs (3.40a,3.47) with these values gives,

$$p_0 = 0.92 \quad p_1 = 0.65 \quad p_2 = 0.306$$

and

$$q_0 = 0 \quad q_1 = 0.206 \quad q_2 = 0.385$$

We may now apply these coefficients into Eq. (3.72, 3.75).

III.2.3.2 Calculation of co-efficients

A least-squares fit to the equivalent width data (fig XXXIX) depicts a symmetric variation around phase 0.50 for the elements of Cr-I, Cr-II, Ti-II, and Fe-II. The Legendre polynomials are then calculated for each element, with values of χ, β ranging from $0-90^\circ$. On obtaining the legendre polynomial coefficients the distribution function may be evaluated for values of ψ , the colatitude ranging from $0-180^\circ$. A locus of solutions in the χ, β plane is then obtained, fig (XL) from the criterion, that Ξ be non-negative at all colatitudes. Fe-I is found to have no solutions of a non-negative distribution function at this point. Since the equivalent width variations are small and the measurements are diverse, it is thus assumed that no axis of symmetry may be defined for this element and, pending further data, its distribution is effectively uniform.

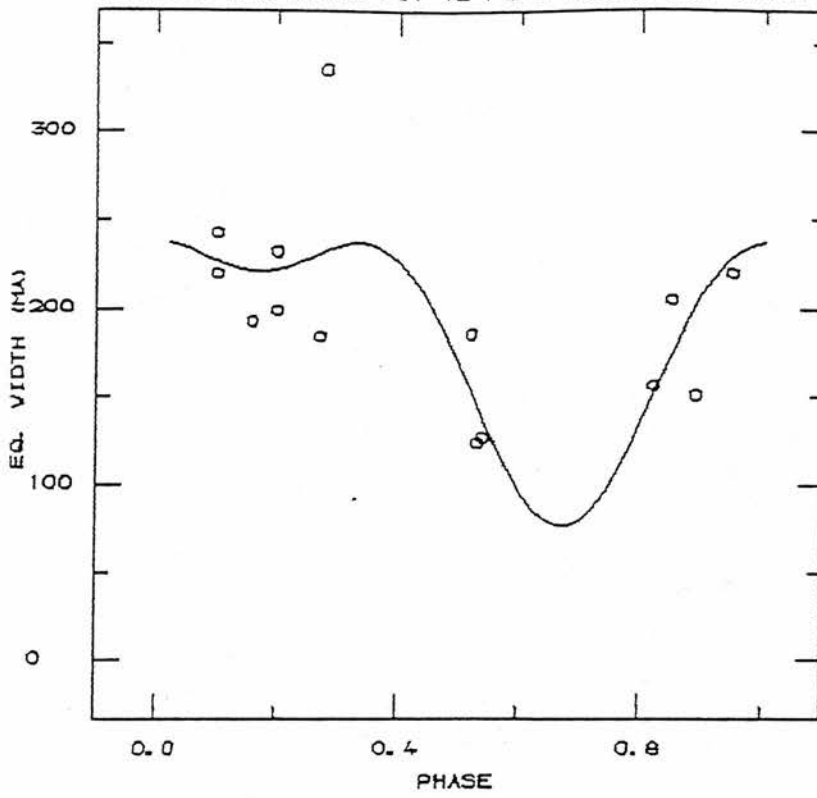
By application of the restriction that a symmetric solution must occur, it is then possible to limit the number of solutions to,

Element	Values of χ, β		
Fe-I			
Fe-II	50/75	60/70	65/65
Cr-I	65/70		
Cr-II			
Ti-II			

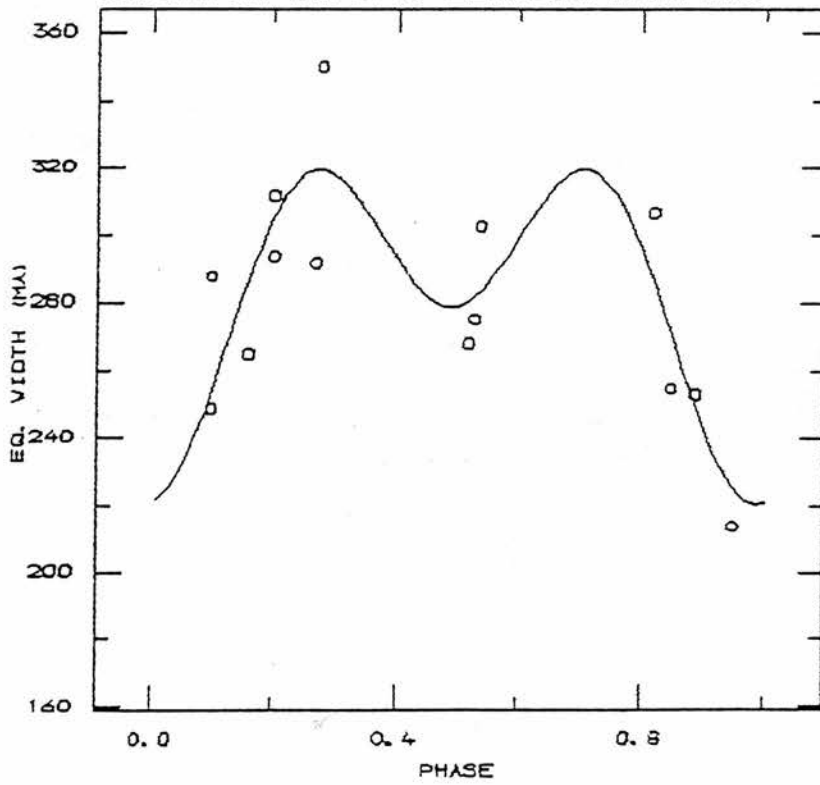
Although no symmetric solutions do exist for Cr-II, Ti-II, antisymmetric solutions do exist as seen in figure (XL). All solutions show comparatively large values of the inclination of rotational axis to line of sight, and in order to satisfy $\Xi > 0$ for all elements, $\chi > 70^\circ$.

By substituting the legendre coefficients into Eq.(3.75), and using values

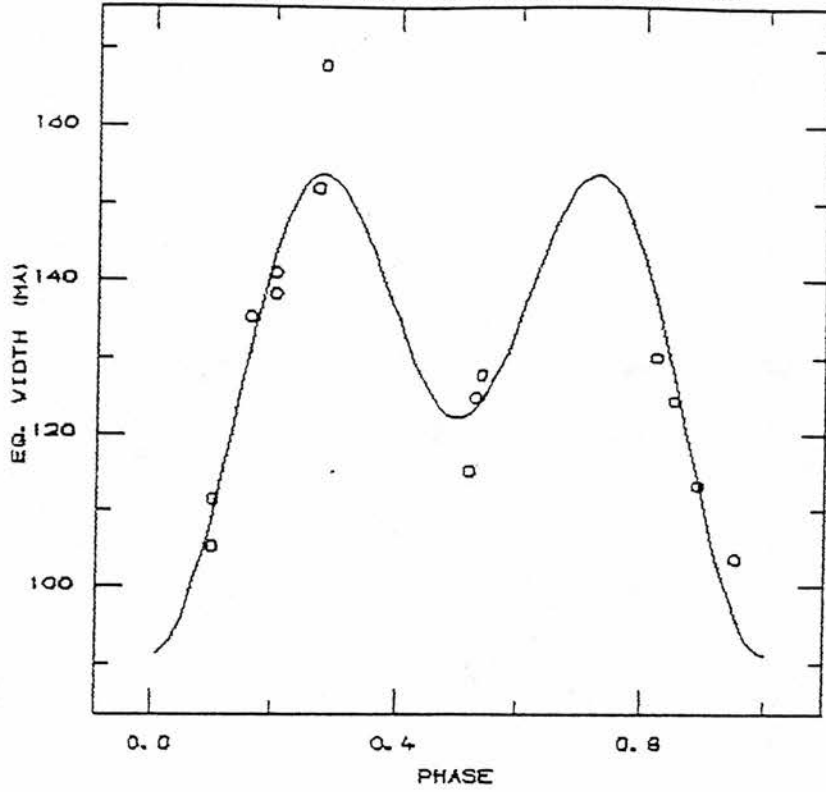
COMPUTED 2ND ORDER FIT TO Fe-I EQUIVALENT WIDTH



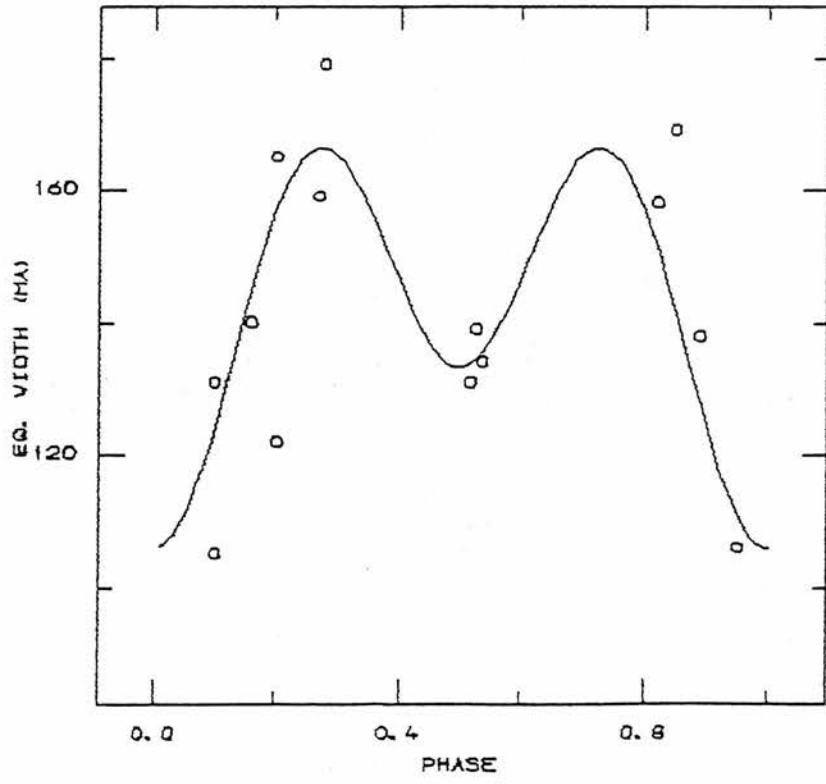
COMPUTED FIT FOR Fe-II EQUIVALENT WIDTH VAR.



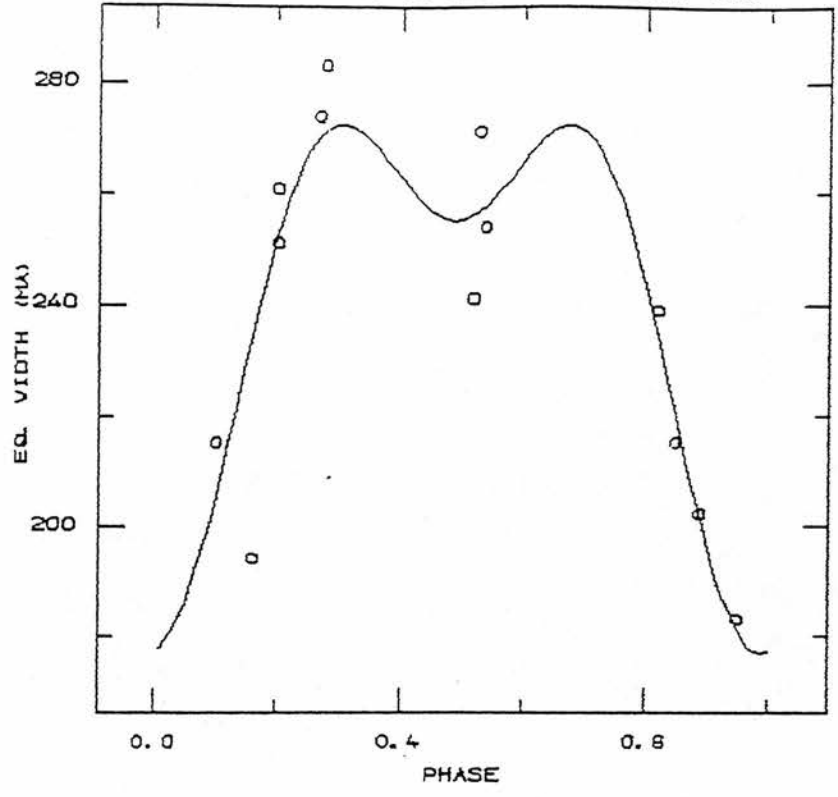
COMPUTED FIT FOR CR-I EQUIVALENT WIDTH VAR.



COMPUTED FIT FOR CR-II EQUIVALENT WIDTH VAR.

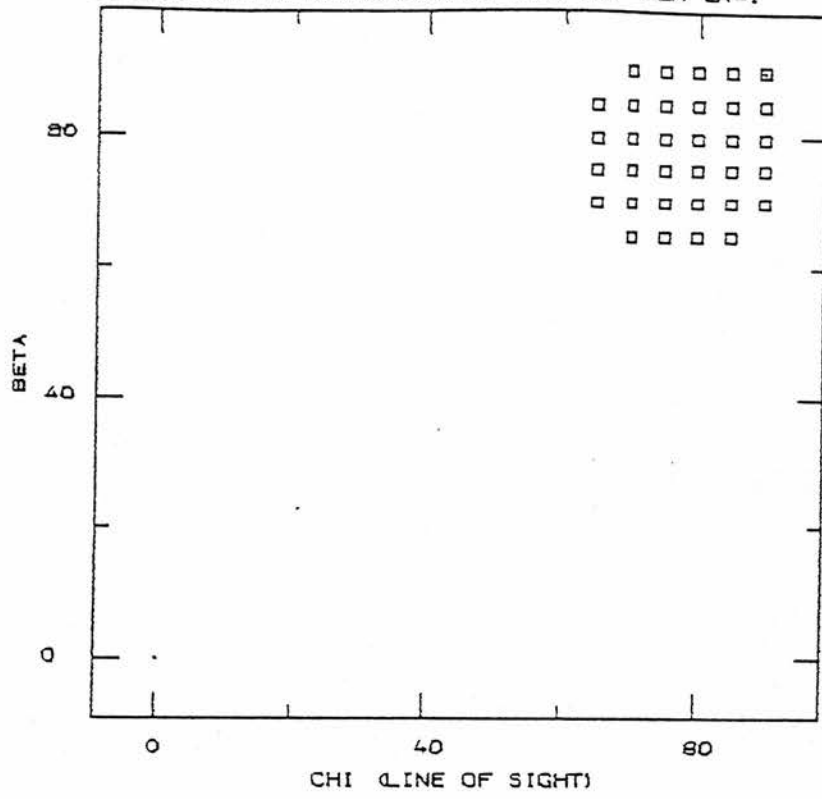


COMPUTED FIT FOR TI-II EQUIVALENT WIDTH VAR.

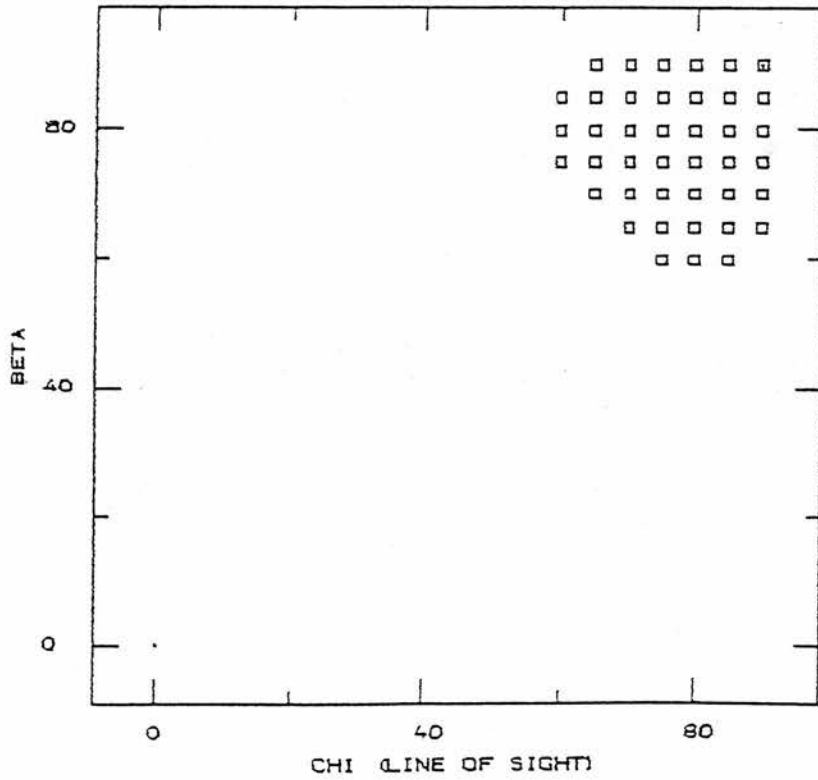


SOLUTIONS FOR NON-NEGATIVE DIST. FN. FOR CR-I

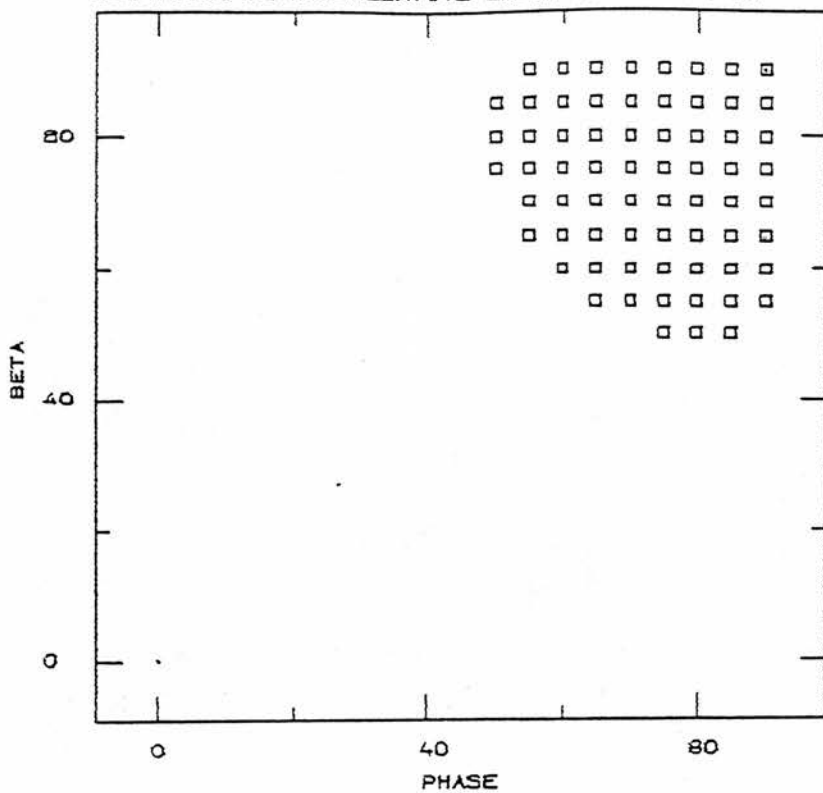
Fig - XL



SOLUTIONS FOR NON-NEGATIVE DIST. FN. FOR CR-II



SOLUTIONS TO NON-NEGATIVE DIST. FN FOR FE-II



SOLUTIONS OF NON-NEGATIVE DIST. FN. FOR TI-II

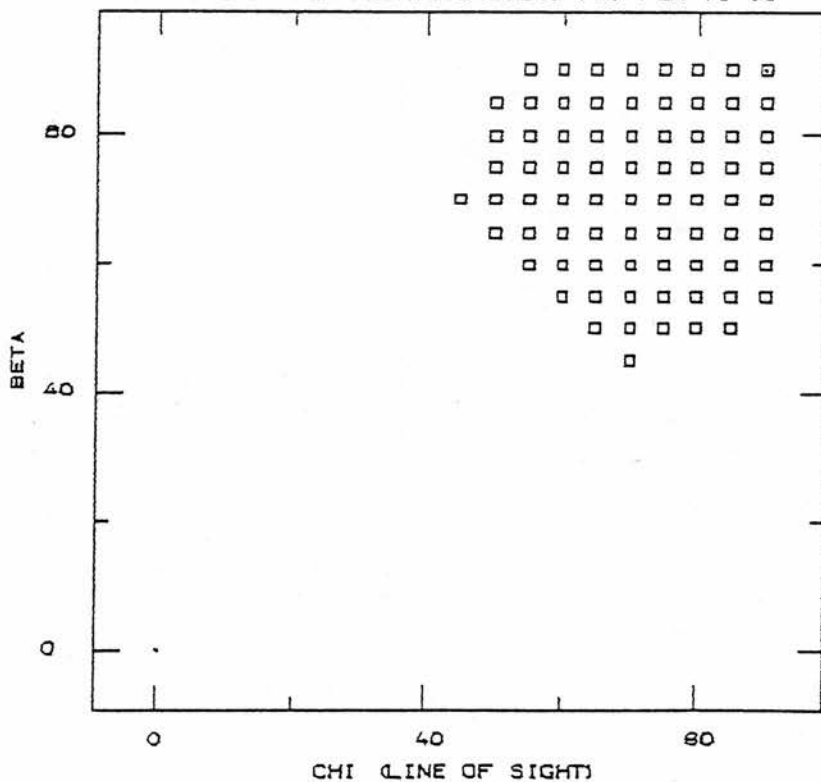
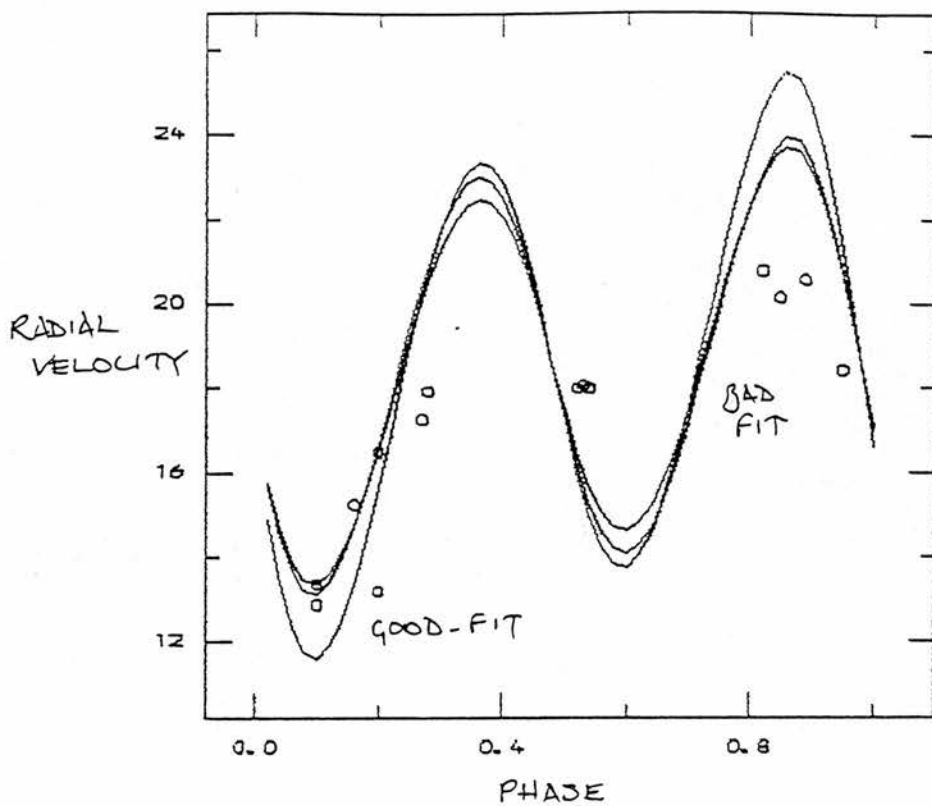


Fig -XLI



of χ, β appropriate to each solution, the values of χ, β may be found from those that give the best fit to the observed radial velocity variations.

Comparison of such solutions (fig (XLI)) shows that though the theoretical curve fits the radial velocity variations at phase 0.00 – 0.20, it does not mirror the data at phases 0.80 – 0.95. Substitution of non-symmetric solutions likewise results in a non-identical fit of the predicted radial velocity variation to that of the observed variation, at phases > 0.60 . Given the speculative nature of the data between phase 0.50 – 0.80, the least-squares fit computed from the equivalent widths may not follow the unobserved data at this point in the cycle. A purported value of $\chi > 70^\circ$ is also incompatible with the value of $v \sin \chi = 31 \text{ km.s}^{-1}$ as observed by Pilachowski et al.

Preston (1972) indicates that the equatorial velocity may be found from the relation

$$V_e = \frac{50.6(\frac{R}{R_o})}{\tau} \quad (3.84)$$

where τ is the rotational period in days. In order to satisfy $v \sin \chi = 31 \text{ km.s}^{-1}$ and $\chi > 70^\circ$, then $V_e < 33 \text{ km.s}^{-1}$. This would imply a stellar radius of $1.92R_o$, which is uncharacteristically small for an A0 star. Values of average stellar radii deduced by Preston (1970) and Winzer (1974) indicate that a radius of between $R_* = 3.2R_o$ and $R_* = 2.2R_o$ would be more appropriate. Shallis & Blackwell (1979) report values of R_* for Ap stars by means of infra-red photometric measurements and parallax from Woolley et al (1970). They indicate that Ap stars may have considerably greater radii than previously expected (fig (XLII)). Comparison of their results for ϵUMa and $\alpha^2 CVn$ and those of Stift (1974) indicate that the A0p stars may have radii approaching $4R_o$, an increase of 31% over radii determined by previous measurements. Hubbard & Dearborn suggest, as mentioned previously, that this is due to horizontal flux tubes either diffusing or rising from magnetic buoyancy, carrying the ionized

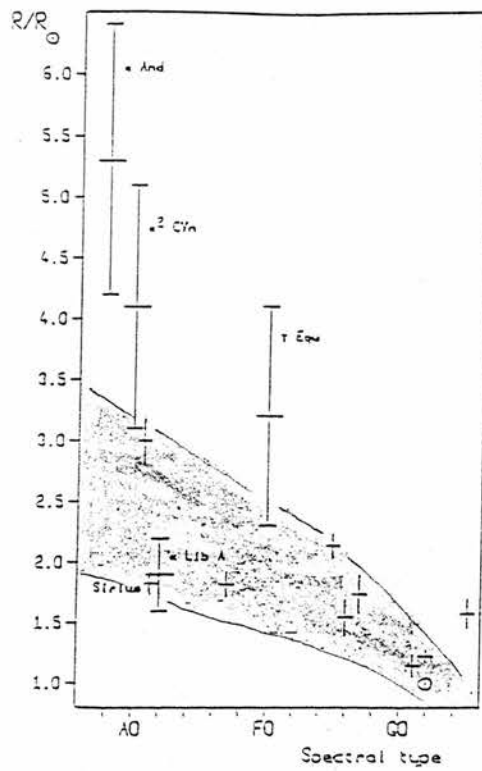


Fig - XLII

Radius plotted against spectral type from the data in Table 4, together with the radii of main sequence stars from Blackwell and Shailis (1977) and Blackwell et al. (1979). The shaded area is fitted to the band within which the main sequence stars are found. Error bars combine the uncertainties in both the angular diameters and the parallax values. For the A₀ stars the uncertainty is mainly due to the parallax measures, for the comparison stars it is chiefly in the θ values

elements outwards.

These ambiguities, coupled to the inaccurate fitting of the radial velocity variations, suggest that the available equivalent-width data is not sufficiently well-determined.

Measurements of Sr-II conducted by Maitzen & Albrecht (1975) indicate that the equivalent width data, should provide an asymmetric equivalent-width profile (fig XLIII). Their results indicate, as do those of Pilachowski et al, the existence of a low secondary peak. This variation, compatible with the few data points observed, may result in a more consistent solution.

Using the results supplied by Maitzen & Albrecht, the analysis may be reconducted. However, the observed variation in Sr-II strongly suggests a non-central axis of symmetry. As can be seen from (Fig. XLIII), the secondary

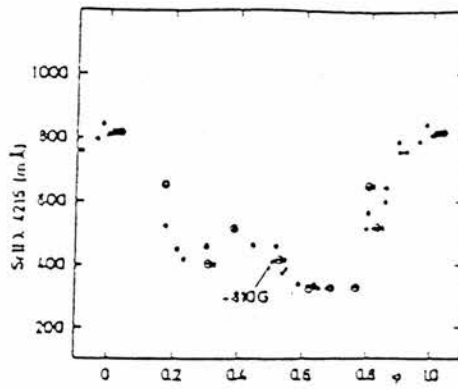


Fig - XLIII

peak is not observed to be separated by $\frac{\pi}{2}$ from the other two. On fitting the second-order fourier cosine series, the best fit is found to be unable to mirror the data. Evaluation of possible solutions, despite the inadequacy of the initial fit, reveals that solutions may now be obtained to a non-negative distribution function for values of $\chi > 35^\circ$. This would produce $R_* < 3.2R_\odot$ from eq (3.84), more compatible with observed radii.

Although a near-symmetry is obtained for values of $\chi = 35^\circ, \beta = 80^\circ$, the calculated radial-velocity variation still does not mirror the observed data. This is thought to be due to the non-ideal fit computed from the equivalent-width variations. This apparent solution at $\chi = 35^\circ, \beta = 80^\circ$, may not be relied upon since the suggestion of a non-central axis of symmetry invalidates the use of Mihalas' analysis. Additionally, considering the plethora of possible non-symmetric solutions, the criterion of symmetry is open to question.

III.2.3.3 Restrictions of Mihalas' analysis

The analysis is formulated to deduce an axis of symmetry coincident with the stellar centre. If, as suggested by Maitzen & Albrecht and the non-harmonic variations in magnetic field, the axis does not fulfil this criterion, the process, and analysis immediately becomes erroneous. Thus, although simpler than Deutsch's analysis, it is seen that Mihalas' simplification results in severe constraints upon the calculated model which, as in this case, may not be satisfied.

It is thus concluded that within the restrictive framework of Mihalas' model, it is impossible to obtain a plane of symmetry coincident with the stellar centre.

III.3 Statistical evaluation of magnetic axis inclination

III.3.1 Theoretical considerations

By second-order harmonic fitting of the magnetic field variations of HD49976 (Figure (XXVII)), it is seen, that $r = 0.98$. To investigate whether this value is compatible with the hypothesis of the oblique rotator model, and other values of r for known periodic magnetic variables, it is possible to statistically analyze the distribution of r . Since the index r is composed of the values of i, β , where the angle between the rotational axis and the line-of-sight in Stibbs' notation is i , this will yield information upon the distribution of the angles i, β .

If i and β define the directions that are randomly distributed, their probability distribution may be written as

$$f_i = \sin i \quad f_\beta = \sin \beta \quad (3.85)$$

and, assuming that the two distributions are independent, the function

$$f(i, \beta) = f_i(i)f_\beta(\beta) = \sin i \sin \beta \quad (3.86)$$

gives the bivariate frequency distribution for the combined functions in Eq (3.85). From the geometry of the oblique rotator, and the definition of the magnetic ratio r given by Eq. (3.12), we have

$$\tan i = \frac{1-r}{1+r} \cot \beta \quad (3.87)$$

from which it follows that

$$\frac{di}{dr} = -\frac{2 \cot \beta}{(1+r)} \sec^2 i \quad (3.88)$$

Changing the variable from i to r gives

$$f_r(r|\beta) = f_i(i) \left| \frac{di}{dr} \right| \quad (3.89)$$

where the modulus $|\frac{di}{dr}|$ is required since the probability must necessarily be positive. The probability density of r for a given β is then

$$f_r(r|\beta) = \frac{2(1-r)\tan\beta}{\{(1-r)^2 + (1+r)^2 \tan^2\beta\}^{\frac{3}{2}}} \quad (3.90)$$

and the joint probability $g(r, \beta)$ is defined in terms of the marginal probability (Eq. 3.89) by the relation

$$g(r, \beta) = f_r(r|\beta)f_\beta(\beta) \quad (3.91)$$

The measured probability density of r is then obtained as

$$\begin{aligned} f_r(r) &= \int_0^{\frac{\pi}{2}} g(r, \beta) d\beta \\ &= \frac{\pi}{8} \frac{1-r}{(1+r)^3} F\left[\frac{3}{2}; \frac{3}{2}; 3; \frac{4r}{(1+r)^2}\right] \end{aligned} \quad (3.92)$$

where $F[\alpha; \beta; \gamma; t]$ is the hypergeometric function with parameters α, β, γ for the variable $t = \frac{4r}{(1+r)^2}$. Since

$$\frac{d}{dt} F[\alpha; \beta; \gamma; t] = \frac{\alpha\beta}{\gamma} F[\alpha+1; \beta+1; \gamma+1; t] \quad (3.93)$$

the cumulative probability of r is

$$P_r(r) = \int_{-1}^r f_r(r) dr = \frac{\pi}{4} F\left[\frac{1}{2}; \frac{1}{2}; 2; \frac{4r}{(1+r)^2}\right] \quad (3.94)$$

This result, due to Stibbs and Carson (1987), gives the expected cumulative probability density which may then be compared with the observed distribution of r -values to test the hypothesis of the random distribution of the inclination of the magnetic axis relative to the axis of rotation.

Following a suggestion by Preston (1971) implied by Eq.(3.86), that the paucity of r -values between $-0.25 - 0.00$ and $0.50 - 0.70$ indicated that two groups of oblique rotator exist with $\beta \simeq 20^\circ$ and $\beta \simeq 80^\circ$, Mestel & Moss (1981) considered that this may be caused by dissipative processes causing β to approach these values. A magnetic star that is dynamically oblate around its magnetic axis, being different from the axis of rotation, will steadily decrease β to approach the asymptotic value of $\beta = 0$. Likewise, a star that is dynamically prolate about its magnetic axis will steadily increase β to approach 90° through processes such as turbulent viscosity and radiative loss. Mestel & Moss calculated the time scale for these loss processes to be effective, to be comparable to the stellar nuclear lifetime, providing only weak corroborative evidence for their theory.

By statistically investigating the validity of a random distribution of β -values, the above proposal may be examined.

III.3.2 Statistical tests

To investigate the distribution of magnetic to rotational axes statistically, two statistical tests, The Kolmogorov-Smirnov test and von Mises ω^2 test were employed.

III.3.2.1 The Kolmogorov-Smirnov test.

The Kolmogorov-Smirnov distribution-free statistic D_n^α , which gives the probability α that the empirical distribution function will have a departure D_n from the distribution function $P(r)$, may be used to decide whether the data sample may be considered as a random sample from a parent population. The parent population may be defined in terms of some hypothesis as to the frequency distribution of i, β . D_n is then defined as,

$$D_n = \sup|P(r) - S_n(r)| \quad (3.95)$$

being the largest departure from $P(r)$ from the empirical distribution function $S_n(r)$, hereafter referred to as the e.d.f. The probability of such a departure may then be evaluated with recourse to the probability tables for the Kolmogorov-Smirnov two-tailed test.

III.3.2.2 The von Mises ω^2 test.

The von Mises ω^2 criterion is given by (von Mises 1964),

$$\omega_n^2 = n^2 \int_{-\infty}^{\infty} \lambda(x) [1 - F(x)] dx \quad (3.97)$$

where $\lambda(x)$ is the weight function and, if constant, the normalization to unity of the expectation value $E[\omega_n^2]$ requires that,

$$\lambda^{-1} = n \int_{-\infty}^{\infty} F(x) [1 - F(x)] dx \quad (3.97)$$

Let x_1, x_2, \dots, x_n be the ordered sequence of x values, the e.d.f, such that,

$$S_n(x) = \begin{cases} 0 & x < x_1 \\ \frac{\nu}{n} & x_\nu \leq x < x_{\nu+1} \\ 1 & x \geq x_n \end{cases} \quad (3.98)$$

then

$$\frac{\omega_n^2}{\lambda n^2} = \int_{-\infty}^{\infty} [S_n(x) - F(x)]^2 dx \quad (3.99)$$

and, on expansion

$$\begin{aligned} \frac{\omega_n^2}{\lambda n^2} &= \int_{-\infty}^{x_1} F^2(x) dx + \sum_{\nu=1}^{n-1} \int_{x_\nu}^{x_{\nu+1}} \left[\frac{\nu}{n} - F(x) \right]^2 dx \\ &+ \int_{x_n}^{\infty} [1 - F(x)]^2 dx \end{aligned} \quad (3.100)$$

The summation term may further be broken down into,

$$\begin{aligned} \sum_{\nu=1}^{n-1} \int_{x_\nu}^{x_{\nu+1}} \left[\frac{\nu}{n} - F(x) \right]^2 dx &= \sum_{\nu=1}^{n-1} \left\{ \left(\frac{\nu}{n} \right)^2 (x_{\nu+1} - x_\nu) - 2 \frac{\nu}{n} \int_{x_\nu}^{x_{\nu+1}} F(x) dx \right. \\ &\left. + \int_{x_\nu}^{x_{\nu+1}} F^2(x) dx \right\} \end{aligned}$$

Evaluating all terms in Eq. (3.100), using

$$G(x) = \int_0^x F(x)dx \quad (3.101)$$

results in

$$\begin{aligned} \omega_n^2 = & \lambda n^2 \int_{-\infty}^0 F^2(x)d(x) + \lambda n^2 \int_0^{\infty} [1 - F(x)]^2 dx \\ & - \lambda \sum_{\nu+1}^{\infty} (2\nu - 1)x_{\nu} + 2\lambda n \sum_{\nu=1}^n \int_0^{x_{\nu}} F(x_{\nu})dx \end{aligned} \quad (3.102)$$

Letting

$$F(x) = \begin{cases} 0 & x < 0 \\ \frac{x}{c} & 0 \leq x < c \\ 1 & x \geq c \end{cases}$$

then

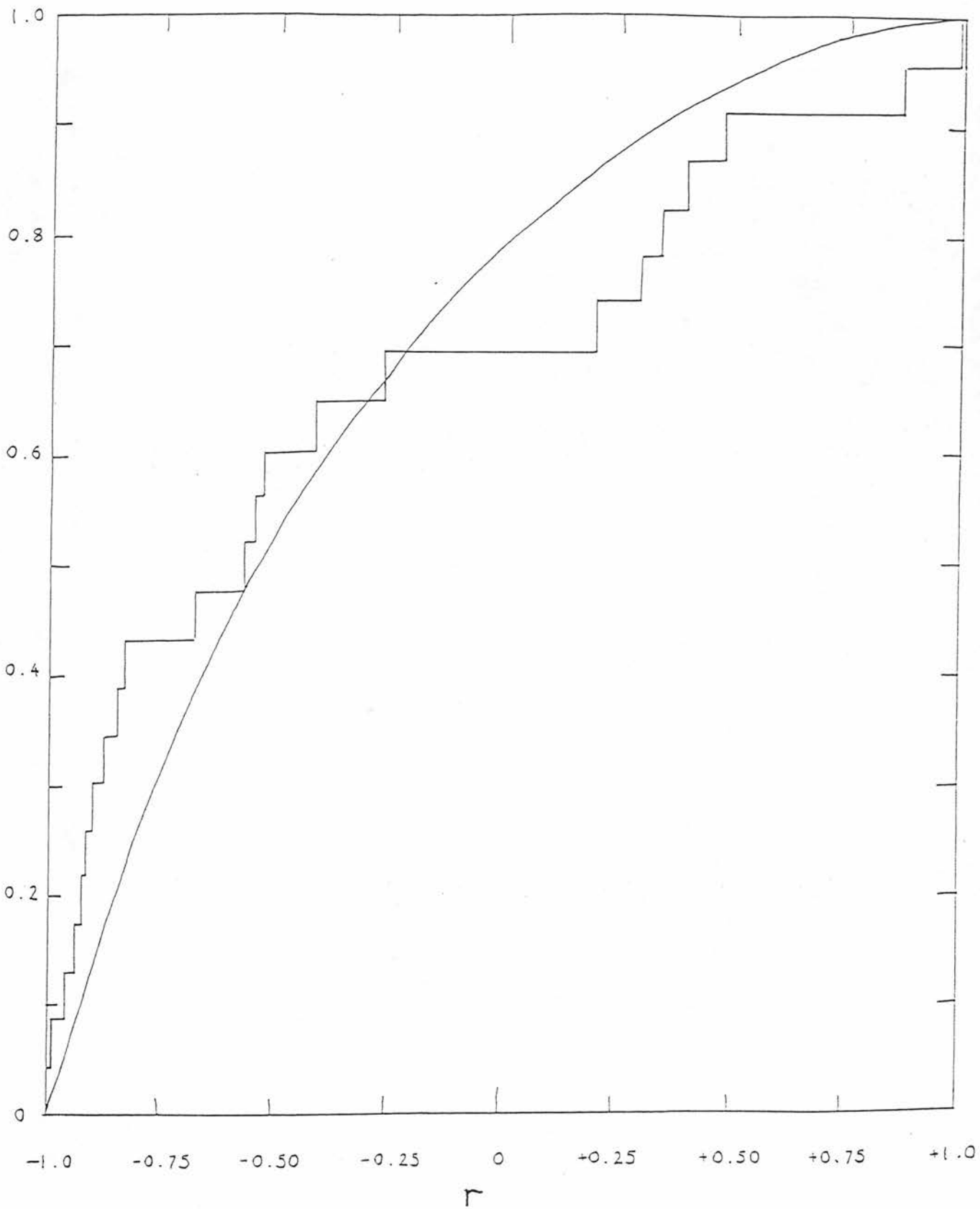
$$\omega_n^2 = \frac{1}{2n} + 6 \sum_{\nu=1}^n \left[F(x_{\nu}) - \frac{2\nu - 1}{2n} \right]^2 \quad (3.103)$$

Using Eq. (3.107) and the tabulated values of ω_n^2 in the probability table (Table (VII)), it is possible to define a confidence band within which the observed data are seen to be compatible with the theoretical distribution.

Table VII

p	$\alpha = (1 - p)$	ω_{∞}^2	p	$\alpha = (1 - p)$	ω_{∞}^2
0.10	0.90	0.276	0.70	0.30	1.104
0.20	0.80	0.372	0.80	0.20	1.446
0.30	0.70	0.475	0.90	0.10	2.082
0.40	0.60	0.582	0.95	0.05	2.766

Stibbs' comparison of theoretical & observed r-values



0.50	0.50	0.715	0.99	0.01	4.458
0.60	0.40	0.882	0.999	0.001	7.008

III.3.3.1 Hypothesis Testing

Preston's original sample of magnetic star r -values (Figure XLIV) has already been analyzed by Stibbs (1974) who strongly advocated the use of distribution-free tests for goodness of fit. Application of the von Mises ω_n^2 test and the K-S test revealed that there was no strong evidence for the grouping suggested by Preston. The K-S two tailed test, using the largest departure in figure XLIV at $r = -0.75$, $D_n = 0.162$, revealed that this departure occurs with probability greater than 20%. Likewise, the von Mises ω_n^2 test revealed that $\omega_n^2 = 1.025$ occurs with probability of 34%. Thus, the null hypothesis that the distribution of magnetic axes is random may be readily accepted.

Recent work has since enlarged the sample of 23 stars considered in this early analysis, and a further analysis may be conducted on 36 accurate variations including HD49976.

The stars considered in this analysis and their respective r -values are shown in table (VIII).

—Table (VIII)—

Name	Alternative	r -value	Reference
BD+33 953	HD32633	-0.32 (-0.61)	B/L
θ Aur	HD40312	-0.67 ✓	B/L
53 Cam	HD65339	-0.78 (-0.67)	B/L
α^2 CVn	HD112413	-0.74 (-0.80) ✓	B/L
78 Vir	HD118022	+0.15 (+0.29)	B/L

CS vir	HD125248	-0.89 (-0.82)	B/L
HR 5597	HD133029	+0.71	B/L
β CrB	HD137909	-0.66 (-0.70) ✓	B/L
52 Her	HD152107	+0.67 (+0.65)	B/L
γ Equ	HD201601	+1.00	B/L
BD+54 2846	HD215441	+0.54	B/L
γ Ari S	HD11503	-0.46	B/L
α Psc A	HD12447	-0.84	B/L
56 Ari	HD19832	-0.90	B/L
CU vir	HD124224	-0.54 ✓	B/L
ω Her	HD148112	+0.35	B/L
ϕ Dra	HD170000	-0.35	B/L
HR 7870	HD196178	+0.47	B/L
ν For	HD12767	-0.82	B/L
r^9 Eri		+0.04	B/L
	HD126515	-1.00	L/M/T & M
	HD107830	-0.25	P
	HD32633	-0.50 ^{M^o}	T,P
	HD153882	-0.48	T,P
73 Dra	HD196502	-0.83	T,Pa
	HD71866	-0.92	T/P
	HD8441	-0.53 ✓	T
21 Per		-0.94	P
	HD98088	-0.83	P
	HD187474	-0.95	P
	HD188041	+0.27	P
17 Com	HD108486	-0.25	P/S/W

κ Cnc	HD108651	-1.00	P/S/W
	HD37776	-0.86	T/L
	HD49976	-0.98	*

Multiple r -values are given where measurements are available for the photoelectric, and photographic measurement systems. References are:

B/L :	Borra & Landstreet (1980)
T:	Trasco (1972)
P/S/W:	Preston, Stephien & Wolff (1969)
Pa:	Preston (1967)
T/L:	Thompson & Landstreet (1985)
P:	Preston (1967).

The 36 stars used in this analysis given in table (VIII) are shown in e.d.f format in Figure (XLV). Also depicted is the hypothetical distribution for a random orientation of magnetic to rotational axes.

Application of the K-S two tailed test to the data reveals the greatest departure to occur at $r = -0.82$, and applying $D_n = 0.12$, it is seen that for a sample size of $n = 36$, $\alpha > 0.2$. Thus, at the 80% level, there is no evidence to suggest that the observed data are incompatible with the hypothesis of random orientation of magnetic to rotational axes. Likewise, application of the von Mises ω_n^2 test gives $\omega_n^2 = 0.557$, which according to table (VII) and, applying the asymptotic probability for $n = \infty$, reveals that $\alpha = 0.62$. This is absolutely consistent with the hypothesis of random orientation of magnetic to rotational axes, and strongly reinforces the earlier conclusion of Stibbs.

It is concluded that for all the data available at the present time, there is no statistical evidence to suggest that there is a preferential angle or group of angles of the magnetic to rotational axes in magnetic variable stars and, con-

Comparison for expanded sample size = 36 stars

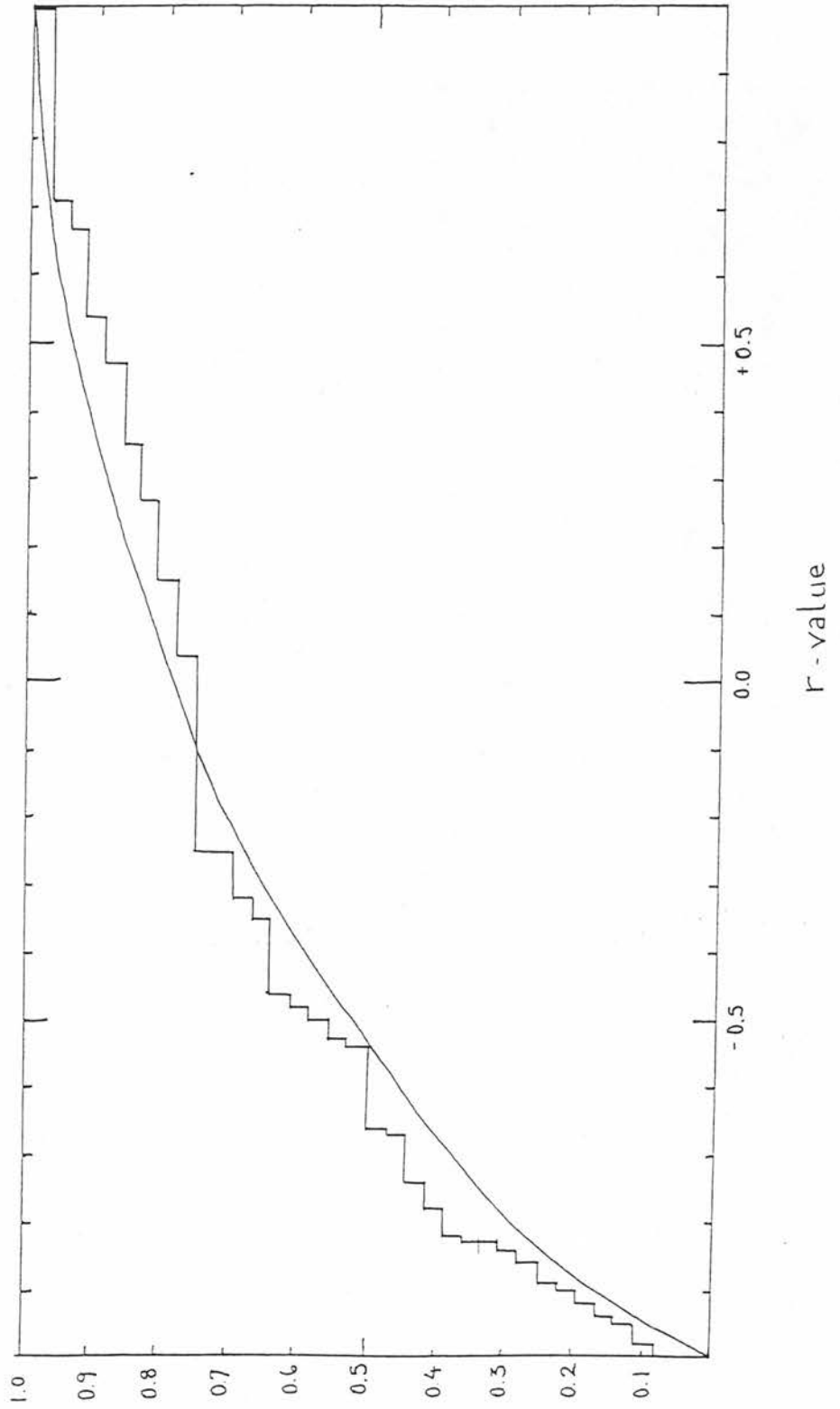
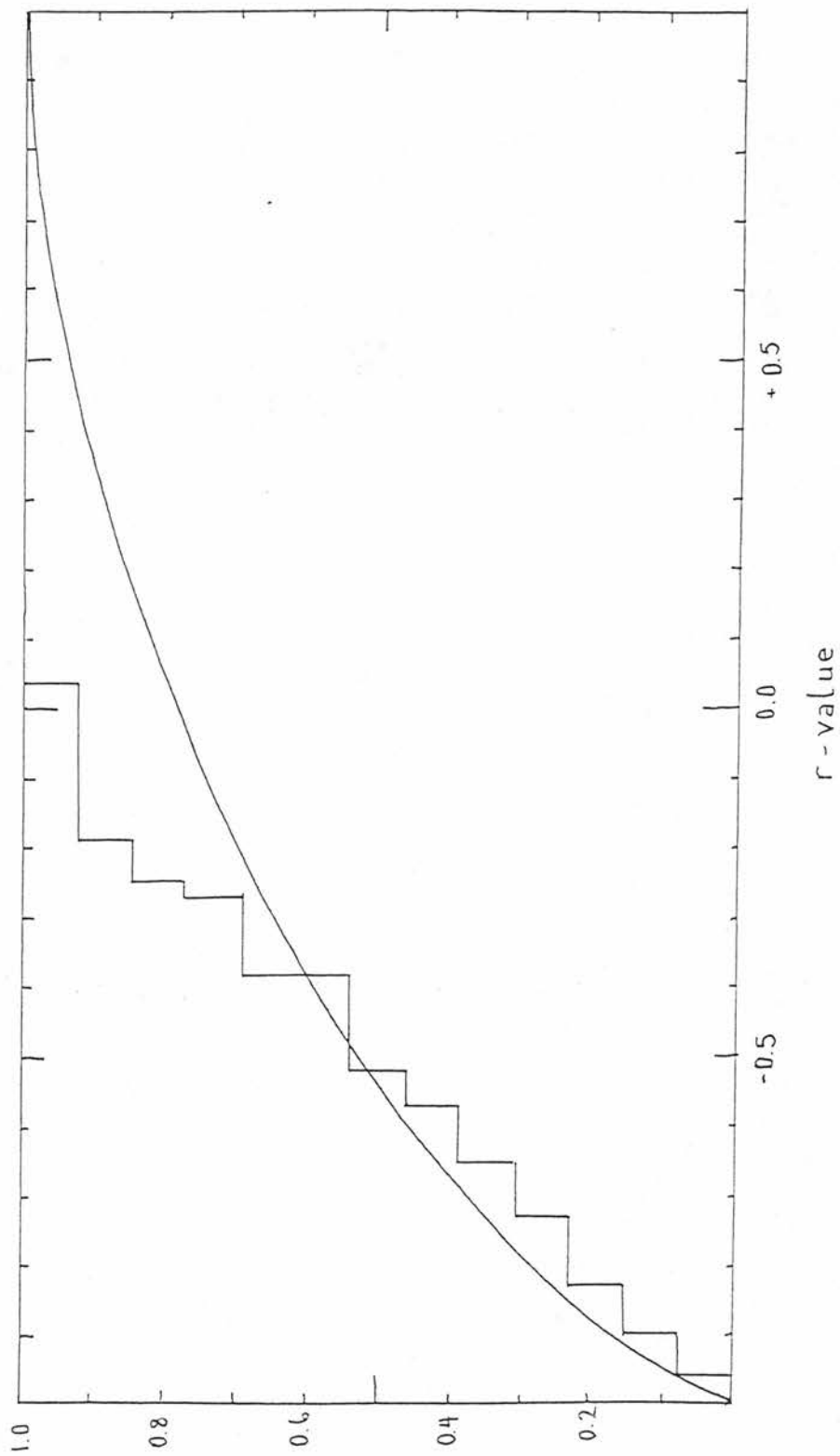


Table IX

Star (HD) Spectral Type	n σ (gauss)	Extrema (gauss)	$\langle B_e \rangle = \sigma$ (gauss)	Possible Periods (days)
35298	5	+2920	2230 = 200	1.9
B3 HeW	450	-2810		
35456	6	+1080	615 = 120	1.7; 2.5; 3.3; 8.2
B6 Ap	300	-300		
35502	6	-95	1490 = 140	1.7
B5 HeW	340	-2250		
36313	6	+1110	915 = 180	3.5; 6.2
B9 Ap	440	-1520		
36429	5	+160	425 = 170	...
B4 HeW	380	-840		
36540	4	+1030	470 = 220	...
B7 HeW	440	-400		
36526	6	+3480	2130 = 200	1.6
B9 HeW	490	-980		
36668	6	+1320	900 = 180	2.1; 2.7; 3.0
B6 Ap	440	-1590		
37140	6	+400	450 = 210	...
B7 HeW	510	-1050		
37151	4	+345	190 = 190	...
B8 Ap	380	-530		
37210	4	+400	280 = 250	...
B9 Ap	500	-760		
37470	4	+150	0.0 = 230	...
B8 Ap	450	-260		
37642	6	+2700	2110 = 180	0.8
B9 Ap	440	-2980		
Orion Nebula Cluster				
36981	1	+450	450 = 440	...
B4 V	440	...		
37062	1	+760	760 = 690	...
B5 V	690	...		
37150	1	...	489 = 260	...
B2.5 V	260	-489		

Comparison for OB1 association r -values



sequently, the data may be taken to be entirely consistent with the hypothesis of a random distribution.

III.3.3.2 Observations on young stars

Despite the lack of evidence to support Preston's proposal of two groups, the suggestion that the orientation distribution of magnetic to rotational axes may be time dependent, proposed by Mestel & Moss, may still occur. To this end, an investigation of the r -values of young stars may be conducted. Borra (1981) conducted an investigation into such a group, the Orion OB1 association. Borra states that these young stars, $\simeq 5 \times 10^6$ years old have magnetic fields in excess of older stars and have higher rotational velocities. He concludes that these findings provide supporting evidence for the fossil theory of magnetic field production. Borra also states that his sample of magnetic observations is too small to apply statistical tests on r -values. It is suggested that the von Mises ω_n^2 test could produce meaningful results on a sample of 13 stars, as it is a powerful distribution-free non-parametric hypothesis testing procedure for global goodness of fit.

Borra applied the technique of H_α polarimetry with a $4A^0$ filter, instead of H_β polarimetry, to obtain measurements of the magnetic field strength for an unbiased sample of 13 stars within the Orion OB1 association. The data are reproduced in table (IX) along with the magnetic field extrema.

Figure (XLVI) illustrates the data in e.d.f format for application to the aforementioned statistical tests. The K-S statistic D_n is found to be $D_n=0.21$ at $r = -0.19$, and this shows that for $n = 15$, $\alpha > 0.20$, and there is therefore no evidence to suggest that the sample shows a preferential inclination between magnetic and rotational axes. The von Mises ω_n^2 statistic is evaluated as $\omega_n^2 = 1.390$ corresponding to $\alpha = 0.21$. Again there is no strong evidence for the alternative hypothesis of preferential axes of inclination.

If the angle of inclination between magnetic and rotational axes is time dependent then a difference between the distribution of young and old stars should be visible. However, both data sets are consistent with the hypothesis of a random distribution, and this requires that if any migration of the magnetic pole does occur, it must be very small. Since the OB1 stars are so young, this eliminates such large migration as Mestel & Moss sought to obtain.

III.3.3.3 Discussion

Though the statistical tests performed indicate that the data is consistent with the hypothesis of a random distribution of magnetic to rotational axes inclination, it is important to consider to what extent those firm conclusions would be perturbed by departures from the adopted model.

The theoretical relation between the r -values and the angles i, β was derived on the basis of a central dipolar oblique rotator model. If this is not the case, and a quadrupole or offset dipole is necessary, as indicated by many authors, then an interpretation based upon this analysis would be subject to some uncertainty, particularly if the null hypothesis were not so readily accepted.

Considering the strongly harmonic variations observed in H_β polarimetry studies, it is felt that the effect of any quadrupole component would be necessarily small and would produce only small perturbations to the oblique rotator model. In any case, the high probability with which the data are consistent with the hypothesis of random β on the central dipole model, mitigates against the possibility that another model would reject the null hypothesis. It is thus concluded that there is no evidence to support Preston's proposal under this analysis, and that minor changes in the oblique rotator model are unlikely to invalidate this result.

APPENDIX-A: Absorption line-list

FE-I

Position (A°)	Z-value	Window width (A°)
3852.574	1.500	1.20
3859.913	1.500	1.60
3863.745	1.300	1.60
3872.504	1.500	1.40
3902.948	1.210	1.10
3903.902	0.990	1.20
3922.914	1.500	1.20
3930.299	1.500	1.20
3948.779	0.960	1.20
3951.154	1.250	1.40
3956.681	1.210	1.80
3986.175	0.800	1.60
3995.996	0.610	1.20
4005.246	1.500	1.60
4030.499	0.800	2.00
4045.815	1.250	1.60
4063.597	1.080	1.60
4067.984	1.540	1.20
4071.740	0.680	1.00
4073.760	1.500	1.20
4112.972	1.360	1.80
4118.549	1.040	1.20
4134.681	1.190	1.40
4143.871	1.500	1.80
4147.673	2.000	1.50
4149.372	1.420	1.20
4156.803	1.380	1.80
4157.788	1.500	1.10

4170.906	1.500	1.40
4173.450	1.490	1.40
4177.700	1.710	1.20
4181.758	1.500	2.00
4187.802	1.470	1.10
4191.438	1.500	2.00
4198.310	1.500	1.40
4202.031	1.180	1.20
4203.987	1.420	1.40
4217.551	1.440	1.80
4219.364	1.070	1.40
4222.219	1.750	1.80
4227.434	1.230	1.50
4233.167	1.210	2.00
4238.816	1.000	1.40
4247.432	1.100	1.10
4250.790	0.940	2.20
4260.479	1.600	1.60
4267.830	1.550	2.00
4282.406	1.330	1.80
4325.765	0.833	2.00
4404.752	1.130	1.60
4415.125	1.100	1.60
4430.618	2.500	2.00
4447.722	2.000	1.40
4466.554	1.170	1.30
4476.021	1.000	1.40
4494.568	1.190	1.20
4525.142	1.330	1.60

FE-II

3935.942	1.060	1.40
4002.549	1.070	1.20
4032.946	0.890	1.80
4122.638	1.490	1.40
4258.155	1.070	1.60
4273.317	2.170	1.80
4278.128	0.210	1.80
4296.567	0.500	1.40
4351.764	1.100	1.20
4369.610	1.500	1.60
4385.381	1.330	1.40
4416.817	0.840	1.50
4472.957	1.500	1.80
4489.185	1.500	1.60
4508.283	0.500	1.30
4515.337	1.030	2.00
4520.225	1.500	1.60

CR-I

3857.631	2.000	1.40
3983.907	0.875	1.80
3992.845	1.670	1.40
4039.100	1.140	1.20
4129.210	1.300	1.00
4174.795	1.250	1.10
4190.160	2.500	1.40
4254.346	1.380	1.60
4274.803	1.960	1.20
4371.279	1.380	1.60
4391.753	2.000	1.30
4496.862	1.330	1.60
4514.373	1.080	1.30

4526.466	1.330	1.40
----------	-------	------

CR-II

3865.590	1.070	1.40
3945.110	0.000	1.60
3979.520	1.070	1.30
4012.500	0.600	1.60
4017.960	1.800	1.20
4022.360	1.030	1.90
4038.030	1.050	1.40
4049.140	0.970	1.70
4051.970	1.160	1.70
4054.110	1.510	1.80
4056.070	0.400	1.50
4070.900	1.060	1.20
4072.560	0.840	1.20
4082.300	1.110	1.70
4086.140	1.350	1.30
4087.630	1.670	1.70
4111.010	1.100	1.70
4151.000	0.920	1.40
4179.430	1.210	1.90
4195.410	1.400	1.80
4207.350	1.480	1.50
4229.810	1.900	1.60
4242.380	1.170	1.70
4246.410	2.100	1.40
4252.620	1.230	1.90
4261.920	1.000	1.80
4269.280	0.800	2.10
4275.570	0.770	1.10
4284.210	0.530	1.60
4511.820	0.940	2.00

Null line

TI-II

3900.546	1.110	1.30
3913.463	0.890	1.30
4028.332	1.060	1.70
4163.644	1.070	1.70
4290.222	1.100	2.10
4294.101	1.200	1.60
4300.052	1.220	2.40
4307.900	1.470	1.40
4312.861	1.490	1.70
4316.807	0.670	1.70
4394.057	1.340	1.10
2211.936	1.330	1.20
4450.487	1.030	1.50
4468.493	1.060	1.30
4501.270	0.930	1.60

SR-II

4077.714	1.170	1.80
4161.796	1.330	2.00
4215.524	1.330	2.30

CA-II

4318.652	1.500	1.00
4425.441	0.500	1.60

REFERENCES

- Adam, M.G., (1965) *The Observatory* (vol. 85), 948, p.204
- Angel, & Landstreet, J.D., (1970) *Ap J. lett.* 160, L147
- Babcock, H.W., (1947) *Ap J.* 105, 105
- Babcock, H.W., (1958) *Ap J. suppl.*, 3, 141
- Bergland (1969) *I.E.E.E. computing* 21, 366
- Böhm-Vitense, E., (1965) *Magnetism & the cosmos* Ed. W.R.
—Hindmarsh New York: American Elsevier pub. co. Inc. p.179
- Böhm-Vitense (1966) *Zs.f. Ap.* 64, 326
- Böhm-Vitense (1967) *Zs.f. Ap.* 67, 1
- Bonsack W.K., (1987) *Private communication*
- Borra, E.F., (1974) *Ap J.* 188, 287
- Borra, E.F., (1981) *Ap J. lett.* 249, L39
- Borra, E.F., & Landstreet, J.D., (1977) *Ap J.* 228, 809
- Borra, E.F., & Landstreet, J.D., (1980) *Ap J. suppl.*, 42, 421
- Borra, E.F., & Vaughan, A.H., (1976) *Ap J.* 210, L145
- Brault, J.W., & Piersol, A.G., (1971) *I.E.E.E. info. T.* 7, 7
- Brault, J.W., & White (1971) *Astron. & Astrophys.* 13, 71
- Brenner, N.M., (1970) "FOURT; available COSMIC/SHARE, univ. Georgia
- Chandrasekhar, S., (1950) *Radiative transfer*, Oxford:
—Clarendon press p.306
- Chandrasekhar, S., & Munch, G., (1946) *Ap J.* 104, 446
- Cooley & Tukey (1965) *Math. computing* 19, 297
- Cowling, T.G., (1952) *M.N.R.A.S* 112, 527
- Deutsch, A.J., (1970) *Ap J.*, 159, 985
- Deutsch, A.J., (1958) *I.A.U. symp. ed. B. Lenhert* 6, 209
- Fisher (1983) *Publ. of the Dominion obsv.*

- Hale, G.E., (1913) Ap J., 38, 57
- Havnes, O., & Conti, P.S., (1971) Astron. & Astrophys. 14, 1
- Hensberge, H., van Rensbergen, W., Gossens, M., Deridder, G., (1977)
—Astron. & Astrophys. 61, 235
- Hill G.W., (1982) Publ. of the Dominion obsv. 16, 11
- Hill, G.W., (1982) Publ. of the Dominion obsv. 16, 27
- Hill G.W., (1986) Publ. of the Dominion obsv. 16, 5
- Hockey, M.S., (1969) M.N.R.A.S. 142,543
- Hubbard, E.N., & Dearborn, D.S.P., (1982) Ap J. 254, 196
- Kemp, J.C., & Wolstencroft (1974) M.N.R.A.S 166, 1
- Krause & Oetken, L., (1976) *Equatorially symmetric models for
—magnetic stars as suggested by Dynamo theory*, p.29
- Leahy, D.A., & Vilenkin, A., (1981) Ap J. 248, 13
- Ledoux, P., & Renson, P., (1966) Ann. rev. astron. & Astrophys.
—3, 293
- Maitzen & Albrecht (1975) Astron. & Astrophys. 44, 405
- Mestel, L., & Moss, D., (1981) M.N.R.A.S 195, 979
- Mestel, L., Nittman, J., Wood, W.P., Wright, G.A.E.,
—(1981) M.N.R.A.S 195, 979 Michaud, G., (1970) Ap J.,
—160, 641
- Mihalas, D., (1973) Ap J. 184, 851
- Morton, D.C., & Adams T.F., (1968) Ap J. 151, 611
- Olson, E.C., (1974) P.A.S.P. 86, 80
- Pilachowski, C.A., Bonsack, W.K., & Wolff S.C., (1976) Astron. &
—Astrophys. 37, 275
- Preston, G.W., (1967) Ap J. 150, 547
- Preston, G.W., (1970) *Stellar rotation*, Ed. Slettebak, A., Reidel

- publ. co. p.254
- Preston, G.W., (1970) Ap J. **160**, 1059
- Preston, G.W., (1972) Ap J. **175**, 465
- Preston, G.W., (1967) Ap J. **150**, 871
- Preston, G.W., & Pyper, D.M., (1965) Ap J. **142**, 983
- Preston, G.W., Stepien, K., & Wolff, S.C., (1969) Ap J. **156**,653
- Pyper, D.M., (1969) Ap J. suppl. **18**, 347
- Robinson, R.D., (1980) Ap J. **239**, 961
- Sâto, Y., (1950) Bull. Earthquake research Inst. (tokyo),
—**28**,175
- Schmidt, A., (1899) Zs. math. phys., **44**, 327
- Seares, H., (1913) Ap J. **38**, 99
- Shallis, M.J., & Blackwell, D.E., (1979) Astron. & Astrophys.
—**79**, 48
- Simkin, R.D., (1974) Astron. & Astrophys. **31**, 129
- Stibbs, D.W.N., (1950) M.N.R.A.S **110**, 395
- Stibbs, D.W.N., (1974) I.A.U. coll. **32**, p.446
- Stibbs, D.W.N., & Carson, T.R., (1987) *Private communicate*
- Stift, M.J., (1974) Astron. & Astrophys. **34**, 153
- Thomas & Athay (1961) *Physics of the solar chromosphere*
—New York:Interscience publ. p.71
- Thompson, I.B., & Landstreet, J.D., (1984) Ap J. **289**, L9
- Trasco, J.D., (1970), Ap J. **171**, 569
- Unno, W., (1956) Astro. soc. of Japan **8**, 109
- von Mises, R., (1964) *Mathematical theory of probability and statistics*
—(*Edited and complemented by H. Geiringer*) Academic press p.471-490
- van de Heuvel, E.P.J., (1971) Astron. & Astrophys. **11**, 461

- Weiss, W.W., Jenkner, H., Wood, H.J., (1978) *Astron. & Astrophys.*
—**63**,247
- Wells, D.C., Greisen, E.W., & Harten, R.H., (1981) *Astron. & Astrophys*
—suppl. **44**, 363
- Winzner, J.E. (1974) *Ph.D thesis*, Univ. of Toronto
- Wolff, S.C., & Bonsack, W.K., (1972) *Ap J.* **176**, 425
- Woltjer, W., (1969) Private communication to Angel & Landstreet
- Woolley, R.d.v.R., Epps, E.A., Penston, M.J., & Poccock, S.B., (1970)
—*Catalogue of stars within 25pc of the sun* Royal obsv.
—annals **5** R.G.O
- Wrubel, M., (1949) *Ap J.*, **109**, 66
- Wrubel, M., (1950) *Ap J.*, **111**, 157
- Zeeman, (1913) *Researches in magneto-optics*, London:MacMillan
—& co., p.150